Universität Potsdam
Institut für Erd- und Umweltwissenschaften

Flow and Reactive Transport Modeling at the Stream-Groundwater Interface: Effects of Hydrological Conditions and Streambed Morphology

Kumulative Dissertation

zur Erlangung des Doktorgrades der Ingenieurwissenschaften (Dr.-Ing.)
in der Wissenschaftsdisziplin Geowissenschaften – Hydrogeologie

eingereicht an der
Mathematisch-Naturwissenschaftlichen Fakultät
der Universität Potsdam

von
Dipl.-Ing. Geowiss. Nico Trauth

Gutachter:

1. Prof. Dr. Sascha E. Oswald
2. PD Dr. Jan H. Fleckenstein
3. Prof. Dr. Reinhard Hinkelmann

Tag der mündlichen Prüfung: 09. Oktober 2015

Published online at the
Institutional Repository of the University of Potsdam:
URN urn:nbn:de:kobv:517-opus4- 82748
http://nbn-resolving.de/urn:nbn:de:kobv:517-opus4- 82748

This dissertation was carried out at the Department of Hydrogeology at the Helmholtz Centre for Environmental Research – UFZ, Leipzig, Germany.
It was funded by a grant of the Ministry of Science, Research, and Arts of Baden-Württemberg (AZ Zu 33-721.3-2, Water and Earth System Science (WESS) Competence Centre) and the Helmholtz Centre for Environmental Research – UFZ, Leipzig, Germany.

Selbstständigkeitserklärung

Hiermit erkläre ich, Nico Trauth, die vorliegende Dissertation selbstständig und ohne unzulässige fremde Hilfe angefertigt zu haben. Ich habe keine anderen als die angeführten Quellen und Hilfsmittel benutzt und sämtliche Textstellen, die wörtlich oder sinngemäß aus fremden Arbeiten entnommen wurden als solche kenntlich gemacht.
Die Arbeit wurde in gleicher oder ähnlicher Form bisher nicht an einer Universität eingereicht.

Leipzig, den

The sciences, each straining in its own direction, have hitherto harmed us little;
but some day the piecing together of dissociated knowledge will open up such terrifying vistas of reality, and of our frightful position therein,
that we shall either go mad from the revelation or flee from the deadly light into the peace and safety of a new dark age.

– H.P. Lovecraft

Abstract

Stream water and groundwater are important fresh water resources but their water quality is deteriorated by harmful solutes introduced by human activities. The interface between stream water and the subsurface water is an important zone for retention, transformation and attenuation of these solutes. Streambed structures enhance these processes by increased water and solute exchange across this interface, denoted as hyporheic exchange.

This thesis investigates the influence of hydrological and morphological factors on hyporheic water and solute exchange as well as redox-reactions in fluvial streambed structures on the intermediate scale (10–30 m). For this purpose, a three-dimensional numerical modeling approach for coupling stream water flow with porous media flow is used. Multiple steady state stream water flow scenarios over different generic pool-riffle morphologies and a natural in-stream gravel bar are simulated by a computational fluid dynamics code that provides the hydraulic head distribution at the streambed. These heads are subsequently used as the top boundary condition of a reactive transport groundwater model of the subsurface beneath the streambed. Ambient groundwater that naturally interacts with the stream water is considered in scenarios of different magnitudes of downwelling stream water (losing case) and upwelling groundwater (gaining case). Also, the neutral case, where stream stage and groundwater levels are balanced is considered. Transport of oxygen, nitrate and dissolved organic carbon and their reaction by aerobic respiration and denitrification are modeled.

The results show that stream stage and discharge primarily induce hyporheic exchange flux and solute transport with implications for specific residence times and reactions at both the fully and partially submerged structures. Gaining and losing conditions significantly diminish the extent of the hyporheic zone, the water exchange flux, and shorten residence times for both the fully and partially submerged structures. With increasing magnitude of gaining or losing conditions, these metrics exponentially decrease.

Stream water solutes are transported mainly advectively into the hyporheic zone and hence their influx corresponds directly to the infiltrating water flux. Aerobic respiration takes place in the shallow streambed sediments, coinciding to large parts with the extent of the hyporheic exchange flow. Denitrification occurs mainly as a “reactive fringe” surrounding the aerobic zone, where oxygen concentration is low and still a sufficient amount of stream water carbon source is available. The solute consumption rates and the efficiency of the aerobic and anaerobic reactions depend primarily on the available reactive areas and the residence times, which are both controlled by the interplay between hydraulic head distribution at the streambed and the gradients between stream stage and ambient groundwater. Highest solute consumption rates can be expected under neutral conditions, where highest solute flux, longest residence times and largest extent of the hyporheic exchange occur. The results of this thesis show that streambed structures on the intermediate scale have a significant potential to contribute to a net solute turnover that can support a healthy status of the aquatic ecosystem.

Kurzfassung

Fluss- und Grundwasser sind wichtige Süßwasserressourcen, deren Qualität durch anthropogene Einträge schädlicher Stoffe vermindert wird. Im Grenzbereich zwischen Fluss- und Grundwasser können diese Stoffe zurückgehalten, umgewandelt oder abgebaut werden. Flussbettstrukturen erhöhen den sogenannten hyporheischen Austausch von Wasser und Stoffflüssen, wodurch diese Prozesse gefördert werden.

In dieser Arbeit wird der Einfluss von hydrologischen und morphologischen Faktoren auf Wasser- und Stoffflüsse sowie Redox-Reaktionen in Flussbettstrukturen der mittleren Skala (10–30 m) untersucht. Hierfür wird ein dreidimensionales numerisches Modell-Konzept verwendet, welches die Flussströmung und die Strömung im darunter liegenden porösen Medium koppelt. Mit einer Computational Fluid Dynamics Software wird die stationäre Flussströmung über generische Pool-Riffle Strukturen sowie über eine natürliche Flussinsel für verschiedene Abflüsse simuliert. Die berechneten Drücke am Flussbett werden als Randbedingungen erster Ordnung an ein reaktives Grundwasser- und Stofftransportmodell übertragen. An der unteren bzw. seitlichen Randbedingung werden zusätzliche Gradienten erzeugt, die die Interaktion zwischen Fluss und regionalem Grundwasser als in– oder exfiltrierende Bedingungen repräsentieren. Sind Flusswasser- und Grundwasserstand ausgeglichen, liegen neutrale Bedingungen vor. Im Grundwassermodell werden der Transport von Sauerstoff, Nitrat und gelöstem organischen Kohlenstoff sowie deren mögliche Reaktion durch aerobe Respiration und Denitrifikation modelliert.

Die Simulationensergebnisse zeigen, dass der hyporheische Austausch durch hydraulische Gradienten am Flussbett verursacht wird. Existiert ein zusätzlicher hydraulischer Gradient zwischen Fluss- und Grundwasser, werden die ausgetauschten Wassermengen sowie die Größe der hyporheischen Zone vermindert, was mit kürzeren Verweilzeiten einhergeht. Dieser Effekt ist unabhängig von der Richtung dieses Gradienten und umso ausgeprägter, je stärker der Gradient zwischen dem Grundwasser und dem Flusswasserstand ist.

Die im Flusswasser gelösten Stoffe werden advektiv in die hyporheische Zone transportiert. Die aerobe Respiration nimmt große Bereiche der flachen hyporheischen Zone ein. Hohe Denitrifikationsraten existieren vor allem in einem “reaktiven Saum”, der den aeroben Bereich umschließt, da hier die Sauerstoffkonzentration niedrig und ausreichend Kohlenstoff verfügbar ist. Die Raten und die Effizienz der aeroben und anaeroben Reaktionen hängen vor allem von dem für die Reaktionen verfügbaren Raum sowie den Verweilzeiten der Stoffe in der hyporheischen Zone ab. Beide Parameter werden von der Wechselwirkung zwischen den hydraulischen Gradienten entlang des Flussbettes und dem Gradienten zwischen Fluss- und Grundwasser kontrolliert. Die höchsten Zehrraten werden unter neutralen Bedingungen erreicht, wenn die Menge der infiltrierenden gelösten Stoffe am höchsten ist, die längsten Verweilzeiten auftreten und die hyporheische Zone die größte Ausbreitung aufweist. Die Ergebnisse dieser Arbeit zeigen, dass die untersuchten Flussbettstrukturen ein bedeutendes Potential für den Umsatz von Wasserinhaltsstoffen haben können, wodurch ein guter Status des aquatischen Ökosystems gefördert wird.

Contents

List of Figures

List of Tables

1 | General Introduction

1.1 Surface Water – Groundwater Interactions

About 30 % of global fresh water is groundwater [Shiklomanov, 1997] and up to 2 billion people on earth receive drinking water from this resource [Sampat and Peterson, 2000]. Also, groundwater is widely used in food production and by industrial processes [Giordano, 2009]. Beside this subsurface water resource, easily accessible surface water bodies like lakes, rivers and streams represent an important water resource for broad usage [Oki and Kanae, 2006], although they only account for a very small portion of global fresh water. Both subsurface and surface water resources are under pressure from alteration, overexploitation, eutrophication and pollution. Occurrence and concentration of critical solutes deteriorate water quality and can harm aquatic ecosystem and restrict water usage. Main inputs of these critical solutes are related to anthropogenic activities introducing fertilizers and contaminants to the environment and consequently to the hydrologic circle [Galloway et al., 2004]. In particular, high emissions of nitrogen-species (e.g. nitrate, ammonia) by intense agriculture, sewage water, industry and burning of fossil fuel favor eutrophication of fresh waters leading to decreased biodiversity, and increased human health risks [Seitzinger et al., 2002; Erisman et al., 2008; Mulholland et al., 2008].
Surface and subsurface water resources are hydraulically connected in most cases representing a single resource [Winter, 1998]. This connection enables an exchange of water and transports solutes in both directions, from surface to subsurface waters and vice versa, leading to an intrusion and a possible mixing of water sources that often differ strongly in solute composition and concentration [Boulton et al., 1998]. In the worst case, surface water groundwater exchange facilitates a contamination of one of the two water sources by the other [e.g. Van der Molen et al., 1998; Lewandowski et al., 2011; Engelhardt et al., 2014]. However, at the interface between surface and subsurface waters critical substances possibly are transformed or degraded by heterotrophic microbial activity that is fueled by the available dissolved oxygen and carbon sources [Brunke and Gonser, 1997]. Hence, these processes improve water quality and thus support a healthy status of the aquatic ecosystem. Additionally, the shallow and oxygen rich zones of the streambeds represent diverse aquatic habitats for various organisms and spawning redds.

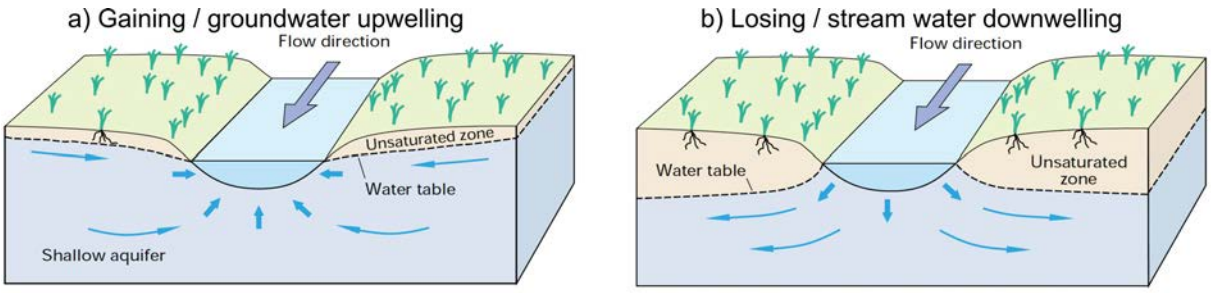

Figure 1.1: Gaining (a) and losing (b) conditions and resulting direction of exchange flow (from Winter [1998]).

The driving forces of the water and solute exchanges across the interface are based on differences between the water level of the surface water and the groundwater evoking hydraulic head gradients. They induce water flows either from the surface water to the groundwater (losing conditions), or a flow from the groundwater to the surface water (gaining conditions) (Figure 1.1). When water levels of surface and groundwater are balanced, hydraulic head gradients are absent and thus water exchange is minimal (neutral conditions).
Additional water and solute exchange is generated by stream water flow over streambed morphologies like meanders, pool-riffles, bars, ripples and obstacles [Packman et al., 2004; Cardenas and Wilson, 2007a,b; Mutz et al., 2007; Boano et al., 2014], which is defined as "hyporheic exchange" and is in the focus of this thesis. It is introduced in the next section.

1.2 Hyporheic Exchange

The Greek term "hyporheic" firstly introduced by Orghidan [1959] means "below" and "flow". Based on this term, the hyporheic zone describes the subsurface water flow below and aside the stream. More precisely, the hyporheic zone is defined as the zone within and beneath the streambed, where stream water infiltrates into the subsurface, flows through the streambed sediments and exfiltrates back to the stream [e.g. Harvey and Bencala, 1993; Winter, 1998; Wondzell and Gooseff, 2013].
Along with the water flux of the hyporheic flow water solutes like ions, nutrients and possible contaminants are transported. In the subsurface, these solutes are potentially exposed to microbial communities that are able to transform and to consume solutes under aerobic and anaerobic conditions. Under aerobic conditions organic carbon is decomposed during respiration of oxygen that represent the primary electron acceptor for aerobic bacteria [Baker et al., 2000]. For conditions where oxygen as electron acceptor is depleted, nitrate is used as the electron acceptor to decompose organic carbon by denitrification, if it is present in relevant quantities [Findlay, 1995; Bencala, 2000; Lowell et al., 2009]. In particular, denitrification is of great importance because it enables a permanent removal of nitrogen from the aquatic system [Harvey and Bencala, 1993; Hill et al., 1998; Zarnetske et al., 2012]. These biogeochemical processes are positively correlated to solute residence time in the hyporheic sediments [Findlay, 1995; Zarnetske et al., 2011a]. Hence, the longer the solutes are in contact with the hyporheic sediment and thus to the microbial communities, the higher the turn-over rates could be, as long as organic carbon is not depleted.
Numerous factors control hyporheic water exchange, solute exchange and reactions. These are distinguishable in physical and biogeochemical factors that are often linked and depend on each other [Boano et al., 2014]. Hyporheic exchange processes are physically controlled by stream stage and discharge at specific stream channel and bed morphologies (Figure 1.2). Since these morphologies exist on various scales, flow path length and residence times range from centimeters to kilometers and from seconds to years, respectively [Stonedahl et al., 2010; Boano et al., 2014; Gomez-Velez and Harvey, 2014]. On the large scale, stream stage differences upstream and downstream of a meander loop create flow through the meander necks [Boano et al., 2006; Cardenas, 2009], also denoted as riparian exchange. On the intermediate scale, partially emerged structures like bars and fluvial islands generate hyporheic zones, where water flow is

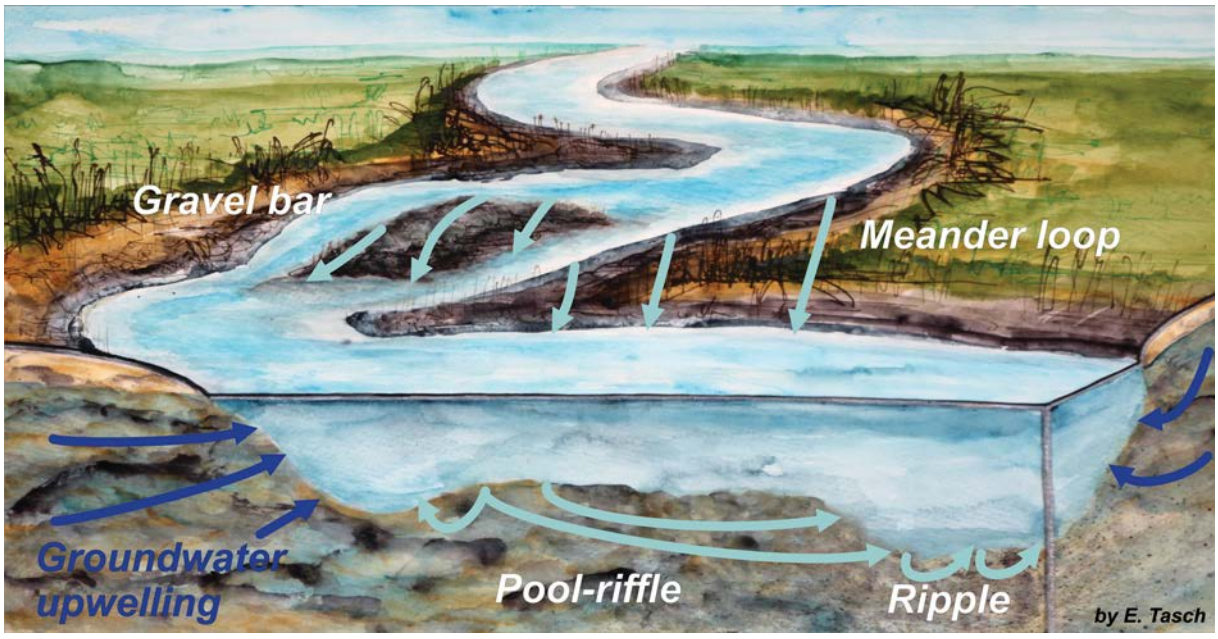

Figure 1.2: Hyporheic exchange flow paths at streambed structures at different scales and groundwater upwelling under gaining conditions.

mainly induced by hydraulic head gradients between river stage differences along these structures [Dent et al., 2007; Cardenas, 2010; Shope et al., 2012]. At submerged structures like pool-riffles sequences, ripples, and obstacles stream flow can generate turbulences, eddies and alternating subcritical and supercritical flow conditions. These flow features locally affect the hydrodynamic component of the flow, denoted as the velocity head [Tonina and Buffington, 2007; Endreny et al., 2011]. According to conservation of energy, the velocity head diminishes the hydrostatic pressure leading to hydraulic head differences at the streambed. In general, high hydraulic heads can be observed at the upstream side and low hydraulic heads at the downstream side of submerged structures. As a result, stream water infiltrates into the sediment at the upstream side of the structure and exfiltrates back into the stream at the downstream side [Thibodeaux and Boyle, 1987; Harvey and Bencala, 1993; Wörman et al., 2002]. This effect is described as "advective pumping" [Elliott and Brooks, 1997a,b; Packman et al., 2000] and has been observed in 2D flume experiments [Elliott and Brooks, 1997a; Packman et al., 2004; Fox et al., 2014] and numerical models [Cardenas and Wilson, 2007a,b]. In addition to these longitudinal flow paths (in stream flow direction), the three-dimensionality of larger streambed structures, like pool-riffles lead to also lateral flow components increasing complexity of hyporheic exchange [Marzadri et al., 2011; Tonina and Buffington, 2011].

Additionally to this driver of hyporheic exchange, the ambient groundwater induces either neutral, losing or gaining conditions that can affect hyporheic exchange processes [Stuart, 1953; Hill et al., 1998; Krause et al., 2013]. Also, sediment properties like grain size distribution, hydraulic conductivity, porosity and heterogeneity directly control hyporheic exchange [Salehin et al., 2004; Fleckenstein et al., 2006] affecting water exchange flux, solute transport, and the residence times in the hyporheic zone.

Biogeochemical factors are represented by presence, activity and growth of microbial communities that directly control reactions in the hyporheic sediments. These factors are also strongly related to physical factors. For example, streambed permeability may be decreased by biofilm growth

that in turn, affects pore water flow field, residence times and solute transport [Arnon et al., 2007].

For more than two decades, researchers have been investigating hyporheic exchange processes [Stanford and Ward, 1988; Brunke and Gonser, 1997] and the interplay of their controlling factors. In numerous field studies sophisticated in-situ field measurements [Kalbus et al., 2006; González-Pinzón et al., 2015] have highlighted that both hydrological and biochemical conditions are key factors that control solute turn-over reactions [Findlay, 1995; Zarnetske et al., 2011b]. Furthermore, flume experiments have been used to systematically investigate the driving forces of hyporheic exchange by manipulating streambed morphology and flume stream discharge [Elliott and Brooks, 1997a; Packman et al., 2004; Mutz et al., 2007; Tonina and Buffington, 2007]. Also, the influence on hyporheic flow by heterogeneous streambed sediments [Salehin et al., 2004] and by ambient groundwater flow [Fox et al., 2014] through small scale bedforms have been investigated. Also, aerobic and anaerobic biogeochemical reactions [O'Connor and Hondzo, 2007; Kessler et al., 2012] are considered in flume experiments and improved the understanding in biogeochemical turn-over processes in hyporheic sediments. However, due to the extensive work that is needed to set up a flume experiment, the number of different realizations is limited. Therefore, to expand the knowledge derived from field and flume studies, numerical models can be used, which are described in more detail in the next section.

1.3 Numerical Modeling of Hyporheic Exchange

The first numerical models of surface and subsurface water interaction were used to study the effect of stream stage, channel curvature, and bars on hyporheic exchange flux and residence times in two dimensions on the reach scale [Harvey and Bencala, 1993; Wondzell and Swanson, 1996; Wroblicky et al., 1998]. Increasing computational power has enabled the running of models of higher morphological detail and in three dimensions [e.g. Kasahara and Wondzell, 2003; Storey et al., 2003]. Finally, the advection-dispersion equation was included to simulate heat and solute transport, which enables a detailed insight into temperature and solute distribution as well as mixing of solutes in the subsurface [e.g. Lautz and Siegel, 2006; Wondzell et al., 2009; Munz et al., 2011; Shope et al., 2012]. In the studies referred to above, numerical modeling is conducted in close conjunction with field measurements. Despite their regional application, these studies provide a detailed understanding of hyporheic exchange flow and transport processes far beyond their field site. However, numerical models can be also used in an explorative manner where the modeling domain does not represent a unique site but a representative type of naturally occurring morphological structure. With these explorative modeling approaches the sensitivity of factors controlling hyporheic exchange processes can be systematically evaluated and their effects on solute distribution and reactive hot spots in the hyporheic zone can be delineated.

Surface water flow over streambed morphologies can be accurately represented using Computational Fluid Dynamics (CFD), solving the full Navier-Stokes-Equations [Endreny et al., 2011; Janssen et al., 2012]. For simulating flow in the subsurface the CFD simulations need to be coupled to a flow model for the porous sediment. A common coupling strategy is one-way sequential coupling, where the simulated pressure distribution at the streambed is used as the top boundary condition of the subsurface model. Such an approach has previously been used

by Cardenas and Wilson [2007a], Cardenas and Wilson [2007b], Jin et al. [2010] and Tonina and Buffington [2009a]. Recently, Janssen et al. [2012] have demonstrated that this sequential coupling approach is a valid and sufficiently accurate coupling scheme. However, also direct coupling by simulating stream water and porous media flow in a single model domain has been used [Endreny et al., 2011]. This single domain approach is exact in terms of continuity and conservation of mass. However, the sequential coupling offers more flexibility in the choice of the subsurface model for instance for simulating complex reactive transport of biogeochemical relevant compounds.
These kinds of models are widely used for studying hyporheic exchange, solute transport and reactions on the small scale of 2D bedforms [Jin et al., 2010; Bardini et al., 2012; Hester et al., 2013]. However, up to date, limited numerical experiments were conducted on the intermediate scale of pool-riffle sequences and bars studying water flow and solute transport in three dimensions, although these structures are supposed to be an important contributor to a good stream ecosystem as shown by numerous field studies [e.g. Vervier et al., 1993; Hill et al., 1998; Lansdown et al., 2012; Hartwig and Borchardt, 2014]. Furthermore, on the pool-riffle and gravel bar scale, the effects of ambient groundwater flow on water and solute exchange and their reactions have not been evaluated systematically by using a coupled modeling approach. Hence, closing these knowledge gaps is part of the objectives of this thesis that are described in detail in the following section.

1.4 Objectives and Structure of the Thesis

In this thesis a novel modeling approach has been developed that couples the computational fluid dynamics (CFD) code OpenFOAM with the reactive transport subsurface model MIN3P. The coupling between the two codes is conducted by sequentially transferring the hydraulic heads at the streambed derived by the CFD model to the top of the groundwater model. The CFD code is able to simulate turbulent, shallow stream flow over fully submerged or partially submerged streambed structures by a two-phase model, where both air and water are simulated (Please find additional information to the CFD code in appendix 6.1). Furthermore, by means of particle tracking the residence times and the spatial orientation of the subsurface flow paths are derived. The modeling approach is applied to generic pool-riffle structures and an in-stream gravel bar, occurring naturally at the Selke River, which is an intensive test site of the Helmholtz Association of German Research Centres (`http://teodoor.icg.kfa-juelich.de/observatories/HCGL_Observatory/hydrological-observatory-1/intensive-test-site-selke`). At the field site, multiple hydrological and chemical parameters are measured that are used as input parameters in the model.
The modeling approach is used to address the following objectives:

1. Scale and dimension: Hyporheic processes have been studied primarily on the small (dunes, ripples), the larger (meander) and catchment scale with focus on two-dimensional effects. In this thesis, hyporheic exchange on the intermediate scale of three-dimensional pool-riffle structures and a natural in-stream gravel bar is investigated.

2. Stream flow and degree of submergence: Water levels at structures on the intermediate

scale are often shallow, accompanied with high turbulence and transitions between sub- and supercritical flow regimes indicated by hydraulic jumps. Also, streambed structures can be partially emerged. The effects of shallow water flow and the level of submergence on hyporheic exchange have not been studied systematically in the past and are therefore in the focus of this thesis.

3. Ambient groundwater flow: The impact of losing and gaining conditions on hyporheic exchange on the intermediate scale was rarely considered in previous studies and is therefore part of this thesis.

4. Solute transport and reactions: Solute transport and reactions were measured intensely in field and flume studies but with lacking of knowledge about the distribution of reactive hot spots and its impact of hydrological conditions. Hence, in this thesis the effects of hydrological conditions mentioned above on solute transport and reactions in the hyporheic zone are evaluated. In addition, the effects of various solute concentrations in upwelling groundwater are evaluated.

In Chapter 2, the modeling approach is applied to different pool-riffle morphologies, varying by their maximum amplitude in stream flow direction. In addition, scenarios of variants of stream discharge and the ambient groundwater flow are performed. The impact of these factors on hyporheic exchange flux, hyporheic extent and residence times are systematically evaluated. In addition, the CFD model is tested to a flume experiment to confirm its physical correctness.

In Chapter 3 several groundwater flow scenarios of the study in Chapter 2 are extended by reactive transport simulations. They demonstrate how aerobic respiration and denitrification in the hyporheic zone are controlled by hydrological conditions (stream discharge and ambient groundwater discharge) and pool-riffle amplitude height. In addition, scenarios of varying solute concentration in the upwelling groundwater are performed.

In Chapter 4 the modeling approach is applied to the morphology of a natural in-stream gravel bar, surveyed at the Selke river. Scenarios of varying stream discharge and levels of the ambient groundwater level are simulated. The degree of submergence at the in-stream gravel bar is an additional controlling hydrological factor. Complex patterns of in- and exfiltration locations of hyporheic, losing and gaining flow paths are delineated at the streambed. Reactive potential of the in-stream gravel bar is assessed and is compared to completely submerged streambed structures.

In Chapter 5 the main results of the individual chapters are summarized, concluded in a broader perspective and recommendations for future work are given based on limitations of the used modeling approach.

2 | Coupled 3-D stream flow and hyporheic flow model under varying stream and ambient groundwater flow conditions in a pool-riffle system

This chapter is published as:
Trauth, N., C. Schmidt, U. Maier, M. Vieweg, and J. H. Fleckenstein (2013), Coupled 3-D stream flow and hyporheic flow model under varying stream and ambient groundwater flow conditions in a pool-riffle system, *Water Resources Research*, 49(9): 5834–5850, doi:10.1002/wrcr.20442.

Abstract

Exchange of water and solutes across the stream-sediment interface is an important control for biogeochemical transformations in the hyporheic zone (HZ). In this paper, we investigate the interplay between turbulent stream flow and HZ flow in pool-riffle streams under various ambient groundwater flow conditions. Streambed pressures, derived from a computational fluid dynamics (CFD) model, are assigned at the top of the groundwater model, and fluxes at the bottom of the groundwater model domain represent losing and gaining conditions. Simulations for different Reynolds numbers (Re) and pool-riffle morphologies are performed. Results show increasing hyporheic exchange flows (m^3/d) for larger Re and a concurrent decrease in residence time (RT). Losing and gaining conditions were found to significantly affect the hyporheic flow field and diminish its spatial extent as well as rates of hyporheic exchange flow. The fraction of stream water circulating through the hyporheic zone is in the range of 1×10^{-5} to 1×10^{-6} per meter stream length, decreasing with increasing discharge. Complex distributions of pressure across the streambed cause significant lateral hyporheic flow components with a mean lateral travel distance of 20% of the longitudinal flow paths length. We found that the relationship between pool-riffle height and hyporheic exchange flow is characterized by a threshold in pool-riffle amplitude, beyond which hyporheic exchange flow becomes independent of riffle height. Hyporheic residence time distributions (RTD) are log-normally distributed with medians ranging between 0.7 and 19 h.

2.1 Introduction

Interactions between stream water and groundwater are important for the management of water quantity and quality as well as for the functioning of aquatic ecosystems [Stanford and Ward, 1988; Edwards, 1998; Winter, 1998; Fleckenstein et al., 2010]. The main driver for hyporheic exchange is the variation of pressure along the streambed [Tonina and Buffington, 2009b; Thibodeaux and Boyle, 1987; Buffington and Tonina, 2009]. These pressure variations are produced by stream

flow over dunes, ripples, pool-riffles, or in-stream obstacles. Obstructions can induce variations of the water level causing high pressures at the upstream side and low pressures at the downstream side of the structures. Driven by these pressure variations at the streambed surface, stream water infiltrates into the sediment at the upstream side of the obstruction and exfiltrates back into the stream at the downstream side [Thibodeaux and Boyle, 1987; Harvey and Bencala, 1993; Elliott and Brooks, 1997a,b; Packman et al., 2000; Wörman et al., 2002].

Hyporheic flow paths in natural streams can have large lateral and upstream components as a result of pressure gradients induced by complex three dimensional (3-D) streambed morphology [Tonina and Buffington, 2011, 2007; Angermann et al., 2012]. Large features such as point bars, in-stream gravel bars, and pool-riffle sequences typically show significant lateral variation in morphology and can cause these 3-D patterns of flow [Wörman et al., 2006; Tonina and Buffington, 2007, 2009b; Stonedahl et al., 2010].

Similar to the effects of streambed heterogeneity [e.g. Salehin et al., 2004; Sawyer and Cardenas, 2009], this three dimensionality increases the complexity of hyporheic flow paths resulting in distinct zones of up- and downwelling and a wide range of residence times (RT) [Stonedahl et al., 2010]. Patterns of up- and downwelling affect in-stream habitat and areas for fish spawning [Stuart, 1953; Malcolm et al., 2006; Stuart, 1954; Greig et al., 2007], whereas longer RT foster the transformation of nutrients and other solutes in the streambed [Marzadri et al., 2011, 2012; Zarnetske et al., 2011a; Bardini et al., 2012].

Besides streambed morphology also the velocity of stream flow as well as the magnitude of ambient groundwater flow significantly affect the geometry of the hyporheic zone (HZ). Increasing groundwater discharge decreases the depth and volume of the HZ [Kasahara and Wondzell, 2003; Storey et al., 2003; Cardenas and Wilson, 2007c; Boano et al., 2008, 2009], whereas increasing stream discharge generally increases hyporheic exchange flow [Packman et al., 2004; Tonina and Buffington, 2007; Cardenas and Wilson, 2007a].

Given the complex nature of turbulent flow over 3-D bed forms and the induced hyporheic flows, it is challenging to design appropriate flume experiments or field studies of the groundwater-surface water interface. However, numerical experiments have proven to be a viable alternative to improve our mechanistic understanding of flow dynamics and biogeochemistry in these complex environments [e.g. Cardenas and Wilson, 2007a,b,c; Jin et al., 2010; Bardini et al., 2012; Frei et al., 2012].

Stream water flow over complex streambed morphologies and the resulting pressure at the streambed surface can most accurately be represented using computational fluid dynamics (CFD) codes that solve the full Navier-Stokes equations [Cardenas and Wilson, 2007a; Tonina and Buffington, 2009b; Endreny et al., 2011; Janssen et al., 2012]. Flow simulations can cover a range of Froude numbers (Fr) and include hydraulic jumps and surface water wave phenomena typical of relatively shallow turbulent flow over larger streambed structures such as pool-riffle sequences. These simulations additionally require a two-phase model [Yue et al., 2005; Polatel, 2006], where the exact water level is derived from the interface of the air-water mixture.

In this study, we use a 3-D, two-phase CFD code, which is sequentially coupled to a groundwater flow model, to systematically investigate the dynamics of hyporheic exchange in a pool-riffle stream. Pool-riffle topography is represented by a simplified approximation of a fully submerged pool-riffle sequence. Hyporheic flow scenarios for five different submerged pool-riffle sequences

are systematically evaluated for a range of stream discharges. Additionally, ambient groundwater flow conditions (losing and gaining), which have been disregarded in previous modeling studies of pool-riffle systems [Tonina and Buffington, 2007, 2009b, 2011; Marzadri et al., 2010], are considered at different flow rates. This is thought to be a more realistic conceptualization of pool-riffle streams, which are typically embedded in an alluvial aquifer. Hyporheic RT and the 3-D hyporheic flow field are analyzed by means of particle tracking. With this modeling concept, for the first time, we are able to systematically evaluate how variations in streambed morphology, stream discharge, and ambient groundwater flow affect 3-D hyporheic exchange and RT in pool-riffle streams.

2.2 Methodology

2.2.1 Model Geometry and Parameterization

The streambed morphology represented in the numerical model is inspired by a field site with distinct pool-riffle sequences [Schmidt et al., 2012]. The observed wavelength to width ratio for a pool-riffle sequence at the field site is approximately 1, which is relatively low, compared to commonly reported ratios of approximately 3 to 7 in free formed pool-riffle reaches [e.g. Leopold and Wolman, 1957; Keller, 1972] with a tendency to decrease with increasing slope [e.g. Grant et al., 1990]. However, if sediment transport is influenced by local flow obstructions such as bank protection measures, large wood debris, or boulders [Montgomery et al., 1995], significantly smaller ratios may be found. For example, Montgomery et al. [1995] reported ratios of wavelength to stream width of even less than one in the presence of large wood debris. At the field site, bank protection measures (rip-rap) as well as larger wood debris (from fallen riparian phreatophytes) are frequently found likely explaining the observed small pool-riffle spacing. The main features of the gradually varying pool-riffle morphology at the field site could be approximated empirically by the following equation:

$$Z(x,y) = A\ sin\left(\frac{2\pi}{\lambda}x\right)\ cos\left(\frac{\pi}{w}y\right) \tag{2.1}$$

where x and y represent the respective longitudinal and transverse planar coordinates in stream flow direction. A is the maximum amplitude of the pool-riffle sequence in the stream center, λ is the wavelength in stream flow direction, and w is the stream width. As can be seen from equation 2.1, the height of the morphology varies in y direction by twice the wavelength of the x direction. According to this configuration, the minima and maxima in the streambed elevation are located in the center of the stream. In the y direction from the center line, elevations gradually increase or decrease up to the vertical riverbank (gray surface in Figures 2.1a and 2.1b). Hence, the streambed morphology is symmetric along the stream center (y = 0 m).

We used five different stream water model domains where the bottom geometry differs by the amplitude A of the pool-riffle sequence. The maximum amplitudes A in the stream center are A=[0.1, 0.2, 0.3, 0.4, 0.5] m. The wavelengths are constant with a value of $\lambda = 10$ m, as well as the stream width with $w = 10$ m (Table 2.1). A constant slope of 2 % is assigned to the streambed morphology representing the upper limit of slopes typically occurring in pool-riffle systems [Buffington and Tonina, 2009]. Additionally, our slopes are in the range of values used by Harvey and Bencala [1993] (6.7 %), Woessner [2000] (2 %), and Marzadri et al. [2010] (0.53 to

3.3 %). Meandering of the stream channel is not considered. When referring to the morphologies in the following sections, the abbreviations A01, A02, A03, A04, and A05 are used, according to the maximum amplitude A. In the CFD simulations, up to 12 different discharge scenarios for each streambed morphology were performed. The lower end of the considered range of discharges was determined by the minimum flow required to fully submerge the pool-riffle structures in the model. The largest discharge roughly represents bank full discharge and is close to the mean of the high flow events observed at the field site over the last 50 years (data obtained from the statistical tables of the agency operating the official gauging stations).

The streambed sediment at the field site consists of coarse gravel with finer, mainly sandy sediment fillings in the pore spaces and is covered by an armor layer of cobblestones, which immobilizes the bed for the range of flows considered in our scenarios.

Slug tests were performed to obtain hydraulic conductivity (K) values of the streambed sediments at the field site [Schmidt et al., 2012]. A constant value of $K = 5 \times 10^{-4}$ m/s was set in the groundwater model. The porosity n for the calculation of the pore water velocity was set to 0.3, which is a reasonable value for heterogeneous streambed sediments. The bottom of the groundwater model domain is defined as a flat plane at a depth of 3 m below the baseline of the sinusoidal streambed elevation (Table 2.1).

The surface water model domain comprises a sequence of five pool-riffle sections to avoid boundary effects. Out of these five pool-riffle sequences only the inner three, where effects on the flow from the inlet or outlet conditions of the CFD simulations are assumed to be negligible, are used in the groundwater model. Finally to avoid boundary effects in the groundwater model, hyporheic flow, extent, and RT are only evaluated in the mid pool-riffle sequence of the porous domain.

2.2.2 Numerical Modeling and Coupling

2.2.2.1 Surface Water Model

The OpenSource CFD Toolbox OpenFOAM version 1.7.1 is used to simulate turbulent stream flow over pool-riffle streambeds in order to derive the hydraulic head distribution at the streambed (H). The software solves the three-dimensional Navier-Stokes equations using the finite-volume approach (FVM) and the PISO algorithm for the pressure-velocity coupling. A two-phase model approach, the Volume of Fluid Method (VoF) [Hirt and Nichols, 1981], is used to simulate both the water and the air fraction of the surface water model domain.

For the turbulence closure model, large eddy simulation (LES) is used, because of its high accuracy when working on flow structures with pronounced eddies [Grigoriadis et al., 2009; Janssen et al., 2012]. For simulating the subgrid scales, the original Smagorinsky subgrid scale model [Smagorinsky, 1963] is used with a filter width, determined by the cubic root from the mesh cell volume.

The mesh consists of hexahedral cells with a width of 0.11 m in x and y directions and less than 0.095 m in z direction. The number of computational cells is about 520,000, varying slightly for the different morphologies. Refinement of mesh cells at the bottom boundary (interface to the groundwater model) revealed no significant changes of the streambed pressure, but vastly increased the calculation time.

By specifying adequate initial conditions, the quasi steady state can be reached faster. Prelimi-

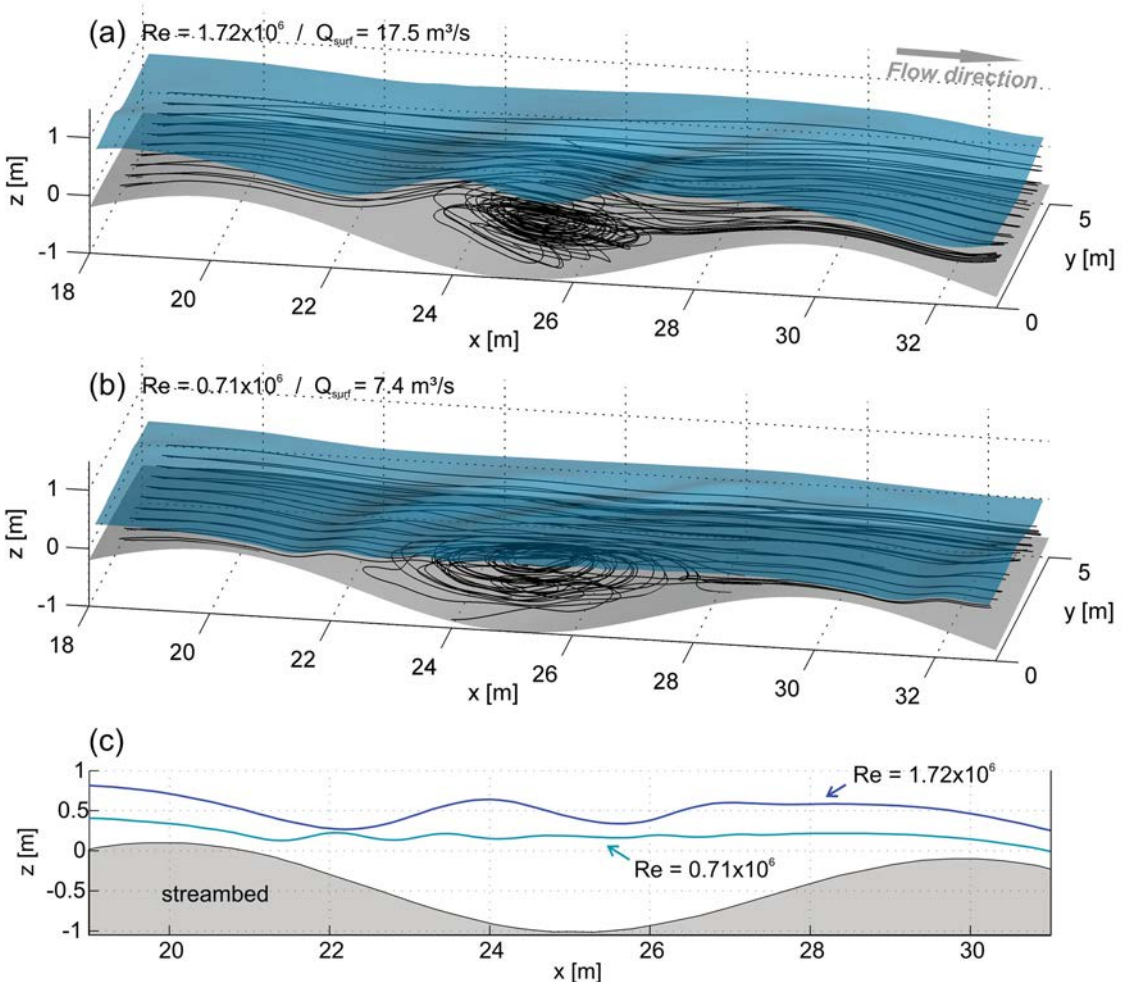

Figure 2.1: Wavy water surface of stream flow for (a) high and (b) low discharge scenarios. Maximum Froude numbers are $Fr = 1.21$ (a) and $Fr = 1.08$ (b) at the downstream side of the riffle. (c) Longitudinal cross section of the stream showing water levels at $y = 0\,\mathrm{m}$ affected by waves induced by undular hydraulic jumps for a high (dark blue line) and a low stream flow (light blue line) scenario. The waves of the low discharge scenario are completely developed within the pool area, while the waves of the high discharge scenario extend into the next riffle structure where they start to interfere with the undular hydraulic jump caused by the next riffle.

nary simulations with a coarse mesh were used to roughly estimate water level and a reasonable velocity field so that the model converges to a quasi-steady state quickly. Subsequently, the mesh is rotated corresponding to the considered slope of 2 % of the stream channel.

The two-phase model requires an inlet boundary condition that defines the fraction of water and air entering the domain. A user-defined application called "GroovyBC" was used to define the inlet condition [Gschaider, 2009, documented at `http://openfoamwiki.net/index.php/Contrib_groovyBC`]. This boundary condition provides the definition of the entering water and air fraction as well as the magnitude and shape of a velocity profile at the inlet, resulting in a defined stream discharge. The inlet condition is constant over time for all model runs, representing steady state stream discharge. A power law function is assigned to the vertical velocity profile at the inlet. Turbulent flow develops shortly after water and air enter the modeling domain. The outlet condition is represented by a boundary that allows both water and air to flow out of the domain unhampered, denoted as *totalPressure* boundary in the OpenFOAM code. The fraction of water and air at the outlet boundary is predicted numerically. The same

Table 2.1: Model Parameters Used for the CFD Simulations and the Groundwater Model MIN3P

Parameter	Value
Stream Configuration	
Stream slope	2 %
Stream width w	10 m
wavelength of pool-riffle sequence λ	10 m
amplitudes of pool-riffle sequence A	0.1, 0.2, 0.3, 0.4, 0.5 m
CFD Code OpenFOAM	
Mesh cell size in x direction	0.11 m
Mesh cell size in y direction	0.11 m
Mesh cell size in z direction	0.095 m and smaller
Groundwater Model MIN3P	
Hydraulic conductivity K	5×10^{-4} m/s
Porosity	0.3
Depth of aquifer	3 m $\pm$ amplitude A
Mesh cell size in x direction	0.2 m
Mesh cell size in y direction	0.2 m
Mesh cell size in z direction	0.1 m

boundary condition is used at the top of the domain, where air can enter and leave the domain, simulating a natural atmospheric condition. For detailed information on the boundary conditions, the reader is referred to the OpenFOAM documentation (`www.openfoam.org`).

The bottom of the domain is bounded by the fixed streambed, which represents the interface between the surface water and the hyporheic zone. The streambed is treated as an impervious no-slip condition in the simulation, which is commonly used in such simulations [Cardenas and Wilson, 2007b; Tonina and Buffington, 2009b; Janssen et al., 2012]. Grain roughness of the streambed is not considered in our model similar to the model approaches of Cardenas and Wilson [2007a,b,c] and Tonina and Buffington [2009b]. This assumption is supported by Janssen et al. [2012], who demonstrated that the effects of wall roughness on the near-bed pressure field are negligible. Furthermore, Lane et al. [2004] compared flow over rough gravel beds versus smooth beds and concluded that sensitivity to rough versus smooth conditions was negligible.

The bank ($y = 5\,\mathrm{m}$) of the stream channel is treated in a similar manner by a no-slip condition. Due to a symmetric stream channel along the stream center ($y = 0\,\mathrm{m}$), only one half of the channel is simulated, which reduces calculation times significantly. Hence, at the stream center a shear-free symmetric boundary condition is used.

OpenFOAM calculates an instantaneous flow field for every time step. For the subsequent statistical analysis of the results, the time-averaged flow field is determined by calculating the averages of the variables over the period of time, after the flow has completely developed and is no longer affected by the initial conditions [Polatel, 2006].

The surface water model is coupled to the subsurface model by assigning H at the streambed surface calculated by the CFD code to the top of a groundwater model as a Dirichlet boundary condition. The mesh cells of the CFD model are approximately half the size of the mesh of the

groundwater model, and therefore, an interpolation over data gaps is not required. This one-way sequential coupling approach captures only flow from the surface water domain into the porous domain and does not account for feedbacks from subsurface flow into the surface water domain. However, hyporheic water that enters the stream channel is only a small volume fraction of the total stream discharge and hence has negligible impacts on hydrodynamic flow in the channel [Prinos, 1995; Cheng and Chiew, 1998].

2.2.2.2 Test of the CFD Model Against Fehlman's Flume Data

To ensure reliable physical behavior of our surface water model, the flume experiments of Fehlman [1985] for flow over triangular bed forms were simulated with the CFD code and the results compared to the experimental data. The bed form geometry of Fehlman's flume, including the flume width, was implemented in an OpenFOAM mesh with a maximum cell width of 0.03 m in all three directions. We adjusted our model parameters to three different runs of Fehlman's experiments, specified by discharge and flume slope (runs 4, 8, and 12). The simulated discharges

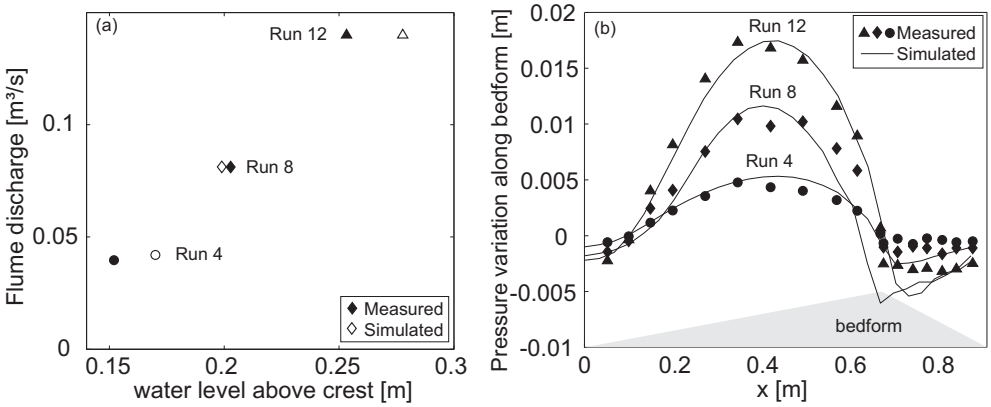

Figure 2.2: Comparison of the simulated data with the measured data of Fehlman's [1985] flume experiment for the runs 4, 8, and 12.

and water levels above the crest agree well with the experimental data (Figure 2.2a). Simulated pressure variations across the bed form normalized by the pressure at the crest also compare well to the experimental data (Figure 2.2b) except at the crest. This is due to the fact that Fehlman did not measure the pressure at the crest and used interpolated values from two adjacent pressure taps located upstream and downstream from the crest. Therefore, the simulated pressure at the crest is significantly lower than the interpolated value from Fehlman, which had already been observed by Cardenas and Wilson [2007a]. However, overall, the simulated bottom pressure agrees well with the measured pressure values (Figure 2.2b and Table 2.2). Our test simulations show that the 3-D surface water model can predict flow over 2-D bed forms with reasonable accuracy. However, this corroboration may not fully extend to our 3-D streambed simulations because of the lack of 3-D pressure head measurements as a validation data set.

2.2.2.3 Groundwater Model

The numerical flow and reactive transport model MIN3P was used to simulate steady state water flow in the HZ. MIN3P is a finite volume flow and transport code that solves Richard's equation for variably saturated flow [Mayer et al., 2002].

Table 2.2: Bias and RMSE of the Measured Pressure Data of Fehlman [1985] and the CFD Simulations

	Run 4	Run 8	Run 12
Bias	3.3×10^{-4} m	2.0×10^{-3} m	2.5×10^{-4} m
RMSE	9.8×10^{-4} m	2.9×10^{-3} m	1.3×10^{-3} m

In a fully saturated domain, as in our case, Richard's equation reduces to the governing groundwater flow equation. The governing equations for incompressible, steady state groundwater flow are:

$$\nabla \cdot \boldsymbol{q} = 0 \tag{2.2}$$

$$\boldsymbol{q} = -K \nabla H \tag{2.3}$$

where $\boldsymbol{q}$ is the Darcy flux, K is the hydraulic conductivity, and ∇H is the gradient of the hydraulic head.

The top of the groundwater model is defined as a Dirichlet boundary with hydraulic head values from the CFD model. At the bottom of the groundwater model domain, at a depth of 3 m below the baseline of the sinusoidal streambed elevation, a Neumann boundary is assigned to control either in- or outflow of water by a Darcy flux denoted as q_{bot}. Gradients, calculated from q_{bot}/K, are within the range of values measured in natural streambeds [e.g. Schmidt et al., 2006; Kennedy et al., 2009; Engelhardt et al., 2011].

For simplicity, we assume that q_{bot} is a uniform flux across the bottom boundary, because of the inherent uncertainty of specifying a realistic spatially varying flux. However, this simplification is supported by results from field studies, which have demonstrated that the variability of vertical flux across the streambed is often small [Shanafield et al., 2010]. Furthermore, gaining and losing exchange fluxes between streams and the underlying aquifer have been shown to be dominated by vertical fluxes across the streambed [Engelhardt et al., 2011], justifying our assumption that lateral fluxes into the stream channel are negligible.

Boundary conditions at the up- and downstream sides as well as at the lateral sides of the model domain are defined by no-flow boundaries.

The mesh of the groundwater model consists of hexahedral cells with maximum vertical extent of less than 0.1 m and 0.2 m in the lateral directions. The elevation of the upper boundary of the groundwater domain follows the streambed morphology.

For each groundwater model scenario, the fluxweighted hyporheic residence time distributions (RTD) and the spatial extent of the HZ were evaluated using forward particle tracking. The proprietary software TECPLOT 360, Version 2011(TecPlot Inc.) was used to calculate particle tracks based on a second-order Runge-Kutta integration of the steady state pore water velocity fields. The integration stops when the particles leave the model domain (TECPLOT User's Manual, 2011). We released massless particles from each streambed boundary node, in total 2,250 (one per node). In the subsequent statistical analysis, only the particles that first enter and then again exit the streambed domain via the top boundary are considered. This defines the hyporheic flow paths and excludes flow paths that describe the flow of water upwelling from the bottom boundary and exiting at the top boundary as well as of water flowing from the top to the bottom boundary.

2.3 Results

2.3.1 Surface Water Flow

2.3.1.1 Stream Discharge, Water Level, and Undular Hydraulic Jumps

In contrast to many natural channels that typically show nonlinear relationships between stage (h_{surf}) and discharge (Q_{surf}), the rating curve is approximately linear in our model (Figure 2.3a). However, when Q_{surf} is approximately $14\,\mathrm{m}^3/\mathrm{s}$, there is a change in the slope of the rating curve, indicating a change in flow conditions at this point. When $Q_{surf} < 14\,\mathrm{m}^3/\mathrm{s}$, the water level rises faster with increasing discharge. When $Q_{surf} > 14\,\mathrm{m}^3/\mathrm{s}$, the water level rises more slowly. This change in the slope of the rating curve coincides with a change of the shape of undular hydraulic jumps that can develop for Fr slightly higher than 1 [Chanson, 2009]. Undular hydraulic jumps are characterized by stationary surface water waves, occurring downstream of the initial water level rise of the hydraulic jump where the flow passes the riffle and enters the pool. The wavelengths and amplitudes of the waves depend on the Fr before the hydraulic jump and the ratio of the average critical depth of the flow over the channel width. Wave amplitudes are damped in the direction of stream flow until they disappear [Chanson and Montes, 1995]. In our simulations, all stream flow scenarios show a wavy water surface with pronounced 3-D structures (Figure 2.1). Q_{surf} is positively correlated with the wavelength and the amplitude and negatively correlated with the number of completely developed waves. For a $Q_{surf} < 14\,\mathrm{m}^3/\mathrm{s}$, the waves of the undular hydraulic jumps in our simulations are restricted to the pool area because the amplitude of the wave is damped to zero before the next downstream riffle starts (light blue line in Figure 2.1c for $Q_{surf} = 7.4\,\mathrm{m}^3/\mathrm{s}$). The flow at the upstream side of the next

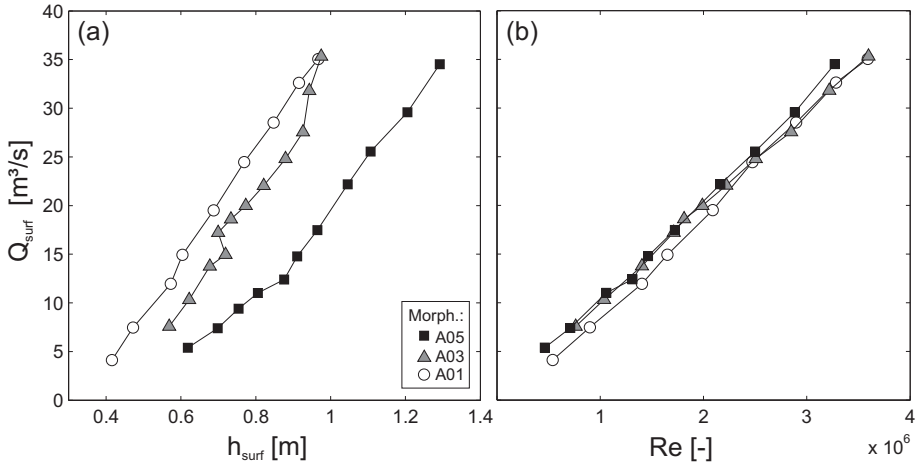

Figure 2.3: (a) Stream discharge (Q_{surf}) as a function of water level (h_{surf}) and (b) as a function of Reynolds number (Re) for three different streambed morphologies.

downstream riffle is not affected by the standing wave of the undular hydraulic jump. This behavior changes at $Q_{surf} > 14\,\mathrm{m}^3/\mathrm{s}$, at which point the wavelength and the amplitude are larger and extend downstream into the zone influenced by the subsequent downstream riffle (dark blue line in Figure 2.1c). The interference of the waves of the undular hydraulic jump with the flow over the subsequent riffle causes a slower rise in the water level relative to the increasing discharge.

Mean Re calculated over all the water columns in the model domain range from 0.5×10^6 to

3.5×10^6. Re numbers increase linearly with Q_{surf} with a constant slope of approximately 1×10^{-5} for all three morphologies (Figure 2.3b). The flow characteristics of the stream scenarios are listed in Table 2.3.

Table 2.3: Stream Flow Characteristics of the CFD Scenarios

Morphology-run	Re [-]	Fr mean [-]	Fr max [-]	H [m]	U [m/s]	Q_{surf} [m^3/s]
A05-1	4.63×10^5	0.44	1.25	0.62	0.93	5.38
A05-2	7.10×10^5	0.48	1.08	0.70	1.15	7.40
A05-3	1.06×10^6	0.57	1.11	0.81	1.48	11.01
A05-4	1.31×10^6	0.60	1.22	0.88	1.67	12.40
A05-5	1.46×10^6	0.63	1.19	0.91	1.76	14.78
A05-6	1.72×10^6	0.67	1.21	0.96	1.95	17.47
A05-7	2.16×10^6	0.75	1.27	1.05	2.27	22.18
A05-8	2.50×10^6	0.77	1.29	1.11	2.43	25.54
A05-9	2.88×10^6	0.79	1.28	1.21	2.59	29.57
A05-10	3.27×10^6	0.83	1.30	1.29	2.78	34.52
A03-1	7.63×10^5	0.65	1.21	0.57	1.46	7.57
A03-2	1.04×10^6	0.74	1.34	0.62	1.76	10.33
A03-3	1.40×10^6	0.89	1.47	0.68	2.21	13.76
A03-4	1.51×10^6	0.87	1.40	0.72	2.22	14.95
A03-5	1.71×10^6	1.02	1.54	0.70	2.58	17.22
A03-6	1.81×10^6	1.03	1.57	0.73	2.65	18.60
A03-7	1.99×10^6	1.01	1.52	0.77	2.70	19.98
A03-8	2.22×10^6	1.01	1.55	0.82	2.80	22.05
A03-9	2.51×10^6	1.03	1.55	0.88	2.95	24.80
A03-10	2.85×10^6	1.03	1.52	0.93	3.09	27.56
A03-11	3.22×10^6	1.12	1.62	0.94	3.39	31.80
A03-12	3.60×10^6	1.16	1.65	0.97	3.61	35.34
A01-1	5.40×10^5	0.68	1.12	0.42	1.35	4.11
A01-2	9.01×10^5	0.91	1.30	0.47	1.94	7.46
A01-3	1.41×10^6	1.05	1.39	0.57	2.47	11.95
A01-4	1.65×10^6	1.15	1.45	0.60	2.78	14.93
A01-5	2.09×10^6	1.16	1.43	0.69	3.02	19.51
A01-6	2.47×10^6	1.18	1.46	0.77	3.24	24.46
A01-7	2.90×10^6	1.19	1.46	0.85	3.42	28.53
A01-8	3.28×10^6	1.21	1.44	0.92	3.60	32.61
A01-9	3.59×10^6	1.20	1.43	0.97	3.70	35.06

2.3.1.2 Eddy Geometry and Hydraulic Head Distribution at the Streambed

In the 3-D simulations, two symmetric eddies develop within the pool area, separated by the stream center line ($y = 0$ m), as expected from the symmetric streambed configurations (see section 2.2.2.1). Due to this symmetry, in the following we refer to the eddies and head distributions in one half of the streambed only.

Stream flow over A03 and A05 produces significant eddies, fully developed in three dimensions, whereas the eddies that develop for flow over A01 are very small. The eddies are located in the deepest pool area close to the stream centerline, while close to the stream bank amplitudes

in streambed elevation are too small for eddy formation. The pool area covered by eddies is approximately 65 % of the stream width for flows over A05 and 50 % of the stream width for flows over A03.

Different discharge scenarios (different Re) also influence eddy geometry. Eddies in the low discharge model runs are relatively flat and cover the whole pool area in flow direction (Figure 2.1a). Under high discharge conditions, the eddies show more circular shapes and are only located deep in the pool, accompanied with lower detachment and reattachment points (Figure 2.1b). A change between these two general eddy geometries occurs at Re of about 1.4×10^6, where also the slope of the rating curve increases and where the waves of the undular hydraulic jump can affect the flow over the next riffle.

Figure 2.4 depicts hydraulic head distributions at the streambed for the different scenarios. Generally, maximum heads (H_{max}) are located at the upstream side of the riffle and correspond to the reattachment points of the eddy. From the maximum, the head decreases in the direction of stream flow until a minimum (H_{min}) is reached at the lee side of the riffle, where the next

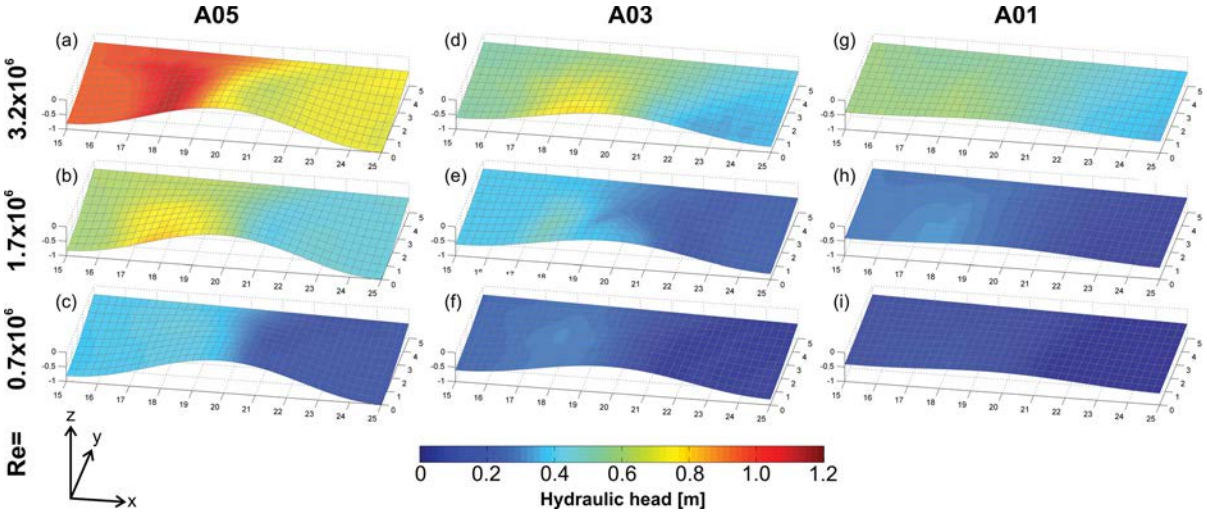

Figure 2.4: Hydraulic head (H) distribution at the streambed for high, moderate, and low Re scenarios for three pool-riffle amplitudes (columns). Flow is from left to right.

eddy detaches. The H differences are significantly higher in A05 and A03 than in A01 and increase with Re. This is most notable at the location of the H_{max} and H_{min} where a shift in their x direction coordinate will depend on changing discharge and morphology: The higher the discharge, the longer the distance between the locations of H_{max} and H_{min} (e.g., compare Figures 2.4a and 2.4c). This is accompanied by smaller eddies in the pool and a lower z elevation of the H maxima. Similarly, the distance between H_{max} and H_{min} increases with lower pool-riffle amplitude. The same effect is also visible at each individual riffle as a result of the decline in amplitude toward the river bank ($y = 5\,\mathrm{m}$). H also varies along the lateral direction of the streambed. The distance between H_{max} and H_{min} along the x direction increases toward the stream bank (Figure 2.4). Interestingly, the absolute H_{max} and H_{min} are not located at the center of the stream ($y = 0\,\mathrm{m}$), but rather some distance toward the stream bank. This distance strongly depends on the discharge. For high discharges, H maxima are located closer to the stream center and vice versa (Figure 2.4). The location of the absolute H_{max} at the streambed corresponds to the maximum longitudinal extent of the eddies, which is not located at the stream center, but rather a certain distance toward the stream bank.

Our results also demonstrate the effects of the undular hydraulic jumps that develop downstream of the riffles on the H distribution at the streambed. The standing waves have distinct wavelengths and amplitudes that increase with discharge. When a wave trough (respectively low hydrostatic pressure) coincides with the upstream side of a riffle, where H is commonly high, the resulting H will be reduced causing local anomalies (clearly visible at $x = 19\,\mathrm{m}$ in Figure 2.4e). Due to the three-dimensional nature of the waves (see Figure 2.1), interferences can occur at particular locations at the streambed and do not necessarily extend over the entire channel width.

2.3.2 Hyporheic Exchange

We define the hyporheic exchange flow (Q_{HZ}) as the water volume per time (in m^3/d) that enters and subsequently exits the porous domain at the top of the HZ. Infiltrating stream water that exits the domain via the bottom boundary and groundwater that enters the domain via the bottom boundary and exfiltrates into the stream is not included in Q_{HZ}. As described in the methods section, Q_{HZ} is evaluated for a single pool-riffle sequence ($\lambda = 10\,\mathrm{m}$). In the following sections, the effects of Re, q_{bot}, and the different streambed morphologies on Q_{HZ} are described.

2.3.2.1 Effects of Reynolds Number

The Q_{HZ} generally increases with Re for the morphologies A05 and A03 (Figures 2.5a and 2.5b), independent of the direction of q_{bot}. This is caused by an overall increase of the hydraulic head gradient at the streambed with increasing Re, respective Q_{surf}. However, the relation is not monotonically increasing and a meaningful correlation is not derivable. For example, in simulation A03, the Q_{HZ} is remarkably reduced for Re of 1.5×10^6 to 2.0×10^6 and reduced even further for very high Re of 3.5×10^6. For A05, variations of Q_{HZ} in this Re range are visible, but not as significant as for A03. A possible explanation for this behavior is that the local reduction of H is caused by the undular hydraulic jumps that develop downstream of the riffles. As a result, the head gradient between the upstream and downstream side of the riffle is reduced causing a decrease in Q_{HZ}.

2.3.2.2 Effects of Ambient Groundwater Flow

Our simulations show strong effects of ambient groundwater flow, represented by the inflow and outflow via the bottom boundary of the groundwater model on hyporheic exchange. For the neutral case ($q_{bot} = 0\,\mathrm{m/d}$), Q_{HZ} and the extent of the hyporheic flow cell are at a maximum. An increase in the magnitude of q_{bot} results in a decrease of Q_{HZ} for both the losing and the gaining case. Even low magnitudes of q_{bot} have a significant impact on Q_{HZ}. Exchange flows for both gaining and losing conditions are of the same order of magnitude and change similarly with the magnitude of q_{bot} for a given morphology (Figures 2.5a and 2.5c). However, under losing conditions, Q_{HZ} is consistently slightly lower than under gaining conditions.

Figure 2.6a shows the relationship between dimensionless ${q_{bot}}^*$ calculated as q_{bot}/K (equals the vertical gradient at the lower boundary condition) and the ratio of Q_{HZ}/Q_{surf} for high and low Re, which can be well approximated by an exponential function. Based on these equations (coefficients for all scenarios are provided in Table 2.4), the ratio of Q_{HZ}/Q_{surf} can be estimated for a given ${q_{bot}}^*$ and Re. Furthermore, a critical ${q_{bot}}^*$ can be derived, defined as the ${q_{bot}}^*$ value for which all hyporheic exchange is completely suppressed. As the exponential curves

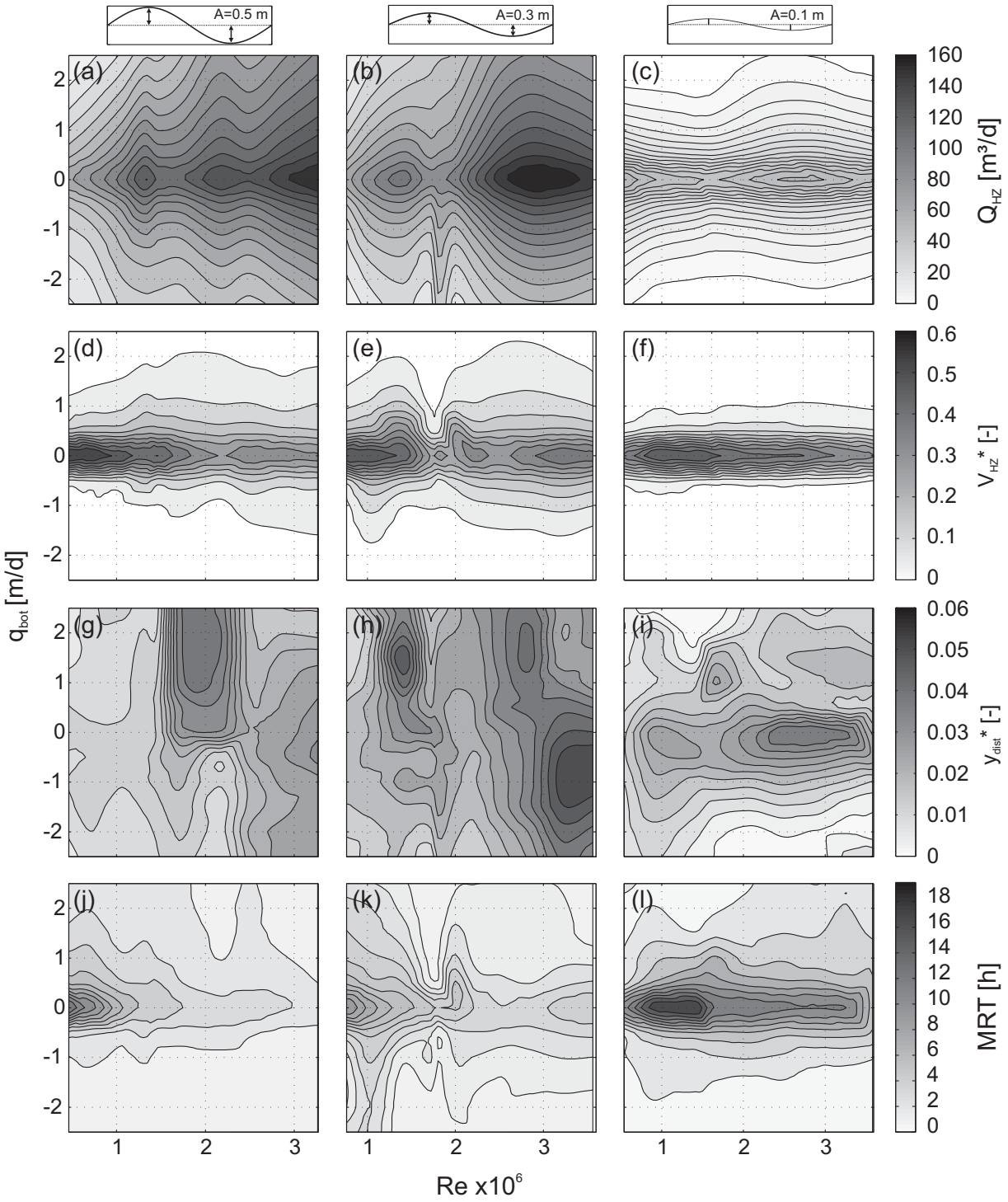

Figure 2.5: Effect of Re and ambient groundwater flow (q_{bot}) on (a to c) Q_{HZ}, (d to f) $V_{HZ}{}^*$, (g to i) $y_{dist}{}^*$, and (j to l) MRT. Negative q_{bot} indicate losing conditions and positive q_{bot} gaining conditions. The three columns refer to the streambed morphologies A05, A03, and A01.

are asymptotic toward $Q_{HZ}/Q_{surf} = 0$, we define a limit for hyporheic exchange at 1 % of the maximum Q_{HZ}/Q_{surf} (at $q_{bot}{}^* = 0$ m/d) and denote the corresponding $q_{bot}{}^*$ value as the critical $q_{bot}{}^*$ (shown as a function of Re in Figure 2.6b). The critical $q_{bot}{}^*$ values increase with Re, because higher Re induces higher H gradients across the riffle, which in turn require higher $q_{bot}{}^*$ values to completely suppress hyporheic flow (except for morphology A01). Under losing conditions, the critical $q_{bot}{}^*$ values do not increase with Re as fast as under gaining conditions. In the high Re scenarios, the critical $q_{bot}{}^*$ is up to twice as high under gaining than under losing conditions.

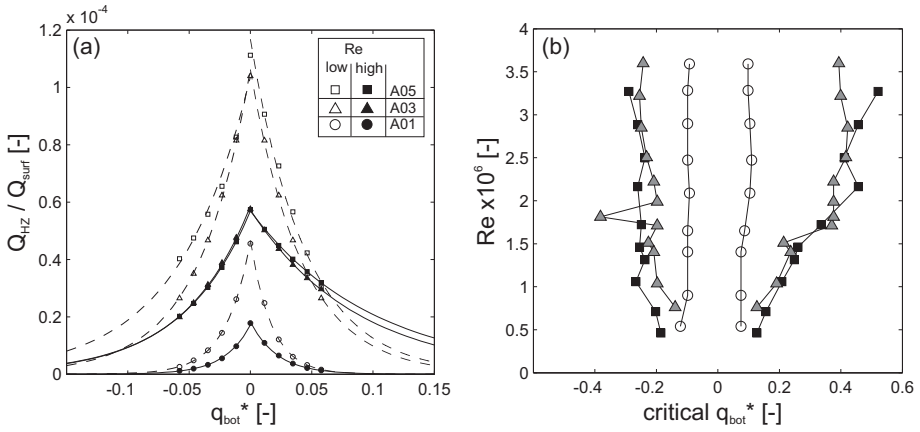

Figure 2.6: (a) Fitted exponential curves for the relationship between $q_{bot}{}^*$ and Q_{HZ}/Q_{surf} for high and low Re scenarios of runs A05–3, A05–10, A03–2, A03–11, A01–2, and A01–8 (see Table 2.3). R^2 is $>$ 0.97 for all scenarios. (b) Critical $q_{bot}{}^*$ as a function of Re. Critical $q_{bot}{}^*$ is derived from the exponential curves in (a) where $Q_{HZ}/Q_{surf} < 1\,\%$ of the maximum Q_{HZ}/Q_{surf} (at $q_{bot}{}^* = 0$ m/d).

2.3.2.3 Effects of Streambed Morphology

As described in section 2.3.2.1, there is a general positive correlation between Re and Q_{HZ} for A03 and A05. In contrast, Q_{HZ} for flow of A01 (Figure 2.5c) does not show the same dependency on increasing discharge, and the Q_{HZ} contours depicted in Figure 2.5c are significantly different for A01 compared to A03 and A05. Also the critical $q_{bot}{}^*$ values (Figure 2.6b) hardly vary with Re for A01.

At first sight this seems to suggest a general positive correlation between the magnitude of Q_{HZ} and streambed amplitude. However, a closer look at the contour plots of A03 and A05 reveals very similar distributions and magnitudes of Q_{HZ} for both of these scenarios. This implies that above a certain pool-riffle height, a further increase in height has no significant effect on Q_{HZ}, which remains at a quasi-constant level beyond this threshold.

For further evaluation of this possible threshold in pool-riffle height, Figure 2.7 shows how Q_{HZ} is related to the pool-riffle amplitude and q_{bot} under constant $Re = 1.4 \times 10^6$. The Q_{HZ} values on the y axis are normalized to Q_{HZ} of morphology A01. The upper graph (Figure 2.7a) shows that for gaining conditions, Q_{HZ} is relatively constant for pool-riffle amplitude heights above A = 0.1 m. For losing conditions, the relationship between amplitude A and Q_{HZ} levels of beyond $A = 0.2$ m. The rate of increase in Q_{HZ} with amplitude (the slope of the graphs in Figure 2.7) before the threshold (beyond which Q_{HZ} remains quasi-constant) generally increases with q_{bot}. This effect is more pronounced for gaining conditions than for losing conditions.

Table 2.4: Fitting Parameters for the Relationship Between $q_{bot}{}^*$ and Q_{HZ}/Q_{surf} for Exponential Functions of the Type $Q_{HZ}/Q_{surf} = \text{a} \times e^{bq_{bot}{}^*}$. For all scenarios $R^2 > 0.97$

		Losing		Gaining	
Morphology-run	*Re*	a	b	a	b
A05-1	4.63×10^5	1.42×10^{-4}	24.750	1.71×10^{-4}	-36.505
A05-2	7.10×10^5	1.20×10^{-4}	22.828	1.40×10^{-4}	-29.016
A05-3	1.06×10^6	1.04×10^{-4}	17.051	1.17×10^{-4}	-22.290
A05-4	1.31×10^6	1.18×10^{-4}	19.672	1.26×10^{-4}	-18.628
A05-5	1.46×10^6	8.82×10^{-5}	17.937	9.53×10^{-5}	-17.537
A05-6	1.72×10^6	7.46×10^{-5}	18.645	7.84×10^{-5}	-13.621
A05-7	2.16×10^6	7.00×10^{-5}	17.840	7.10×10^{-5}	-10.033
A05-8	2.50×10^6	5.82×10^{-5}	19.398	5.89×10^{-5}	-11.066
A05-9	2.88×10^6	5.69×10^{-5}	18.008	5.69×10^{-5}	-10.051
A05-10	3.27×10^6	5.25×10^{-5}	15.939	5.25×10^{-5}	-8.813
A03-1	7.63×10^5	1.09×10^{-4}	33.277	1.17×10^{-4}	-35.464
A03-2	1.04×10^6	1.06×10^{-4}	23.833	1.06×10^{-4}	-23.833
A03-3	1.40×10^6	8.28×10^{-5}	21.940	8.70×10^{-5}	-19.226
A03-4	1.51×10^6	8.65×10^{-5}	20.456	9.15×10^{-5}	-21.122
A03-5	1.71×10^6	5.85×10^{-5}	23.879	5.80×10^{-5}	-12.167
A03-6	1.81×10^6	5.60×10^{-5}	12.001	5.60×10^{-5}	-12.001
A03-7	1.99×10^6	5.61×10^{-5}	23.528	5.61×10^{-5}	-12.111
A03-8	2.22×10^6	6.39×10^{-5}	22.134	6.37×10^{-5}	-12.034
A03-9	2.51×10^6	6.96×10^{-5}	20.043	6.85×10^{-5}	-10.971
A03-10	2.85×10^6	6.94×10^{-5}	18.747	6.77×10^{-5}	-10.775
A03-11	3.22×10^6	5.86×10^{-5}	18.442	5.73×10^{-5}	-11.520
A03-12	3.60×10^6	4.89×10^{-5}	19.086	4.74×10^{-5}	-11.613
A01-1	5.40×10^5	1.65×10^{-4}	39.750	1.85×10^{-4}	-60.913
A01-2	9.01×10^5	8.17×10^{-5}	47.839	8.49×10^{-5}	-59.012
A01-3	1.41×10^6	4.59×10^{-5}	49.446	4.67×10^{-5}	-58.069
A01-4	1.65×10^6	3.32×10^{-5}	47.958	3.41×10^{-5}	-51.071
A01-5	2.09×10^6	2.87×10^{-5}	50.379	2.85×10^{-5}	-42.205
A01-6	2.47×10^6	2.51×10^{-5}	49.393	2.51×10^{-5}	-40.536
A01-7	2.90×10^6	2.11×10^{-5}	46.653	2.21×10^{-5}	-42.207
A01-8	3.28×10^6	1.71×10^{-5}	47.460	1.82×10^{-5}	-45.809
A01-9	3.59×10^6	1.49×10^{-5}	49.297	1.55×10^{-5}	-46.100

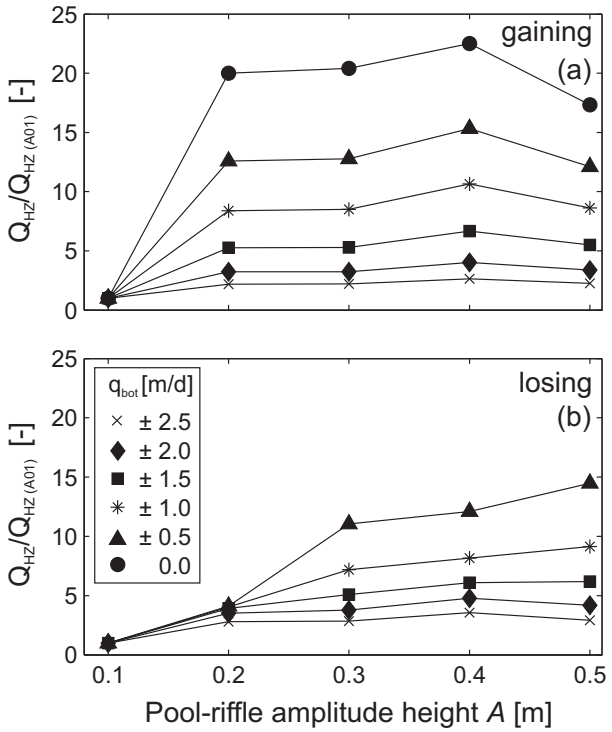

Figure 2.7: Hyporheic exchange flow as a function of maximum pool-riffle amplitude height (A) under constant stream discharge of $Q_{surf} = 12\,\mathrm{m}^3/\mathrm{s}$. All Q_{HZ} values are normalized to Q_{HZ} of the scenario with a maximum amplitude height of $A = 0.1\,\mathrm{m}$.

2.3.2.4 3-D Hyporheic Zone Volume and Lateral Flow

Based on the results of the 3-D particle tracking, the water volume of the hyporheic flow cells (V_{HZ}) enclosed by the outermost flow paths returning to the stream can be derived (Figure 2.8). The ratio between V_{HZ} and the total water volume stored in the entire porous domain is denoted as the dimensionless hyporheic volume $V_{HZ}{}^*$. Contour plots of $V_{HZ}{}^*$ versus Re and q_{bot} are shown in Figures 2.5d to 2.5f. For the neutral case ($q_{bot} = 0\,\mathrm{m}$), $V_{HZ}{}^*$ slightly decreases with increasing Re and shows maximum values for low Re. In contrast, under losing and gaining conditions $V_{HZ}{}^*$ slightly increases with increasing Re or stays relatively constant. The inverse relation of $V_{HZ}{}^*$ to Re under losing/gaining and neutral conditions could be an effect of the no-flow boundary condition at 3 m depth representing the aquifer bottom. Under neutral conditions, this no-flow boundary restricts the full development of the major and minor hyporheic flow cells, which increases with Re. The space between major and minor flow cells also increases with Re and thus, less aquifer volume is affected by hyporheic flow. For gaining and losing conditions, the hyporheic flow cells do not reach the bottom of the domain, so this effect does not occur.

When the magnitude of q_{bot} exceeds 2 m/d for both the gaining and losing cases, $V_{HZ}{}^*$ is less than 5a small vertical extent of the HZ (Figures 2.5d and 2.5f). However, Q_{HZ} is still significant even for low magnitudes of q_{bot} (Figures 2.5a and 2.5c), indicating significant hyporheic flow even for small HZ volumes. Also, the low $V_{HZ}{}^*$ values for Re between 1.5×10^6 and 2×10^6 in A03 indicate a reduction of the HZ volume (Figure 2.5h), probably caused by the effects of undular hydraulic jumps as described earlier.

Major differences in $V_{HZ}{}^*$ are visible between A05, A03, and the shallow morphology A01. $V_{HZ}{}^*$ in A01 shows a sharper decline with increasing Re than in A03 and A05. Furthermore, $V_{HZ}{}^*$ in

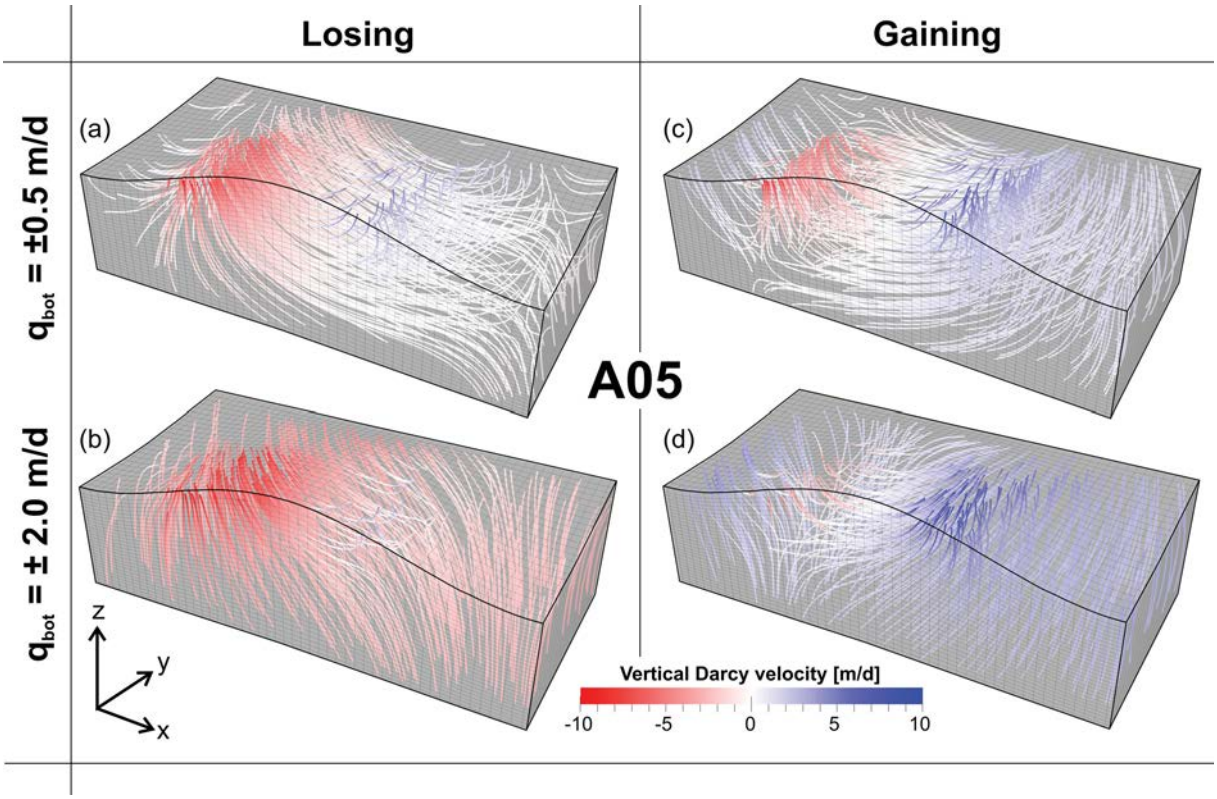

Figure 2.8: Hyporheic flow paths for A05 morphology for a high discharge scenario of $Re = 1.72 \times 10^6$ (H distribution of Figure 2.4b) of high and low q_{bot} magnitudes for the gaining and losing case. Red colors (negative vertical Darcy velocity) indicate infiltration and blue colors (positive vertical Darcy velocity) exfiltration to the streambed.

A01 is more sensitive to q_{bot}, indicated by steeper $V_{HZ}{}^* / q_{bot}$ gradients compared to A03 and A05.

Two distinct flow cells in the HZ can be distinguished: a major and a minor one (Figures 2.8, 2.9, and 2.10). Flow paths in the major flow cell, located around the crest, are directed downstream with a lateral flow component toward the stream bank. Flow paths that are directed upstream form a minor flow cell with the infiltration zone at a lower location on the stoss side of the riffle and an exfiltration zone close to the upstream pool with a lateral flow direction toward the stream center. This complex 3-D flow field is caused by the spatial variation of H across the streambed (see section above) resulting from the 3-D morphologies. It is additionally influenced by the direction and magnitude of ambient groundwater flow across the bottom boundary. For gaining conditions, the bulk of the stream water is infiltrating at the upstream side of the riffle and subsequently returns to the stream at the downstream side. The general lateral direction of flow in this cell under gaining condition is toward the stream bank. Flow paths that are oriented in the opposite direction (minor flow cell) return to the stream close to the upstream pool center and are laterally deflected toward the stream center (Figures 2.8c and 2.8d and 2.10, right column). Flow cells that develop under losing conditions look quite different. Here large fractions of stream water that infiltrate at the upstream side of a riffle do not return to the stream, but instead leave the model domain at the bottom boundary (Figures 2.8a and 2.8b). Areas of infiltration at the streambed with subsequent return to the stream are pushed toward the crest of the riffle (Figure 2.10, left column). In contrast to the gaining case, the general lateral flow component in this major flow cell is toward the stream center. For high

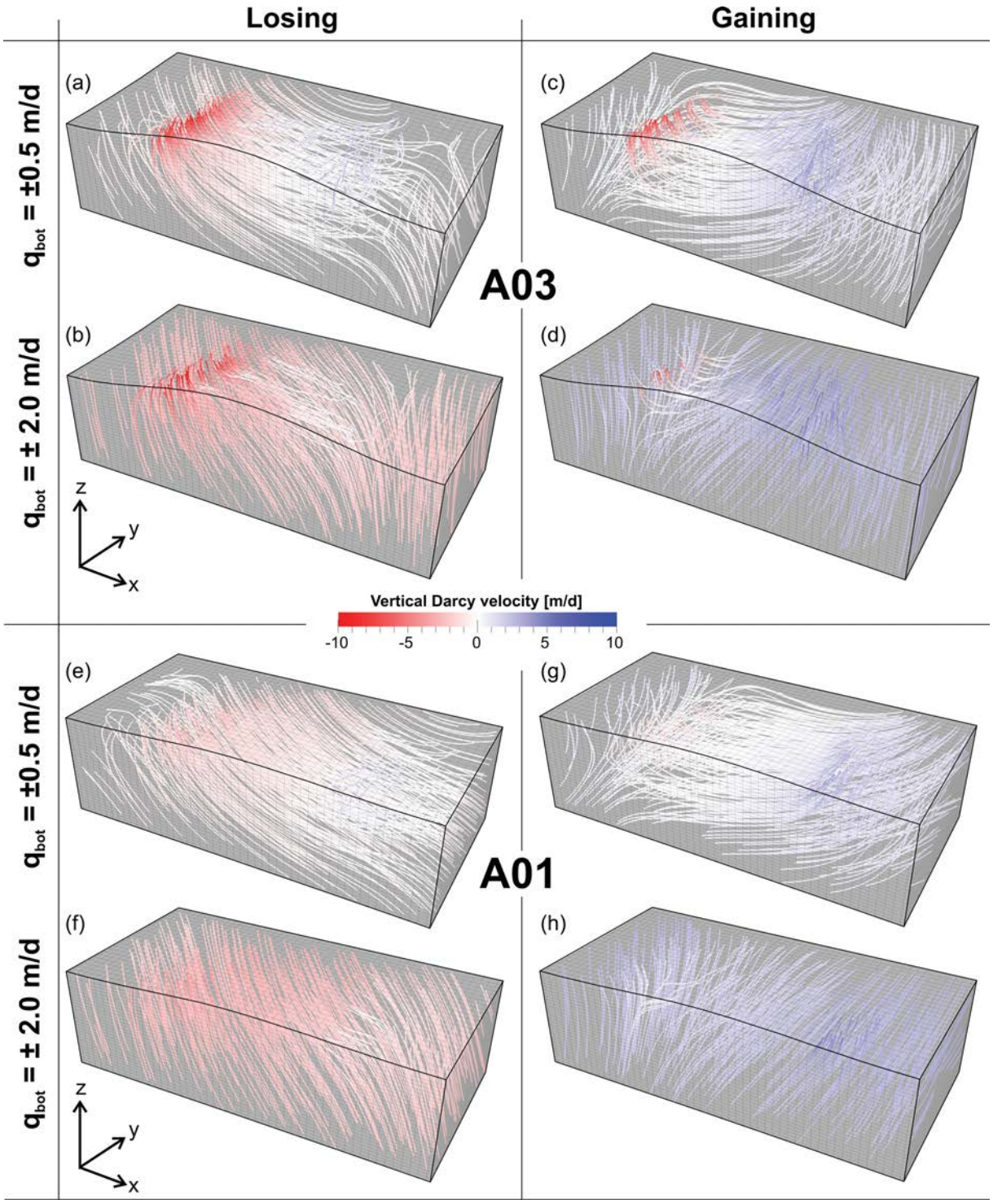

Figure 2.9: Hyporheic flow paths for A03 and A01 morphology for discharge scenarios of $Re = 1.72 \times 10^6$ (H distribution of Figure 2.4e and h) of high and low q_{bot} magnitudes under gaining and losing conditions. Red colors (negative vertical Darcy velocities) indicate infiltration and blue colors (positive vertical Darcy velocities) exfiltration to the streambed.

Re (1.72×10^6) or low magnitudes of q_{bot} a smaller hyporheic flow cell can develop toward the upstream pool (Figures 2.10a to 2.10d), which is also directed toward the stream center. With respect to the impact of q_{bot}, it can generally be stated that: (1) the higher q_{bot}, the smaller the areal extent of the infiltration and exfiltration zones, and (2) for high magnitudes of q_{bot} no distinct minor flow cell develops and only the major flow cell remains but is cropped close to the stream bank (Figures 2.8b and 2.10c,d,g,h,k,l,o,p), and (3) the lateral flow directions in the major flow cells show opposite patterns in the gaining (toward stream bank) and in the losing case (toward stream center).

The maximum vertical flow velocities of the particle paths are found at the infiltration and exfiltration points (red and blue colors in Figures 2.8 and 2.10b,d,f,h,j,l,n,p). Infiltration and exfiltration velocities at the streambed increase with Re, due to higher H gradients and are independent of q_{bot}. Vertical velocities are smallest at the maximum depth of each particle path (white color in Figure 2.8).

To quantitatively evaluate the lateral flow components, we define the dimensionless distance $y_{dist}{}^*$ as the absolute lateral travel distance y_{dist} normalized by the stream width (10 m). In Figures 2.5g to 2.5i the mean values of $y_{dist}{}^*$ versus Re and q_{bot} are presented. The magnitude and direction of lateral shifts mainly depend on the hydraulic heads (and thus on Re) at the location of infiltration. Additionally, the direction and magnitude of q_{bot} influences the lateral shift. Overall, y_{dist} is rarely higher than 50 % of the longitudinal travel distance. Generally, the lateral travel distance increases slightly with Re for all morphologies. Ambient groundwater flow does not consistently influence $y_{dist}{}^*$. For A01, $y_{dist}{}^*$ decreases with increasing q_{bot} for both gaining and losing conditions. This relationship cannot be observed for A05 and A03.

2.3.2.5 Hyporheic Residence Times

Flux-weighted RT in the HZ (only flow paths that enter the HZ from the stream and subsequently return to the stream are considered) were evaluated based on the results of the forward particle tracking. Simulated median RT (MRT) range from 0.7 to 19 h (Figures 2.5j to 2.5l). Plotted against Re and q_{bot} they show similar spatial patterns as the distributions of Q_{HZ} shown in Figures 2.5a to 2.5c. Figures 2.5a to 2.5c also show that MRT is mainly affected by the magnitude of q_{bot} and not by its direction. MRT are generally shorter for increasing magnitudes of q_{bot}. However, MRT are shorter under losing conditions compared to gaining conditions despite relatively similar Q_{HZ}. This indicates faster hyporheic flow for the losing case. For all three morphologies, the longest RT occurs in the case of no bottom inflow or outflow.

Increasing Re results in shorter MRT for all three morphologies. The longest MRT occur under low Re, where very low exchange flows appear and vice versa. This indicates a higher hyporheic flow velocity under high Re, accompanied with shorter MRT and higher Q_{HZ}.

In contrast to the distribution of Q_{HZ} (Figures 2.5a to 2.5c), the MRT for the three different morphologies are within one order of magnitude, where the longest MRT can be observed for the shallowest morphology A01. Stream flows over steep morphologies produce high Q_{HZ} (A03, A05), due to a fast flow through the HZ, which leads to shorter RT but long flow paths. In contrast, for the shallow morphology (A01), flow velocities are slower, and consequently, the RT are larger.

For the scenarios shown in Figure 2.10, histograms of the RT and fitted log-normal curves are

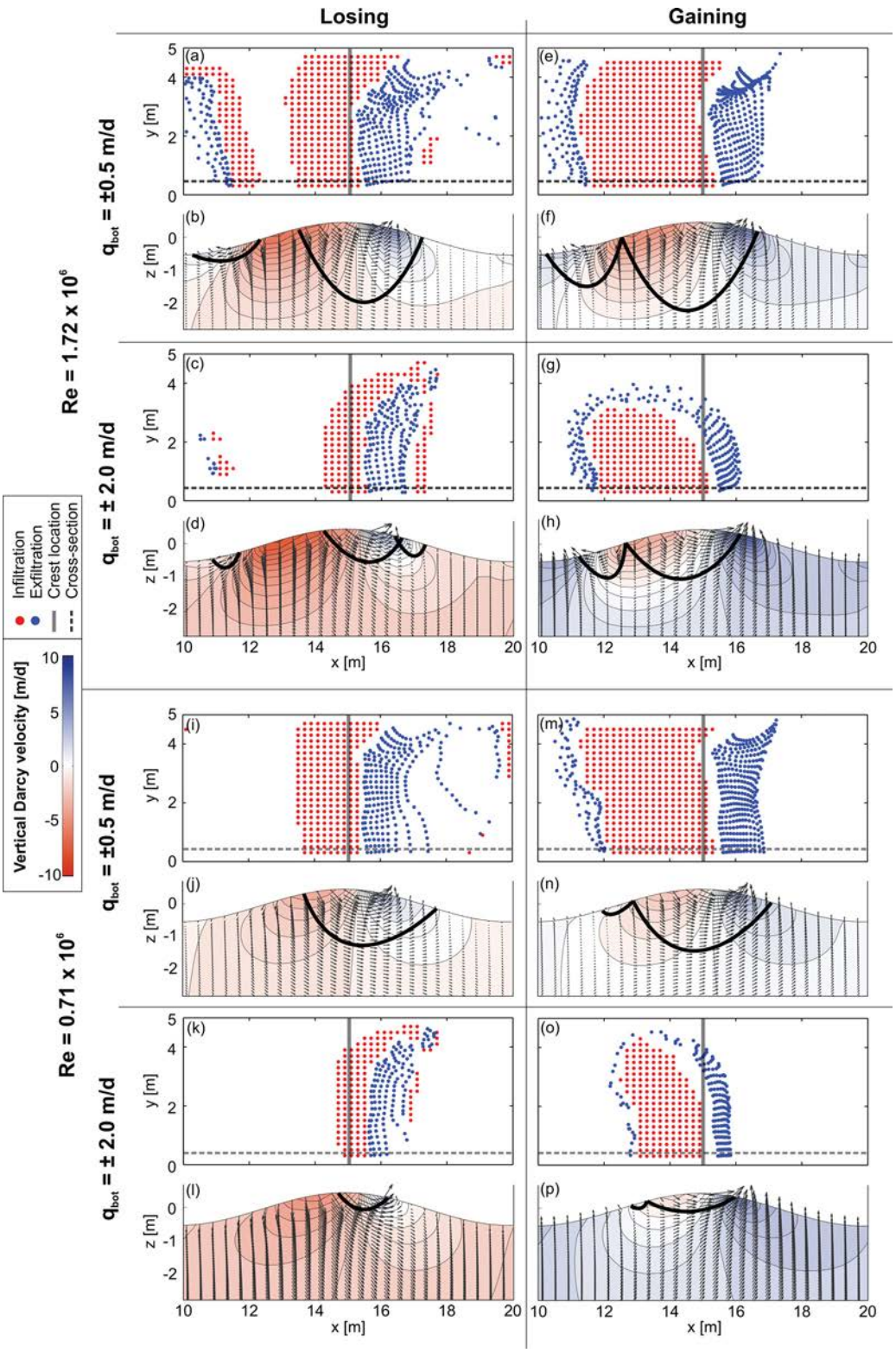

Figure 2.10: (a, c, e, g, i, k, m, o) Locations of infiltration and subsequent exfiltration at the streambed in the x–y plane for the two Re scenarios presented in Figures 2.1, 2.4b, and 2.4c for different directions and magnitudes of q_{bot}. The start- and end-points of the flow paths are shown that define hyporheic exchange (infiltration into and subsequent exfiltration out of the streambed). Flow paths that leave or enter the domain at the bottom boundary are not considered. (b, d, f, h, j, l, n, p) Cross sections along the x–z plane at location $y = 0.4\,\mathrm{m}$ (dashed line in top). The contours represent vertical Darcy velocities and vectors depict the direction of the flow. The bold black lines indicate the maximum vertical extent of the hyporheic flow cells. Stream flow direction is from left to right.

shown in Figure 2.11. RT for all scenarios are well represented by a lognormal distribution. The RTD do not show significant variations neither between the losing and gaining cases nor between the high and low *Re* scenarios. Also the RTD for the three different morphologies are very similar (data not shown).

2.4 Discussion

2.4.1 Variation of Hydraulic Head at the Streambed and Effects of Undular Hydraulic Jumps

Natural stream flows in channels with pool-riffle structures typically result in complex configurations of the stream water level including (undular) hydraulic jumps [Tonina and Buffington, 2007, 2011]. Such variations in the water level together with pressure effects caused by turbulent flow are the dominant controls of pressure variations at the streambed, which in turn drive hyporheic flow through the streambed [Packman et al., 2004; Cardenas and Wilson, 2007a,b,c; Tonina and Buffington, 2007, 2011]. Hence, an accurate representation of water level and turbulent effects is indispensable when simulating hyporheic exchange flows in river reaches with pronounced pool-riffle structures [Tonina and Buffington, 2007, 2011, 2009b; Endreny et al., 2011]. The two-phase CFD approach in this study complies with these requirements. Water levels in our simulations are determined using the VoFapproach and locally deviate by up to 0.45 m from the mean water level. Using a simpler one-phase model would have resulted in significant errors in the pressure distributions at the streambed. By comparing the water level with the hydraulic head, our work provides further evidence that in complex channels the water level is not a good surrogate for the hydraulic head distribution at the streambed. These findings corroborate the results of Tonina and Buffington [2007] from flume experiments. The overall difference between H_{max} and H_{min} depends on *Re*, and the location of the H_{max} and H_{min} on the ratio between dune height and dune length. Furthermore, the distance between the extreme values is larger for lower ratios, as in our results for the different morphologies. However, the H_{max} and H_{min} at the upstream and downstream side of a riffle vary significantly in the lateral direction and hence also induce lateral hyporheic flow components. At the upstream side, H decreases from the stream center to the bank, whereas H increases toward the stream bank at the downstream side of the riffle. Absolute H maxima are always located closer to the stream center than the H minima. This setting generates a lateral gradient toward the stream bank in addition to the major longitudinal gradient between the upstream side and downstream side of a riffle. A small depression of H located next to the pool close to the stream centre evokes hyporheic flow cells that points upstream and toward the stream center (Figure 2.4).

For the first time in pool-riffle systems, we show that surface water waves produced by undular hydraulic jumps can cause local anomalies in streambed pressure. We found that when the trough of the standing wave coincides with the region of highest streambed pressures in the reattachment zone of the eddy, H at the streambed is significantly reduced. This effect alters the H distribution across the streambed and in turn affects the 3-D hyporheic flow field. The severity of these effects depends on the magnitude of stream discharge.

Also, the complex head distribution simulated by the CFD model results from the specific, field-inspired, 3-D streambed morphology. Streambed morphology at the site is affected by bank

protection measures (e.g. rip-rap) and large woody debris, which constrains sediment dynamics resulting in a small ratio of pool-riffle wavelength to stream width (~ 1) [Montgomery et al., 1995]. To our knowledge, hydraulic head distributions and hyporheic flows in such pool-riffle systems have not been studied systematically. Probably, higher ratios of pool-riffle wavelength to stream width would diminish the effect of standing wave interference. Furthermore, stream flow could adapt more smoothly to the morphology, likely resulting in less lateral variations of hydraulic head and, hence, a decrease in the lateral hyporheic flow component.
However, further investigations regarding the impact of morphology on hyporheic flow are needed to evaluate the dependence of Q_{HZ} on the ratios between wavelength to width as well as ratios between wavelength and amplitude.

2.4.2 3-D Hyporheic Flow Paths

The pronounced variations of H at the streambed induce complex 3-D hyporheic flow paths with flow components in both longitudinal and lateral directions (Figures 2.8, 2.9 and 2.10). Lateral flow distances (y_{dist}) were on average 20 % of the longitudinal flow distance. The y_{dist} increased only slightly with Re; however, the effect of Re is evident in longitudinal direction where increasing Re results in deeper and longer hyporheic flow paths. We suspect that pronounced lateral flow components may support an enhanced mixing of stream water and groundwater in the hyporheic zone.
The 3-D hyporheic flow paths were strongly affected by ambient groundwater flow. Most notably regarding the shapes of the hyporheic flow cells and the spatial patterns of infiltration and exfiltration zones, which were found to be significantly different between the gaining and losing case (Figures 2.8, 2.9 and 2.10). Under gaining conditions, one single infiltration area exists, and flow paths are separated into two distinct hyporheic flow cells, one in downstream and one in upstream direction (Figures 2.10e,f,g,h,m,n,o,p). For the losing case, two noncontiguous infiltration areas with completely separated flow cells develop, particularly pronounced for high Re (Figures 2.10a and 2.10b). This separation is forced by the fast downward flow located close to the maximum in H at the upstream side of the riffle (Figures 2.8a, 2.10a, and 2.10b). This general separation of the infiltrating stream water into flow cells pointing in upstream and downstream directions has also been shown in several 2-D studies investigating stream flow over structured streambeds and the effects of ambient groundwater on flow in the HZ [Boano et al., 2008; Cardenas and Wilson, 2007c]. In addition to this general flow separation shown in our 3-D simulations, the lateral in- and exfiltration patterns are also affected by ambient groundwater flow. The variations in the hyporheic flow field result from competing pressure gradients either caused by the H gradients along the streambed or vertical gradients imposed by ambient groundwater flow. For increasing magnitudes of q_{bot}, the hyporheic flow cell first disappears at the stream bank. A plausible explanation for this is that the lower bed form induces a gradient along the smaller bed form amplitude in the vicinity of the stream bank. For strong gaining conditions, the vertical gradient evokes groundwater upwelling in the pool area but also close to the stream bank and thus hampers the formation of a hyporheic flow cell that would span over the entire stream width (Figure 2.8d). Additionally, this high vertical upward directed gradient close to the stream bank induces flow paths in the hyporheic flow cell that have strong lateral components toward the stream bank (Figures 2.8d and 2.10g,h,o,p at $y = 3$ to 4 m).

For the losing case, strong downward vertical gradients (high negative q_{bot}) cause stream water to predominantly downwell at the upstream H_{max} location (Figure 2.8b). Additional downwelling occurs close to the stream bank along the crest area, where the bed form-induced gradient does not exceed the vertical gradient. Here similarly to the gaining case, hyporheic flow cells are truncated close to the stream bank and shifted in downstream direction from the crest (Figures 2.10c,d,k,l). In contrast to the gaining case, the flow paths in the hyporheic flow cells close to the stream bank have a strong lateral flow component toward the stream center, induced by the downward vertical gradient.

For both the losing and the gaining cases higher magnitudes of q_{bot} induce higher vertical gradients and, hence, a stronger lateral shift of the hyporheic flow paths close to the stream bank. Although hyporheic flow paths are strongly altered by q_{bot}, the average lateral flow component expressed as y_{dist} remained relatively unaffected (Figures 2.5 and 2.6g to i). Hyporheic flow paths that deviated from the general downstream direction but rather showed complex patterns of in- and exfiltration in directions lateral and opposed to the direction of stream flow have also been observed in a field study by Angermann et al. [2012]. These patterns could potentially be explained by the interplay between 3-D streambed morphology and ambient groundwater flow.

2.4.3 Effects of Ambient Groundwater Flow and Varying Discharge on the Integral Characteristics of Hyporheic Exchange

Our results show that the integral characteristics of hyporheic exchange Q_{HZ}, $V_{HZ}{}^*$ and MRT are similar between the gaining and losing cases for the same magnitudes of q_{bot} and Re. This relative insensitivity of the magnitudes of Q_{HZ}, $V_{HZ}{}^*$ and MRT to the direction of groundwater flow in our model is in line with the results of Cardenas and Wilson [2007c], who found Q_{HZ}, hyporheic depth, and MRT to be almost equal between the gaining and the losing cases. In contrast to Cardenas and Wilson [2007c], however, Q_{HZ}, $V_{HZ}{}^*$ and MRT in our simulations are not absolutely identical in both cases. Under losing conditions, Q_{HZ} is slightly lower, $V_{HZ}{}^*$ is lower and the MRT are shorter compared to the gaining case. Also the critical $q_{bot}{}^*$ values, where all hyporheic exchange is suppressed, are different for similar magnitudes of $q_{bot}{}^*$. Critical $q_{bot}{}^*$ is up to 50 % smaller under losing conditions, suggesting that smaller vertical gradients between the streambed and the bottom of the groundwater domain are needed to completely inhibit hyporheic flow compared to the gaining case. This can be caused by the different spatial extents of the infiltration areas at the streambed and the separation of hyporheic flow into an up- and a downstream flow cell, when comparing the gaining to the losing case, described in the section above.

Therefore, we conclude that under losing conditions smaller and thus shallower flow cells develop, accompanied with faster hyporheic flows, and respective shorter MRT. Furthermore, in the losing case hyporheic exchange is more sensitive to the magnitude of q_{bot}.

The ratios between hyporheic exchange flow (Q_{HZ}) and stream discharge (Q_{surf}) decrease for increasing Re. Hence, for high stream flows the fraction of total stream flow that becomes hyporheic flow and is in turn exposed to the higher reaction rates in the HZ becomes smaller. This in turn diminishes potential effects on overall stream water concentrations of constituents such as nitrates. The ratios are generally higher for low magnitudes of q_{bot}, indicating a higher fraction of the infiltrated water of Q_{surf} under low ambient groundwater flow. Losing conditions

result in slightly lower Q_{HZ}/Q_{surf} ratios compared to gaining conditions due to the overall lower values of Q_{HZ}. The ratio Q_{HZ}/Q_{surf} is generally low (1×10^5 to 1×10^6 per meter stream length) and agrees with values of hyporheic exchange found in other studies [Battin et al., 2003; Boulton et al., 1998; Saenger et al., 2005].

Our results demonstrate that the connection of the stream to the ambient groundwater system cannot be disregarded when examining hyporheic exchange. Even low vertical gradients (q_{bot}* in Figure 2.6a) between stream and groundwater can significantly alter the hyporheic flow field and diminish hyporheic exchange flow and extent under both losing and gaining conditions.

2.4.4 Threshold of Streambed Amplitude

The influence of streambed amplitude on hyporheic exchange is characterized by a threshold behavior in our simulation. Above a certain threshold in amplitude, Q_{HZ} and MRT become insensitive to further increases in amplitude (see Figure 2.7). Our results generally show that a distinct streambed morphology is necessary to produce sufficient pressure differences at the streambed for advective pumping to occur. If this condition is met, additional effects of the height of the streambed morphology on hyporheic exchange are minor. Tonina and Buffington [2011] showed data from flume experiments with partially submerged pool-riffle sequences of four different amplitudes. In their Figure 5, q* (comparable to our Q_{HZ}) is smallest for the lowest amplitude and practically equal for the three higher amplitudes. Although they did not explicitly describe this relationship, their results are in line with the threshold of bed form amplitude observed in our study. Furthermore, Packman et al. [2004] showed in a flume experiment that exchange flow in structured beds is generally higher than in a flat bed and that higher bed forms only slightly increased hyporheic exchange. Although, the study of Packman et al. [2004] was conducted in 2-D, the lack of a significant increase of hyporheic exchange with increasing bed form height is similar to our results based on 3-D modeling.

Hence, the most important controls of hyporheic exchange in the studied pool-riffle systems are stream discharge, and ambient groundwater flow, while the height of bed form amplitude has minor effects beyond a defined threshold.

2.4.5 Residence Times

Many biogeochemical reactions in the HZ are time dependent and thus directly related to the RT of infiltrated stream water in the HZ [Zarnetske et al., 2011a]. For instance, long RT lead to higher consumption of redoxsensitive compounds (oxygen, nitrate), provided that a sufficient carbon source is available [Brunke and Gonser, 1997; Zarnetske et al., 2011a; Marzadri et al., 2012, 2011, 2013]. Therefore, hyporheic RT is a crucial parameter to evaluate the potential for biogeochemical reactions in the HZ. However, Bardini et al. [2012] showed that the transformation of several redox-sensitive compounds increased with stream velocity because the higher amount of solutes advected into the HZ was more important than the overall decrease in residence time. Our RT calculations show that with increasing Re, MRT becomes shorter due to faster flow velocities in the HZ, accompanied with higher Q_{HZ} and vice versa, also in agreement with the findings of Tonina and Buffington [2011]. Hence, low hyporheic flows (small Q_{HZ}) cause longer exposure times to the hyporheic sediments and hence a higher potential for certain biogeochemical reactions to occur.

Furthermore, the flow over less-pronounced streambed morphologies (e.g. A01) produces lower H gradients that result in low Q_{HZ} but high MRT. The effect of longer RT for shallow morphologies is in agreement with the findings of Marzadri et al. [2010], where flows over shallow bed form amplitudes resulted in longer mean RT. However, when comparing our RT data and streambed configuration to those of Figure 8a in Marzadri et al. [2010], our data do not fit to the proposed relationship, because normalized mean RT are too low, compared to the normalized streambed amplitude.

The RT for all our scenarios are well represented by a log-normal distribution. This agrees with several previous studies that have examined hyporheic RT induced by flow over dune-shaped bed forms [Cardenas et al., 2004], submerged pool-riffle structures [Marzadri et al., 2010], and partially submerged pool-riffle sequences [Tonina and Buffington, 2011]. If we were to include the full complexity of a field site, where morphological features at nested scales and sediment heterogeneity occur, our RTD would likely show more tailing. However, the MRT would likely not change very much. Interestingly, the RT in our model cover the range of RT over which Zarnetske et al. [2011a] observed a biogeochemical regime shift in a streambed of similar texture from net nitrifying to net denitrifying. Hence, our results demonstrate that pool-riffle sequences can cause RT that might facilitate biogeochemical regime shifts in the hyporheic sediments.

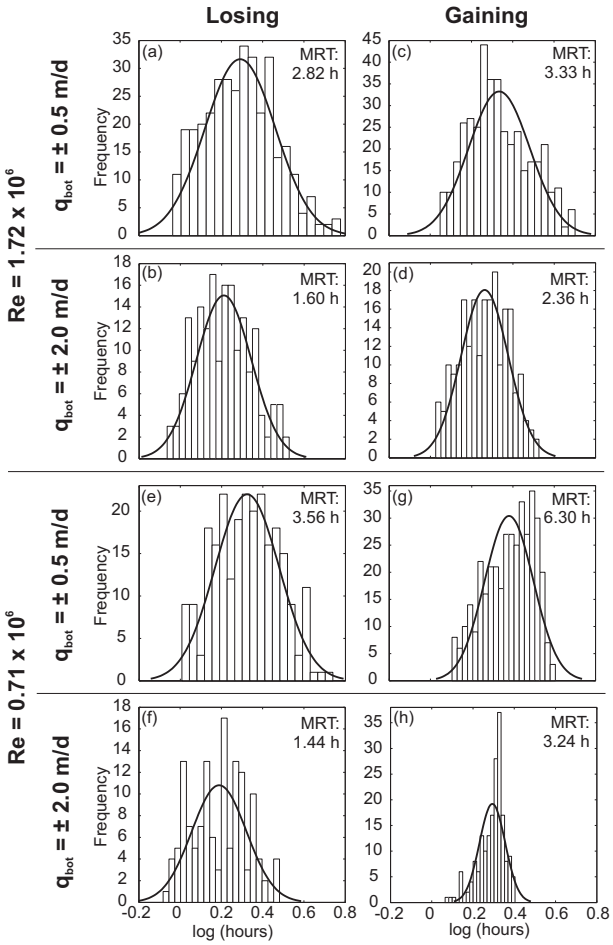

Figure 2.11: Histograms of the residence time distributions (RTD) and median residence times (MRT) of the scenarios in Figure 2.10.

2.5 Summary and Conclusions

In this 3-D modeling study the effects of stream discharge, streambed morphology, and ambient groundwater flow on hyporheic flow in pool-riffle streams were systematically investigated. We combined two-phase CFD simulations of turbulent stream flow over 3-D pool-riffle streambeds with flow modeling in the underlying porous streambed (HZ) for different stream discharges and streambed morphologies. Ambient groundwater flow was represented by either gaining (upward flow of groundwater into the streambed) or losing (downward flow of stream water into the aquifer) conditions. 3-D flow paths in the HZ and hyporheic RTD were derived from particle tracking.

Our CFD simulations showed the formation of 3-D eddies and complex water surfaces including undular hydraulic jumps at the downstream side of riffles (for Fr between 1 and 1.2) resulting

in distinct pressure variations across the streambed surface. If a trough of the standing wave in the undular hydraulic jump coincided with the high pressure in the reattachment zone of the eddy, streambed pressure was locally reduced affecting the developing hyporheic flow cell. Due to the three-dimensional nature of the bed forms, the H_{min} at the downstream side of the riffles was shifted toward the stream bank relative to the location of H_{max} at the upstream side. This separation effect induced significant lateral flow components in the HZ. Additionally, a constricted zone of lower H in the upstream pool region caused secondary hyporheic flow cells in the upstream direction with a slight shift toward the stream center. Lateral flow components in the major hyporheic flow cell were also affected by the direction of ambient groundwater flow and showed a shift toward the stream bank for the gaining case and a shift toward the stream center for the losing case.

Our results highlight the importance of ambient groundwater flow for HZ extent and the characteristics of the 3-D hyporheic flow field in pool-riffle streams, both under gaining and losing conditions. The extent of the hyporheic water volume within the aquifer ($V_{HZ}{}^*$) strongly decreased with increasing magnitude of groundwater flow accompanied with a lower hyporheic exchange flow rate and shorter RT. Neglecting the vertical hydraulic gradients induced by typical rates of ambient groundwater flow would lead to a significant overestimation of the hyporheic exchange flow.

Total hyporheic exchange flow (Q_{HZ}) increased with stream discharge while MRT decreased, due to faster hyporheic flow, despite longer flow paths, as also shown by Tonina and Buffington [2011]. The ratio between hyporheic exchange flow and stream discharge (Q_{HZ}/Q_{surf}) was on the order of 1×10^5 to 1×10^6 per meter stream length and decreased with increasing stream discharge. However, for the relationship between Q_{HZ} and pool-riffle amplitude, we found a threshold in the pool-riffle height, beyond which Q_{HZ} remained constant for even higher pool-riffle amplitudes. This threshold is also observed in the results of the flume study of Tonina and Buffington [2011] and comparable to the findings of the 2-D study of Packman et al. [2004].

Hyporheic RT showed unimodal log-normal distributions and MRT ranged from 0.7 to 19 h over the series of investigated scenarios. Over a similar range of MRT, shifts from a net nitrifying to a net denitrifying biogeochemical regime have been observed in comparable field settings [Tonina and Buffington, 2011]. This suggests that the streambeds investigated in this study may have the potential to attenuate redox-sensitive solutes.

Our results elucidated distinct 3-D patterns and dynamics of hyporheic exchange in pool-riffle streams, and for the first time, highlighted how ambient groundwater flow affects these hyporheic flow characteristics. These dynamics will likely affect the biogeochemical turnover of solutes in pool-riffle streams and their impact should be addressed in future work.

3 | Hyporheic transport and biogeochemical reactions in pool-riffle systems under varying ambient groundwater flow conditions

This chapter is published as:
Trauth, N., C. Schmidt, M. Vieweg, U. Maier, and J.H. Fleckenstein (2014), Hyporheic transport and biogeochemical reactions in pool-riffle systems under varying ambient groundwater flow conditions, *Journal of Geophysical Research: Biogeosciences*, 119(5): 910–928, doi:10.1002/2013JG002586.

Abstract

At the interface between stream water, groundwater, and the hyporheic zone (HZ), important biogeochemical processes that play a crucial role in fluvial ecology occur. Solutes that infiltrate into the HZ can react with each other and possibly also with upwelling solutes from the groundwater. In this study, we systematically evaluate how variations of gaining and losing conditions, stream discharge, and pool-riffle morphology affect aerobic respiration (AR) and denitrification (DN) in the HZ. For this purpose, a computational fluid dynamics model of stream water flow is coupled to a reactive transport model. Scenarios of variations of the solute concentration in the upwelling groundwater were conducted. Our results show that solute influx, residence time, and the size of reactive zones strongly depend on presence, magnitude, and direction of ambient groundwater flow. High magnitudes of ambient groundwater flow lower AR efficiency by up to 4 times and DN by up to 3 orders of magnitude, compared to neutral conditions. The influence of stream discharge and morphology on the efficiency of AR and DN are minor, in comparison to that of ambient groundwater flow. Different scenarios of oxygen (O_2) and nitrate (NO_3) concentrations in the upwelling groundwater reveal that DN efficiency of the HZ is highest under low upwelling magnitudes accompanied with low concentrations of O_2 and NO_3. Our results demonstrate how ambient groundwater flow influences solute transport, AR, and DN in the HZ. Neglecting groundwater flow in stream-groundwater interactions would lead to a significant overestimation of the efficiency of biogeochemical reactions in fluvial systems.

3.1 Introduction

The hyporheic zone (HZ), where stream water interacts with the streambed sediment, has been recognized as a biogeochemically active zone that plays a crucial role in fluvial ecosystems [Findlay, 1995; Brunke and Gonser, 1997; Battin et al., 2003]. Oxygen (O_2), dissolved organic carbon (DOC), nutrients, contaminants, and other solutes can be transported by infiltrating

stream water into the streambed sediments where they mix with groundwater-borne solutes from the connected aquifer system [Findlay, 1995; Boulton et al., 1998]. Depending on their concentration and residence time in the hyporheic sediment, the solutes can react with each other according to redox reactions. Important reactions in the HZ are the decomposition of organic carbon by consumption of O_2 and nitrogen (N) by aerobic and anaerobic microbial communities [Findlay, 1995; Bencala, 2000].

The permanent removal of N species from the aquatic system is primarily related to denitrification, which transforms NO_3 to N_2 gas [Birgand et al., 2007]. Elevated N loads in streams, commonly associated with anthropogenic activities, has been clearly linked to eutrophication of streams, lakes, and marine ecosystems [Seitzinger et al., 2002; Mulholland et al., 2008], thus, the potential of a fluvial system to degrade N has been the focus of much research [Harvey and Bencala, 1993; Hill et al., 1998; Kasahara and Hill, 2006; Pinay et al., 2009; Zarnetske et al., 2011a, 2012; Lansdown et al., 2012; Krause et al., 2013]. However, although the HZ acts primarily as a sink for N within NO_3-rich streams, in systems with low NO_3 concentrations, nitrification, not denitrification, is often the dominant process and acts as a NO_3 source [Jones and Holmes, 1996; Dahm et al., 1998]. Morphological features such as dunes, ripples, and pool-riffle sequences can drive increased surface-subsurface water exchange thereby enhancing the biogeochemical transformation of solutes within streams [Kasahara and Hill, 2006; Lautz and Fanelli, 2008; Maazouzi et al., 2013]. This morphological effect is particularly pronounced in pool-riffle sequences [Harvey and Bencala, 1993; Storey et al., 2003; Lansdown et al., 2012].

Field studies, flume experiments [Thibodeaux and Boyle, 1987; Packman et al., 2004; Kessler et al., 2012; Fox et al., 2014], and column experiments with hyporheic sediment [Doussan et al., 1997; Gu et al., 2007] have all been useful in improving our understanding in solute transport and biogeochemical turnover processes in the HZ. Furthermore, numerical simulations, such as reactive transport models, can be an important tool to support these field studies and laboratory experiments [Fleckenstein et al., 2010; Frei et al., 2012], by providing detailed understanding of the controlling mechanisms and spatial distribution of reactions within the HZ. With respect to the interactions between morphology and HZ processing, numerical simulations have been used to simulate biogeochemical reactions in marine ripples [Cardenas et al., 2008] and to evaluate how varying streamflow over 2-D dunes affects turnover processes of redox-sensitive compounds in the HZ [Bardini et al., 2012]. When coupled with laboratory flume experiments, numerical simulations have demonstrated the functioning of aerobic respiration and denitrification in streambed sediments [Kessler et al., 2012] and the impact of 3-D pool-riffle morphology on nitrogen dynamics in streambed sediments [Marzadri et al., 2011]. What has not been considered in most studies is the impact of ambient groundwater flow (either upwelling or downwelling) on solute transformation in the HZ, even though this flow can have a significant impact on hyporheic flux and residence times [Cardenas and Wilson, 2007c; Boano et al., 2009; Hester et al., 2013; Trauth et al., 2013] and consequently also on whole-stream biogeochemistry [Odum, 1956; McCutchan et al., 2002; Krause et al., 2013]. Disregarding upwelling groundwater leads to overestimation of the metabolic potential of the HZ [Hall and Tank, 2005; Hill et al., 1998].

In this study, we investigate the following: (1) the spatial distribution of biogeochemical reactions in the HZ of 3-D pool-riffle systems under various hydraulic conditions, (i.e., stream discharge and ambient groundwater flow) and two different morphologies, (2) the effect of upwelling groundwater

with varying O_2 and NO_3 concentrations on biogeochemical reactions in the HZ, and (3) the potential of aerobic respiration and denitrification in the hyporheic zone of pool-riffle systems. The hydraulic simulations are based on the surface-subsurface coupling approach of Trauth et al. [2013]. A computational fluid dynamics code (CFD) was used to simulate turbulent streamflow over 3-D pool-riffle morphologies and was sequentially coupled to a groundwater flow model via the resulting hydraulic head distribution at the streambed surface. At the bottom of the model domain, upwelling or downwelling fluxes were assigned, representing losing or gaining conditions. In this study, we consider the stream and hyporheic flow scenarios of Trauth et al. [2013] and add a reactive transport model in order to simulate solute transport and biogeochemical reactions. In addition, the solute concentration of O_2 and NO_3 of the upwelling groundwater is varied, accounting for different chemical conditions of the ambient groundwater.

3.2 Methodology

3.2.1 Simulation of Turbulent Stream Water Flow Over Pool-Riffle Sequences

The streambed morphology used in this study is inspired by real pool-riffle sequences, observable at the Selke river in north central Germany [Schmidt et al., 2012]. The main features of the pool-riffle morphology are approximated by the following equation [Trauth et al., 2013]:

$$Z(x,y) = A\ sin\left(\frac{2\pi}{\lambda}x\right)\ cos\left(\frac{\pi}{w}y\right) \tag{3.1}$$

where x and y are the longitudinal (parallel to streamflow) and lateral (perpendicular to streamflow) planar coordinates, respectively, A is the maximum amplitude of the pool-riffle sequence at the center of the stream, λ is the longitudinal wavelength of the pool-riffle sequence, and w is the stream width. Using this approximation, the maximum excursions in streambed elevation are located in the stream center ($w = 0$; Figure 3.1) and streambed elevations converge laterally to a constant elevation at the stream bank. We apply equation 3.1 to two different pool-riffle amplitudes, $A = 0.1$ and 0.5 m, hereafter referred to as A01 and A05, respectively.
Streamflow over complex streambed morphologies, and the resulting hydraulic pressure at the streambed surface, can be accurately modeled using CFD, solving the full Navier-Stokes equations [Cardenas and Wilson, 2007a; Tonina and Buffington, 2009b; Janssen et al., 2012; Kessler et al., 2012]. In this study we use threedimensional CFD simulations with a free surface realized by a two-phase model using the volume of fluid [Hirt and Nichols, 1981] method to represent turbulent streamflow over submerged pool-riffle sequences. Turbulence closure is represented by Large Eddy Simulation with the original Smagorinsky subgrid scale model [Smagorinsky, 1963].
The open-source CFD package OpenFOAM was used for these turbulent flow simulations. Further details on the model code, the boundary conditions, and the mesh geometry are provided in Trauth et al. [2013] and in the OpenFOAM documentation (`www.openfoam.org`). To avoid boundary effects, the CFD model domain contains a sequence of five pool-riffle sections of which only the inner three are used in the groundwater model. To avoid boundary effects in the groundwater model, only the middle pool-riffle sequence of the porous domain is evaluated (x = 10 to 20 m in Figure 3.1). Stream discharge (Q_{surf}), represented by the volumetric flux of water entering the surface water model domain, is specified by defining water level and velocity. Low- and high discharge scenarios are considered, based on the CFD simulations of Trauth et al.

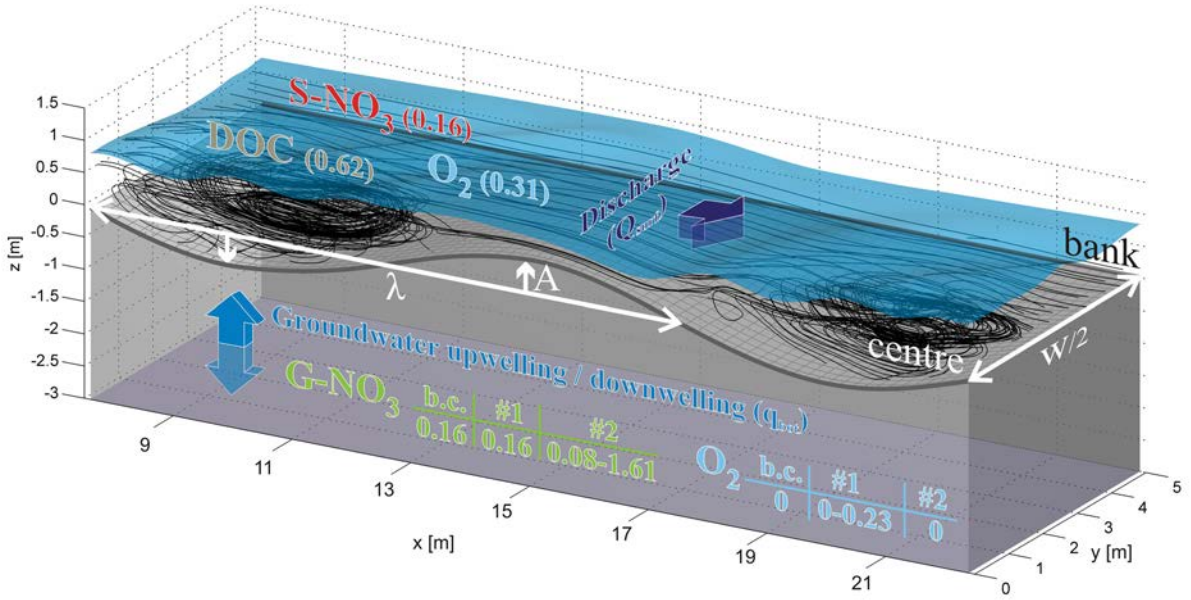

Figure 3.1: Model setup for reactive transport simulations for the three reactive transport scenarios (base case and scenarios #1 and #2), corresponding to Table 3.2. Concentrations in brackets are in mmol/L. Eddies and streamlines are represented by black lines above streambed.

[2013] (for A05: 7.40 and 14.78 m^3/s and for A01: 7.46 and 14.93 m^3/s. In these simulations, distinct eddies develop in three dimensions (streamlines in Figure 3.1), responsible for a complex hydraulic head distribution at the streambed surface. The maxima of the simulated hydraulic heads correspond to the reattachment points of the eddies at the upstream side of the riffle (approximately $x = 13$ m; Figure 3.1), whereas the minimum heads at the downstream side of the riffle correspond to the point where the next eddy detaches (approximately $x = 18$ m; Figure 3.1). As a result of this hydraulic head distribution, stream water generally infiltrates the subsurface at the upstream side of the riffle and reenters the stream at the downstream side. For simulating this subsurface flow field the hydraulic head distribution at the streambed surface is used as upper boundary condition for the groundwater model which is described in the following section.

3.2.2 Subsurface Flow Model

The groundwater model MIN3P was used for simulating flow and reactive transport in the hyporheic zone. MIN3P is a finite volume code that solves Richard's equation for variably saturated flow [Mayer et al., 2002]. In our simulations the model domain is fully saturated and the governing equations for incompressible, steady state groundwater flow are as follows:

$$\nabla \cdot \boldsymbol{q} = 0 \tag{3.2}$$

$$\boldsymbol{q} = -K \nabla H \tag{3.3}$$

where $\boldsymbol{q}$ is the Darcy flux, K is the hydraulic conductivity, and ∇H is the gradient of the hydraulic head.

At the bottom of the groundwater model domain, at 3 m depth below the baseline of the

sinusoidal streambed elevation, a Neumann boundary is assigned to control the inflow or outflow of water (q_{bot}). In our scenarios q_{bot} values of -2.5 to $2.5\,\mathrm{m/d}$ are considered, ranging from losing (-) to neutral (0) to gaining conditions (+). Concentrations of solutes at the top and the bottom of the model domain were assigned as Cauchy type boundary conditions, ignoring dispersive solute flux. Boundary conditions at the upstream, the downstream, and the lateral sides of the model domain are defined by no-flow boundaries. Using a no-flow boundary at the lateral sides of the model domain disregards potential lateral exchange between the hyporheic zone and the riparian area. Head measurements in the streambed and the stream banks revealed very small lateral gradients compared to strong vertical gradients at our field site, corroborating the results from a similar site [Engelhardt et al., 2011]. The simplifying model assumption is thus supported by the observation that water flux to the stream is dominated by fluxes across the streambed. Hydraulic conductivity, measured in the streambed sediments of the field site using slug tests, is isotropic with a value of 5×10^{-4} m/s.

The general flow field in the groundwater model is characterized by flow paths that infiltrate the subsurface domain upstream of a riffle and exfiltrate back to the stream downstream of a riffle [Trauth et al., 2013]. Hence, these flow paths form the major hyporheic flow cell (HFC). Additionally, a second and minor flow cell develops, which is opposed to the streamflow direction, and where hyporheic water is exfiltrating near the upstream pool [Trauth et al., 2013]. With increasing magnitude of water flow through the bottom model boundary q_{bot}, under both losing and gaining conditions, hyporheic exchange flow (Q_{HZ}) and median residence times (MRT) decrease within the HFC. Based on these hyporheic flow fields described in detail by Trauth et al. [2013], reactive transport simulations were conducted.

3.2.3 Reactive Transport Model

In MIN3P, reactive transport for steady state reactions is implemented as

$$R_s = \nabla \left(\frac{\boldsymbol{q}}{n} C_s - \boldsymbol{D} \nabla C_s \right) \tag{3.4}$$

where R_s is the kinetic rate (source/sink terms) of the solute species s, C_s is the concentration of that species, n is the sediment porosity ($n = 0.3$), and $\boldsymbol{D}$ is the hydrodynamic dispersion tensor. The dispersivity coefficients are constant for all scenarios and are equal to 0.1 m, 0.01 m, and 0.001 m for longitudinal dispersivity, transversal horizontal dispersivity, and transversal vertical dispersivity, respectively. In our numerical experiments we simulated the biogeochemical processes of aerobic respiration (AR) and denitrification (DN) of dissolved organic matter according to the following reaction equations:

Aerobic respiration:

$$CH_2O + O_2 \rightarrow CO_2 + H_2O \tag{3.5}$$

Denitrification:

$$5CH_2O + 4NO_3^- + 4H^+ \rightarrow 5CO_2 + 2N_2 + 7H_2O \tag{3.6}$$

The reactions are simulated using a Monod-type formulation, considering electron donors (CH_2O used as DOC), acceptors (O_2, NO_3), and inhibition terms. The general Monod kinetic is in the form of

$$R = \mu_{max} I \left(\frac{C_D}{K_D + C_D} \right) \left(\frac{C_A}{K_A + C_A} \right) \tag{3.7}$$

where R is the reaction rate, μ_{max} represents the maximum reaction rate, C_D and C_A are the concentrations of the electron donors and acceptors, and K_D and K_A are the half-saturation constants for electron donors and acceptors, respectively. The reaction rate of DN is inhibited in the presence of O_2, because O_2 is the primary electron acceptor for organic matter oxidation by microbial communities [Stumm and Morgan, 2012; Hedin et al., 1998]. Therefore, an inhibition factor I is required for simulation of the denitrification kinetic, as described by

$$I = \left(\frac{K_I}{K_I + C_{O_2}} \right) \tag{3.8}$$

where K_I is the inhibition constant and C_{O_2} is the O_2 concentration.
The maximum reaction rate of AR used in the model ($\mu_{max,AR} = 0.478\,\text{mmol/L/d} = 15.3\,\text{mg/L/d}$) is calculated from combined measurements of electrical conductivity (EC) and dissolved oxygen (DO) concentrations at an in-stream gravel bar at the Selke river [Schmidt et al., 2012] during the summer months. Time series of EC and DO concentrations in the stream water and in the streambed were measured at 0.45 m depth at the upstream and downstream end of the gravel bar. A cross-correlation method was used to calculate the travel time between the stream water EC sensor and the EC measured in the sediment. The difference between the DO concentration in the stream water time series and the DO concentration in the sediment time series shifted by the corresponding travel time was calculated. This difference is assumed to be the DO consumed by aerobic respiration, and dividing it by the time lag leads to a zero order DO decay rate. Since the decay rate is temperature dependent a time-averaged value was used as model input. This rate is considered as the maximum aerobic respiration rate $\mu_{max,AR}$, assuming saturated DO conditions and an unlimited DOC source in the stream water under relatively warm conditions. The value of $\mu_{max,AR}$ is at the lower end of the range of observed O_2 consumption rates in the flume studies of Precht et al. [2004]. The maximum reaction rate of DN ($\mu_{max,DN}$) used in the model is based on values from the literature [García-Ruiz et al., 1998; Gu et al., 2007] as the direct measurement of NO_3 time series is too complicated. The half saturation constants K_{O_2}, K_{NO_3}, K_{DOC} and the O_2 concentration inhibiting DN (K_I) are also based on literature values from studies working with streambed sediments [Zarnetske et al., 2011a; Gu et al., 2007]. Simulations are conducted under constant temperature of 15 °C, representing average stream water temperature at the field site during the summer months. The model parameters for the reactions are listed in Table 3.1.

Table 3.1: Input Parameters for Reactive Transport Model Code MIN3P

Parameter	Value
K_{O_2}	6.25×10^{-3} mmol/L
K_{NO_3}	3.23×10^{-2} mmol/L
K_{DOC}	1.07×10^{-1} mmol/L
K_I	3.13×10^{-2} O_2 mmol/L
$\mu_{max,AR}$	4.78×10^{-1} mmol/L
$\mu_{max,DN}$	8.64×10^{-2} mmol/L

3.2.4 Reactive Transport Scenarios

Three different scenarios (base case, #1, and #2) are simulated in order to evaluate the impact of hydraulic conditions and groundwater O_2 and NO_3 concentrations on reaction rates in the HZ (Table 3.2 and Figure 3.1).

The stream water at the field site can be considered to be saturated in O_2 [Vieweg et al., 2013], which is common for well-mixed surface water bodies [Battin et al., 2003; Diem et al., 2013]. Hence, a constant O_2 concentration of 0.31 mmol/L (10 mg/L) was assigned to the top of the groundwater model domain. Time series of dissolved organic carbon (DOC) at a stream gauging station 5 km upstream of the field site show varying DOC concentrations between 10 and 30 mg/L during the summer month. Hence, a constant CH_2O concentration of 0.62 mmol/L (18.66 mg/L) is assigned to the top of the groundwater model, representing a DOC source equal to twice that of the molar O_2 concentration. By doing so we implicitly assume that DOC does not limit reactivity in the streambed sediments [Hill et al., 1998; Storey et al., 2003; Marzadri et al., 2011; Peyrard et al., 2011; Diem et al., 2013], an assumption that is necessary to avoid complete consumption by AR and ensure that there is a DOC source available for DN. Preliminary simulation runs using upper boundary (i.e., stream water) DOC concentration equal to the molar concentration of O_2 resulted in complete DOC consumption within the HZ by AR and extremely low NO_3 consumption rates, confirming that extensive DN is not possible under DOC limitation [Jones et al., 1995; Hedin et al., 1998; Baker et al., 2000; Zarnetske et al., 2011a]. In contrast, in all three model scenarios the DOC source CH_2O concentration is set to zero in the groundwater reflecting the fact that the concentrations of DOC available for respiration processes in groundwater are commonly low compared to stream water [Kaplan and Bott, 1982; Appelo and Postma, 2005].

NO_3 concentrations in both stream water and groundwater can vary temporally and spatially, depending on, e.g., soil properties, precipitation rates, and seasonal land use in the stream catchment [Mulholland et al., 2008; Bartsch et al., 2013]. As previous studies have demonstrated, in the hyporheic zone upwelling groundwater can mix with infiltrating stream water [Cardenas and Wilson, 2007c; Trauth et al., 2013; Hester et al., 2013] and with that NO_3 from both sources. In order to track the relative spatial distribution of groundwater- versus stream water-sourced NO_3 within the HZ, and to distinguish the relative consumption of NO_3 from these two sources, we "virtually label" NO_3 within our simulations as derived from either stream water (S-NO_3) or groundwater (G-NO_3). The chemical reactions and Monod kinetics for both NO_3 species are similar and can react with the same DOC species. The resulting denitrification of these two NO_3 sources is likewise distinguished as S-DN and G-DN.

The base case represents a quasi-pristine fluvial system, with moderate NO_3 concentrations in both the stream water and the groundwater. O_2 can only enter the HZ by infiltration of stream water, and O_2 concentrations in the groundwater are zero. In this scenario the influence of high and low stream discharge, as well as losing and gaining conditions on reactions in the HZ is evaluated. In scenario #1, runs of different O_2 concentrations in the upwelling groundwater (0 to 0.234 mmol/L = 0 to 7.5 mg/L) are performed in order to evaluate the impact of groundwater O_2 concentrations on the reactions in the HZ. Finally, in scenario #2 we evaluate the influence of different concentrations of upwelling NO_3 on biogeochemical reactions in the HZ by varying the G-NO_3 concentration between 0.08 to 1.61 mmol/L (5 to 100 mg/L NO_3) while keeping the

Table 3.2: Hydraulic and Chemical Boundary Conditions of Reactive Transport Scenarios

	Hydraulic Boundary Conditions		Chemical Boundary Conditions					
	Stream Discharge	Ambient Groundwater Flow	Stream Water/Streambed Boundary			Groundwater/Bottom Boundary		
	Q_{surf} [m^3/s]	q_{bot} Darcy Velocity [m/d]	O_2 [mmol/L]	DOC (CH_2O) [mmol/L]	S-NO_3 (Stream Water Nitrate) [mmol/L]	O_2 [mmol/L]	DOC (CH_2O) [mmol/L]	G-NO_3 (Ground Water Nitrate) [mmol/L]
Base case	7.40 and 14.78 (A05) 7.46 and 14.93 (A01)	-2.5 to +2.5	0.31	0.62	0.16	0.0	0.0	0.16
Scenario #1	7.40 (A05) 7.46 (A01)	+0.125 to +2.5	0.31	0.62	0.16	0.0 to 0.23	0.0	0.16
Scenario #2	7.40 (A05) 7.46 (A01)	+0.125 to +2.5	0.31	0.62	0.16	0.0	0.0	0.08 to 0.61

concentration of S-NO_3 at the top of the groundwater model constant.
During all simulations the initial concentrations of the reacting species (O_2, DOC, G-NO_3, and S-NO_3) are set to zero in the entire modeling domain. Steady state chemical equilibrium, when outflux and consumption rates become constant, is reached after approximately 150 h of simulation time.
Nitrification is not considered in our scenarios, as our model design is based on a stream system with very low ammonium (NH_4) loadings ($< 5.5 \times 10^{-3}$ mmol/L) and no wastewater treatment inputs, and relatively high S-NO_3 concentrations (up to 0.161 mmol/L). In support of this assumption, we conducted several preliminary runs where nitrification was considered with an ammonium concentration of 5.5×10^{-3} mmol/L. Results from these runs indicated that less than 1.5 % of the total nitrate input (S-NO_3+G-NO_3) was a product of nitrification. Hence, we assume that neglecting nitrification in our subsequent detailed simulations is justified. Our assumption is further corroborated by Kessler et al. [2012], who could show that more than 90 % of the NO_3 depleted by DN in the HZ originated from stream water and not from nitrification. Peyrard et al. [2011] and Marzadri et al. [2012] also demonstrated that in a NO_3-rich stream, nitrification is of minor importance.

3.3 Results

In the following section, the description and analysis of our modeling results are based on three metrics provided by the output of the numerical model:

1. The mass flux of solutes into the modeling domain, from the stream (O_2, DOC, and S-NO_3) and groundwater (G-NO_3), normalized to streambed area in mmol/d/m^2.

2. The mass flux of solute consumed by aerobic respiration (AR), denitrification of stream water-borne nitrate (S-DN), and denitrification of groundwater-borne nitrate (G-DN) under quasi steady state conditions, normalized to streambed area in mmol/d/m^2.

3. The fraction of consumed O_2, S-NO_3, and G-NO_3 relative to the influx from the stream and/or groundwater, denoted as F_{O2}, $F_{S\text{-}NO3}$, and $F_{G\text{-}NO3}$.

To distinguish highly reactive zones from less reactive zones in the modeling domain, a threshold of 20 % of the maximum reaction rate (μ_{max}) of the respective solute is defined. Zones of high reactivity exceed this threshold.

3.3.1 Influence of Ambient Groundwater Flow on Transport and Reactions (Base Case)

3.3.1.1 Neutral Conditions (q_{bot}=0)

Under neutral groundwater flow conditions ($q_{bot} = 0$), the only source of solutes in the HZ is from the stream water and no solutes are introduced across the bottom boundary (Figure 3.2a and 3.2d). Under neutral conditions the HFCs are at their maximum extent, reaching the bottom of the model domain. Within the shallow HFC, aerobic conditions prevail and O_2 concentration decreases with depth due to O_2 consumption (Figure 3.3a and 3.4b). Large volumes in the deeper HZ are characterized by anaerobic conditions as the result of O_2 consumption along the flow

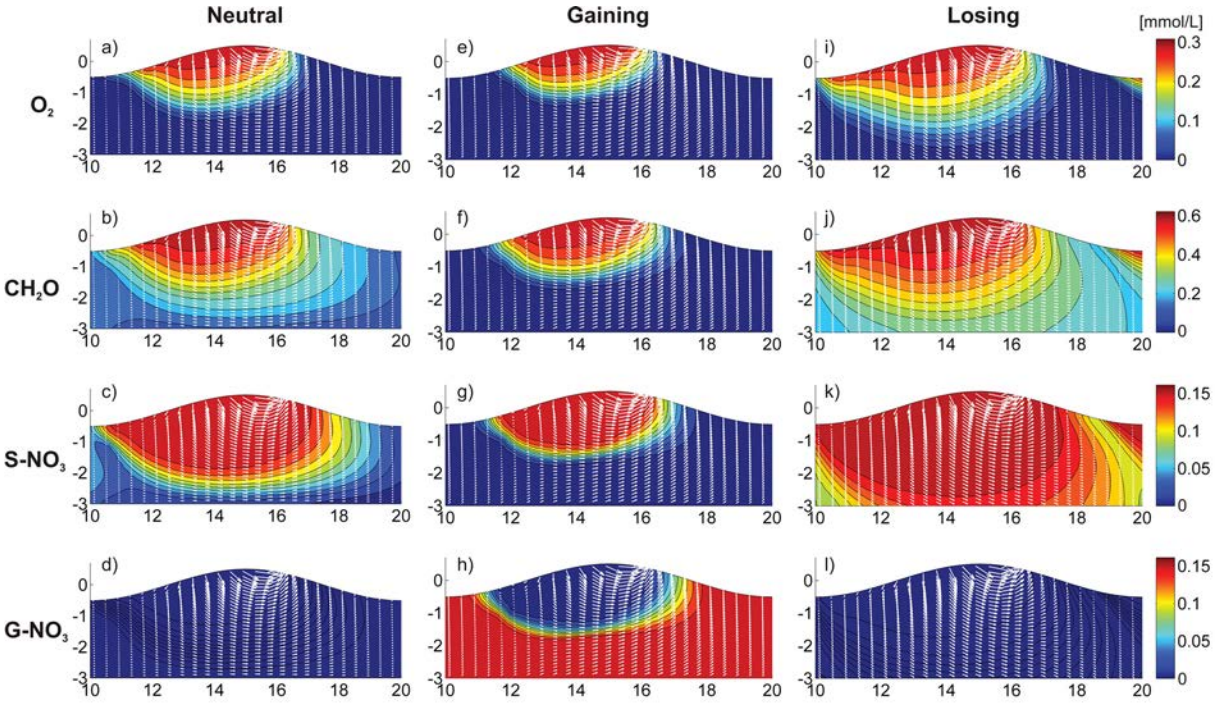

Figure 3.2: Cross sections of solute concentration along the x-z plane at location y = 0.4 m under (left) neutral (q_{bot} = 0 m/d), (middle) gaining (q_{bot} = +0.5 m/d), and (right) losing conditions (q_{bot} = −0.5 m/d). The vectors depict the direction of the hyporheic flow and denote the formation of hyporheic flow cells (HFC). Streamflow direction is from left to right. Simulated using the base case scenario with low stream discharge Q_{surf} = 7.4 m^3/s.

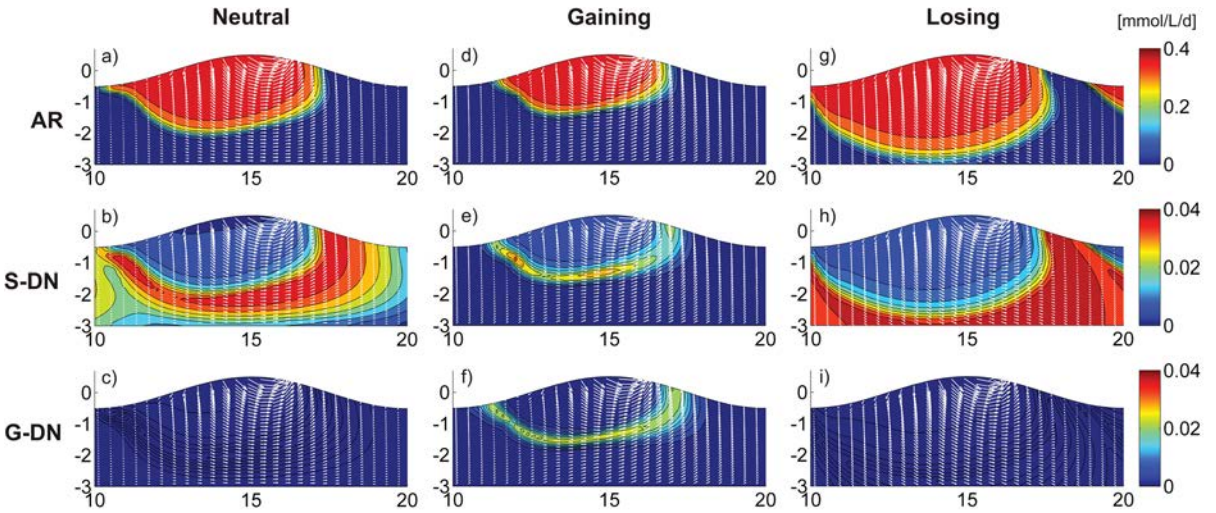

Figure 3.3: Cross sections of solute consumption rates along the x-z plane at location y = 0.4 m under (left) neutral (q_{bot} = 0 m/d), (middle) gaining (q_{bot} = +0.5 m/d), and (right) losing conditions (q_{bot} = −0.5 m/d). The vectors depict the direction of the hyporheic flow. Streamflow direction is from left to right. Simulated using the base case scenario with low stream discharge Q_{surf} = 7.4 m^3/s.

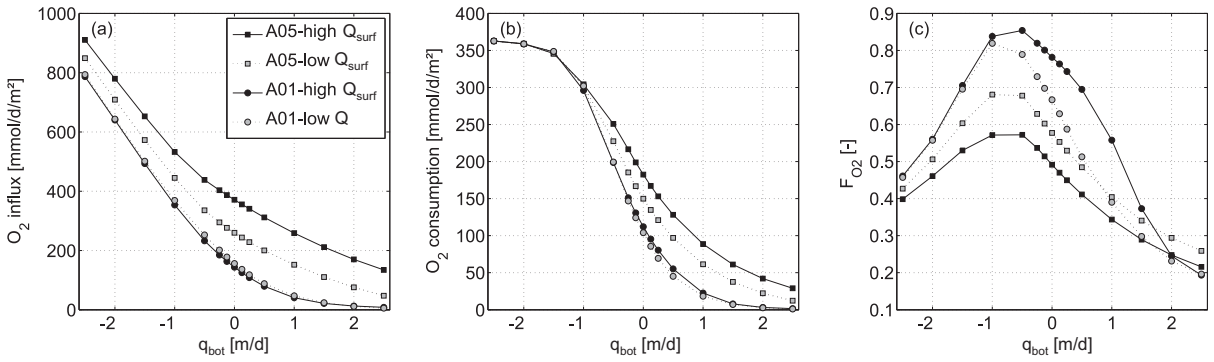

Figure 3.4: Oxygen influx, consumption, and fraction consumed under varying ambient groundwater flow directions and magnitudes (q_{bot}), stream discharge (Q_{surf}), and morphology for the base case scenario. (a) O_2 influx across the streambed, (b) O_2 consumption, and (c) O_2 consumption as a fraction of the total O_2 flux (F_{O2}).

path through the HZ. The size of these anaerobic zones within the streambed is a function of the residence time and the consumption of the inflowing O_2 in the HZ. Denitrification of S-NO_3 occurs within the anaerobic zones (Figure 3.3b) and the highest fraction of S-NO_3 consumption ($F_{S\text{-}NO3} = 0.27$) is observed during neutral conditions when these zones reach their maximum extent (Figure 3.5b and 3.5d). In the lateral direction (toward the stream bank and perpendicular to the direction of streamflow), aerobic and anaerobic conditions do not change significantly and reaction rates are uniform.

3.3.1.2 Gaining Conditions (q_{bot}>0)

Under gaining conditions the aerobic zone is constrained to the upper part of the HZ, where the two HFCs (major and minor) dominate the flow field. As the magnitude of groundwater upwelling increases, the velocity of stream water infiltrating the HZ and the size of the HFCs decrease [Trauth et al., 2013]. Accordingly, O_2, DOC, and S-NO_3 fluxes across the streambed are reduced as a function of both the diminished infiltration areas and the lower infiltration velocities (Figure 3.4a and 3.5a). In addition, both the residence time of the solutes in the HFC and the zone available for AR are reduced with increased q_{bot} as a result of the shorter flow paths and the diminished size of the HFC (Figures 3.6a and 3.7, top), respectively. These changes result in reduced potential of AR, represented by F_{O2}, with increasing q_{bot}, because O_2 consumption decreases faster relatively to the O_2 influx (Figure 3.4c). The extent and depth of the aerobic zone decreases toward the stream bank and is completely suppressed under high magnitudes of gaining q_{bot} (Figure 3.7, top).

Except for the aerobic zone within the HFC, the majority of the modeling domain is anaerobic (blue areas in Figure 3.2e). Beneath the aerobic zone where O_2 is extensively consumed by AR, and DOC from the stream source still exists, conditions for DN are met. S-NO_3 and upwelling G-NO_3 mix with DOC and react in a "reactive fringe" surrounding the aerobic zone. The reactive fringe is clearly visible in Figures 3.3e and 3.3f, where green to red colors indicate highly reactive areas and also in Figures 3.7 (middle) and 3.7 (bottom), where it is represented by the volume that is enclosed by the isosurfaces of 20 % of μ_{max}. Minor S-DN also occurs above this reactive fringe in the aerobic zone. Here, DN reaction rates are strongly inhibited by the presence of O_2 and hence, represent an insignificant contribution to the total S-DN.

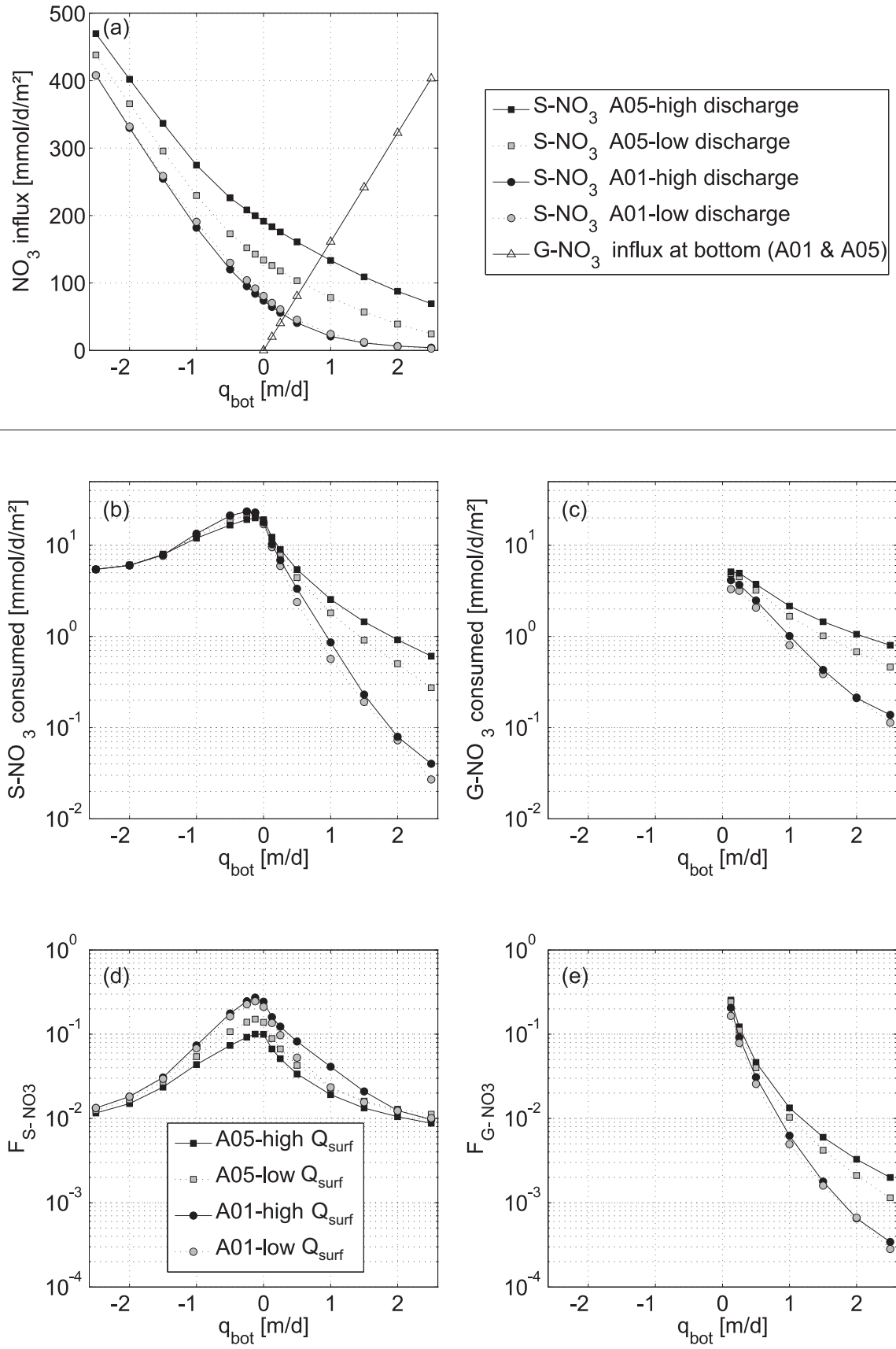

Figure 3.5: NO_3 influx, consumption, and fraction consumed under varying ambient groundwater flow directions and magnitudes (q_{bot}), stream discharge (Q_{surf}), and morphology for the base case scenario. (a) NO_3 influx, (b) S-NO_3 consumption rates, (c) G-NO_3 consumption rates, (d) S-NO_3 consumption as a fraction of influx ($F_{S\text{-}NO3}$), and (e) G-NO_3 consumption as a fraction of influx ($F_{G\text{-}NO3}$).

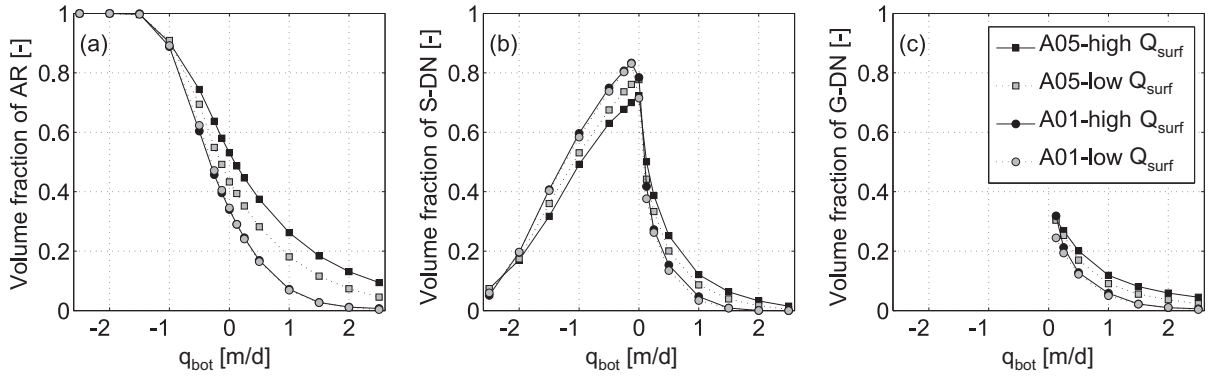

Figure 3.6: Reactive zones as a fraction of domain volume for (a) AR, (b) S-DN, and (c) G-DN. Reactive zones are defined by areas where 20 % of the maximum reaction rate (μ_{max}) of the respective solute is exceeded (data from base case).

Similar to the HFC and the aerobic zone, upwelling groundwater reduces the size of the reactive fringe, resulting in smaller areas where conditions for S-DN and G-DN are met (Figures 3.6b and 3.6c). Subsequently, both S-DN and G-DN consumption rates decrease with increasing q_{bot} (Figures 3.5b and 3.5c). Consumption rates of S-DN decline more rapidly in response to increasing q_{bot} than those of G-DN, reflecting the fact that the size of the S-DN reactive zone is more sensitive to increases in q_{bot} than the size of the reactive zone of G-DN (Figures 3.6b and 3.6c). In contrast to S-NO_3, the influx of G-NO_3 increases with increasing q_{bot} (triangles in Figure 3.5a) leading to a larger mass of G-NO_3 in the modeling domain. Both $F_{G\text{-}NO3}$ and $F_{S\text{-}NO3}$ decrease with increasing q_{bot} (Figures 3.5d and 3.5e) indicating that upwelling groundwater has a strong effect on DN potential in the HZ. However, large amounts of both S-NO_3 and G-NO_3 are not consumed by DN and consequently exfiltrate to the stream, as discussed in section 3.4.3. Under low q_{bot} conditions (0.125 to 1 m/d), three major "hot spots" of S-DN and G-DN can be observed longitudinally within the reactive fringe surrounding the anaerobic zone (Figure 3.3e and 3.3f):

1. at the stagnation point, at the deepest point of the minor HFC where flow velocities are small in all directions (x = 12 m)

2. at the deepest extent of the major flow cell, where vertical velocity is nearly zero (x = 13 to 15.5 m)

3. beneath the area where water from the HZ is exfiltrating back to the stream (x = 17 m).

With increasing q_{bot}, the stagnation hot spot (1) disappears as the minor flow cell is increasingly suppressed, and the deep (2) and exfiltrating (3) hot spots merge into a single spot located at the deepest point of the HFC. Although the locations of the "hot spots" of both S-DN and G-DN are relatively similar, highly reactive zones of S-DN are larger than those of G-DN when q_{bot} is low. With increasing q_{bot} the highly reactive zones of G-DN are slightly larger (Figures 3.6b, 3.6c, and 3.7). Laterally, the reactive fringe decreases in depth toward the stream bank, becoming closer to the stream-sediment interface (Figure 3.7). Next to the stream bank, the highest DN rates can be observed in a narrow zone (around x = 13.5 m), where flow velocities are relatively small.

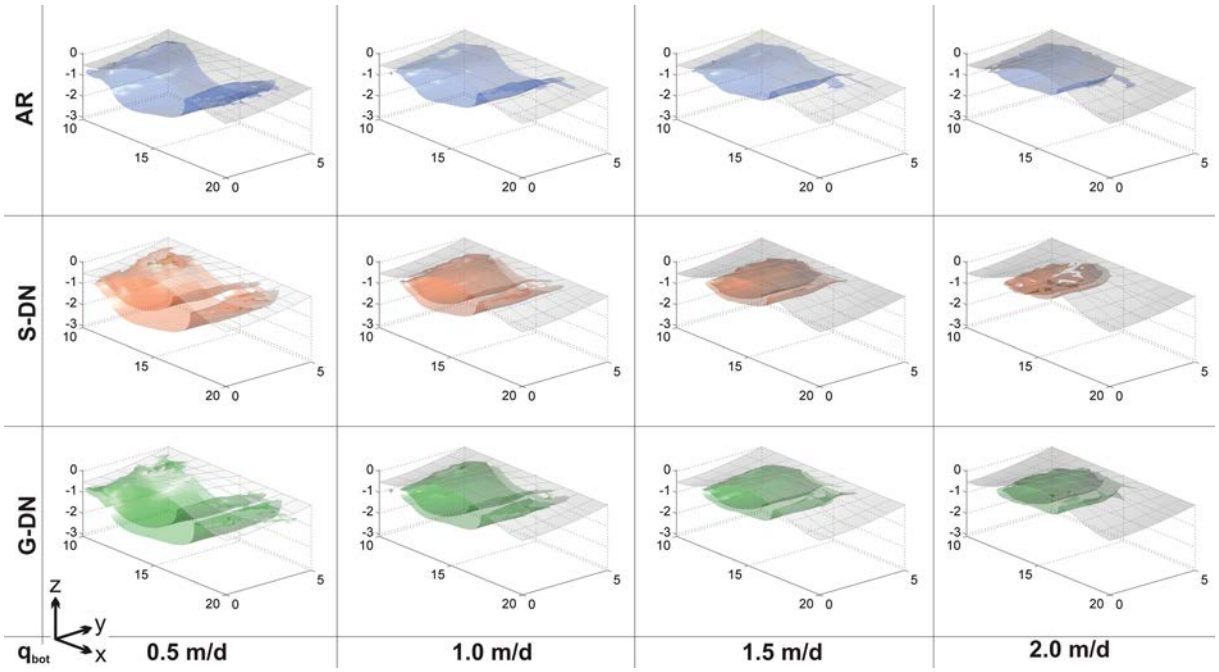

Figure 3.7: Three-dimensional view of the distribution of (top) AR, (middle) S-DN, and (bottom) G-DN within the HZ for various gaining conditions for $Q_{surf} = 7.4\,\mathrm{m}^3/\mathrm{s}$. Isosurfaces represent 20 % of the maximum reaction rate (μ_{max}) of the respective solutes and, hence, enclose high reactive zones, named as "reactive fringes" for S-DN and G-DN (data from base case scenario).

3.3.1.3 Losing Conditions (q_{bot}<0)

Under losing conditions, the influx of solutes from the stream and the size of the aerobic zone increase with increasing q_{bot} (Figure 3.4a and 3.6a). For high negative q_{bot} magnitudes, the bulk of the solutes infiltrating at the upstream side of the riffle are transported toward the lower bottom boundary, while a smaller fraction reinfiltrates to the stream at the downstream side of the riffle (Figure 3.2i to 3.2l). Laterally, the aerobic zone does not change significantly in extent or depth, and aerobic conditions are present across the entire width of the stream.

In general, the influx of O_2 and its consumption increase with negative magnitude of q_{bot} (Figure 3.4a and 3.4b). Under strongly losing conditions ($q_{bot} < 1\,\mathrm{m/d}$), the O_2 influx increases linearly with q_{bot} whereas O_2 consumption increases up to a constant level (Figure 3.4b). As a result, the maximum F_{O2} ($F_{O2} = \sim 0.85$) occurs at slightly losing conditions (-1 to -0.5 m/d), representing the q_{bot} at which the relationship between the influx of O_2 and DOC, and the solute residence time within the modeling domain are at an optimum with respect to oxygen consumption. Beyond this maximum, F_{O2} decreases with increasing magnitude of losing conditions, indicating a fast transport of O_2 through the modeling domain under constant consumption. Consequently, the amount of unreacted O_2 leaving the modeling domain at the bottom boundary increases also with an increasing magnitude of losing q_{bot}. However, the presumably continuing AR reaction outside the modeling domain is not captured by our model, a limitation that is discussed in detail in section 3.4.1. Under losing conditions, the zone of anaerobic conditions is small relative to the aerobic zone. Hence, major S-DN exists only in deep regions of the modeling domain, below the downstream side of the riffle, where flow velocities are extremely low (Figure 3.3h). These zones of S-DN quickly shrink with increasingly negative q_{bot} (Figure 3.6b) resulting in decreasing consumption rates of S-DN (Figure 3.5b). Thus, the high S-NO_3 influx cannot be

denitrified in the modeling domain and the bulk of S-NO_3 exits the domain unreacted across the bottom boundary, where under real conditions S-NO_3 can potentially be consumed in the aquifer (also see discussion in section 3.4.1). Toward the stream bank, aerobic and anaerobic conditions do not change significantly, and hence, also S-DN is relatively constant in lateral direction.
The consumption rates of S-DN under losing conditions are significantly higher than under gaining conditions (Figure 3.5b), because the size of zones of S-DN are larger (Figure 3.6b) and maximum degradation rates of S-NO_3 (0.04 mmol/L/d) are reached (Figure 3.3h). The maximum degradation rates are the result of a higher supply of S-NO_3 and DOC across the streambed, and the higher concentration of S-NO_3 and DOC in deep zones of the modeling domain (Figure 3.2j and 3.2k).

3.3.2 Impact of Streambed Morphology and Stream Discharge (Base Case)

The morphology of the pool-riffle sequence (differing by the amplitude forms) affects the size of the HFC, and thus the size of the reactive zone within the HZ, and the influx of solutes from the stream. Fluxes of O_2, DOC and S-NO_3 are significantly higher with the A05 morphology relative to A01 (Figure 3.4a and 3.5a) due to stronger hydraulic head gradients between the upstream and the downstream side of the more pronounced streambed morphology of the A05 [Cardenas and Wilson, 2007a; Trauth et al., 2013]. Both AR and S-DN, described by the values of F_{O2} and $F_{S\text{-}NO3}$, are more efficient in morphology A01, especially under gaining conditions (Figure 3.4c and 3.5d), due to the significantly lower solute influx. In contrast, the groundwater-borne G-NO_3 is degraded with higher efficiency in morphology A05 (Figure 3.5e), because G-NO_3 influx is not controlled by morphology, but by groundwater upwelling (q_{bot}).
Higher stream discharges increase the pressure gradient between upstream and downstream side of the riffle of A05 morphology [Trauth et al., 2013]. As a result, the solute influx is higher and the reactive zones are larger, leading to higher consumption rates of AR and DN (Figure 3.4a, 3.4b, 3.5a to 3.5c, and 3.6), consistent with the results of Bardini et al. [2012]. However, the increase in consumption rates due to increases in discharge is not as large as the corresponding increase in solute influx. Consequently, F_{O2} and $F_{S\text{-}NO3}$ are low under high stream discharge for the A05 morphology, resulting in an overall lower reaction efficiency of the HZ (Figure 3.4c and 3.5d). For the shallower A01 morphology, F_{O2} and $F_{S\text{-}NO3}$ are hardly affected by variations in discharge. In contrast, $F_{G\text{-}NO3}$ increases with stream discharge for both morphologies, because the larger reactive zones evoke higher consumption rates, but the influx of G-NO_3 remains constant since it is only controlled by q_{bot} magnitude (Figure 3.5e). Nonetheless, stream discharge has a minor impact on the reactions in the HZ, compared to changes in the magnitude of ambient groundwater flow.

3.3.3 Influence of O_2 Concentration in Upwelling Groundwater (Scenario #1)

In scenario #1, the input concentration of O_2 at the bottom boundary varied in the range of 0 to 0.234 mmol/L (0 to 7.5 mg/L), while all other solute concentrations and stream discharge (low $Q_{surf} = 7.4\,m^3/s$) were kept constant. When O_2 infiltrates the lower boundary, the entire lower part of the model domain is aerobic in addition to the upper, downwelling-driven aerobic zone (Figures 3.8a, 3.8e, and 3.8i). However, due to the lack of a carbon source (DOC) in the

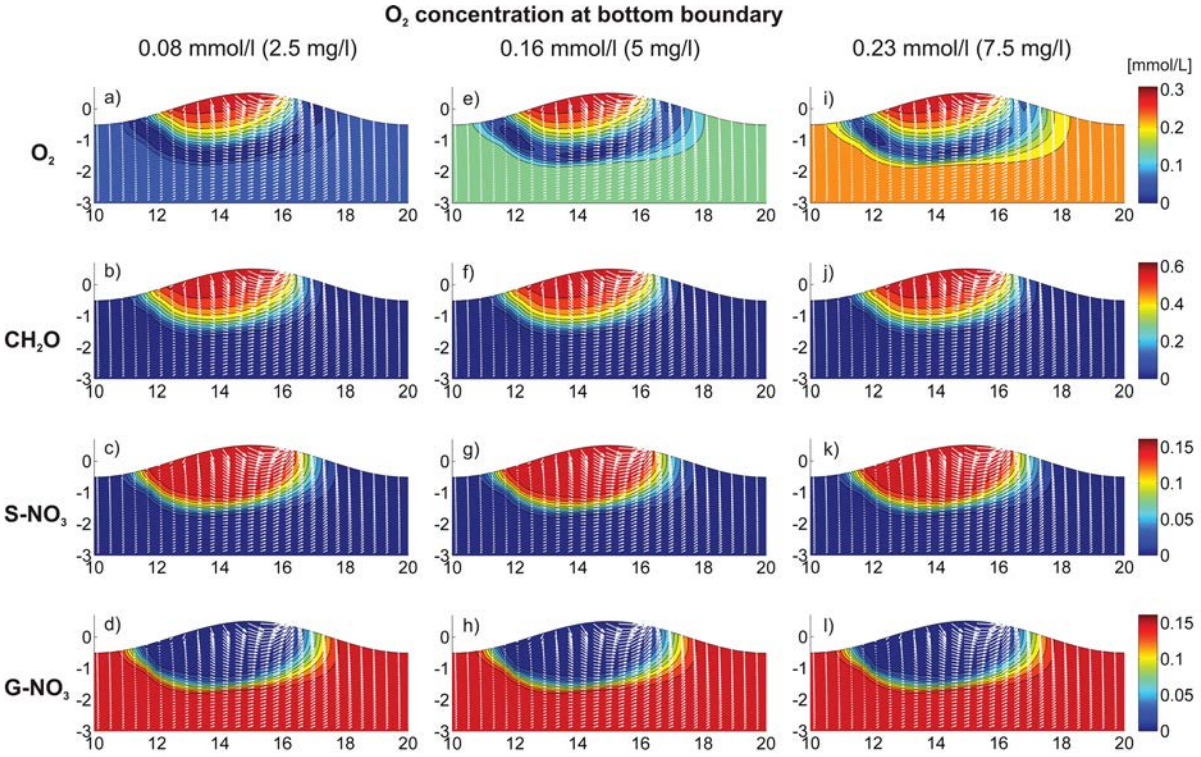

Figure 3.8: Cross sections of solute concentration along the x-z-plane at location y = 0.4 m under various O_2 concentrations at the bottom boundary. The vectors depict the direction of the hyporheic flow. Stream flow direction is from left to right. Simulated using the scenario #1 with low stream discharge $Q_{surf} = 7.4\,\mathrm{m}^3/\mathrm{s}$.

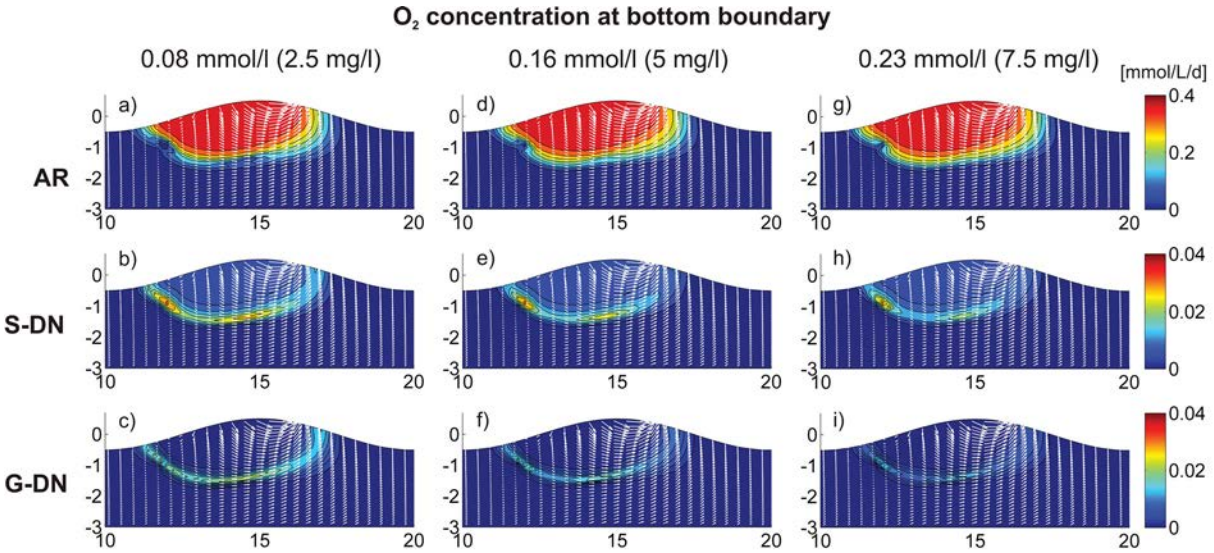

Figure 3.9: Cross sections of of solute consumption rates along the x-z-plane at location y = 0.4 m under various O_2 concentrations at the bottom boundary. The vectors depict the direction of the hyporheic flow. Stream flow direction is from left to right. Simulated using the scenario #1 with low stream discharge $Q_{surf} = 7.4\,\mathrm{m}^3/\mathrm{s}$.

upwelling groundwater, O_2 contained in the upwelling groundwater is conservatively transported through the lower parts of the modeling domain. Only where DOC from the stream is available, at the fringe of the upper aerobic zone, consumption of groundwater-borne O_2 by AR can be observed (Figures 3.9a, 3.9d, and 3.9g). The propagation of DOC within the HZ is controlled by the size of the HFC and decreases with increasing q_{bot}. Hence, the potential of AR in groundwater is constrained by the distribution and presence of DOC. As a result, the total consumption of O_2 increases only slightly with increases in O_2 concentration of the groundwater (Figure 3.10a). Furthermore, the reactive fringes of S-DN and G-DN observable in the base case become partially aerobic, conditions for DN become spatially limited, and consumption of S-NO_3 and G-NO_3 decrease (Figures 3.10b, 3.10c and 3.9). Similarly, F_{O2}, $F_{S\text{-}NO3}$, and $F_{G\text{-}NO3}$ decrease with increasing O_2 influx at the bottom boundary. As a consequence, highest DN efficiency in the HZ is reached when the magnitude (q_{bot}) and O_2 concentration of upwelling groundwater are low.

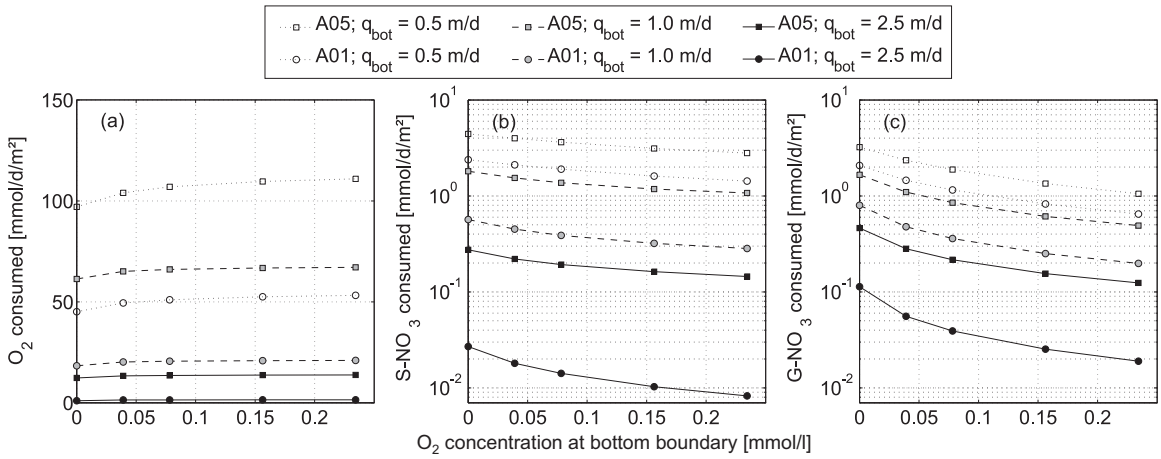

Figure 3.10: Consumption rates of (a) O_2, (b) S-NO_3, and (c) G-NO_3 under varying O_2 concentrations at the lower bottom boundary. Simulated using scenario #1.

3.3.4 Influence of G-NO_3 Concentration in Upwelling Groundwater (Scenario #2)

In scenario #2, simulations with different concentration of G-NO_3 at the bottom boundary in the range of 0.08 to 1.61 mmol/L (5 to 100 mg NO_3/L) are performed, while all other solute concentrations and stream discharge (low Q_{surf}) were kept constant (Figure 3.11). In general, G-NO_3 consumption increases with G-NO_3 concentration (Figure 3.12 and 3.13a). The variation of G-NO_3 does not affect AR or S-DN (Figure 3.12). The highest G-NO_3 consumption rates are observed at the highest G-NO_3 concentrations coupled with the lowest q_{bot} (0.5 m/d) (Figure 3.13a). Under these conditions the residence time of solutes within the HZ, the size of the HFC, and the corresponding aerobic zone and reactive fringe where DN occurs, are large (Figures 3.12c, 3.12f, and 3.12i). Furthermore, the reaction rate in the Monod kinetic is on high level, due to high G-NO_3 concentrations. Further increases in G-NO_3 concentration, while holding q_{bot} constant, do not result in significant further increases in absolute G-NO_3 consumption indicating that the maximum denitrification potential has been reached (Figure 3.13a). Denitrification potential is therefore limited by the size of the reactive fringe beneath the aerobic zone. In contrast, highest $F_{G\text{-}NO3}$ is observed at low G-NO_3 concentrations coupled with low q_{bot} (Figure

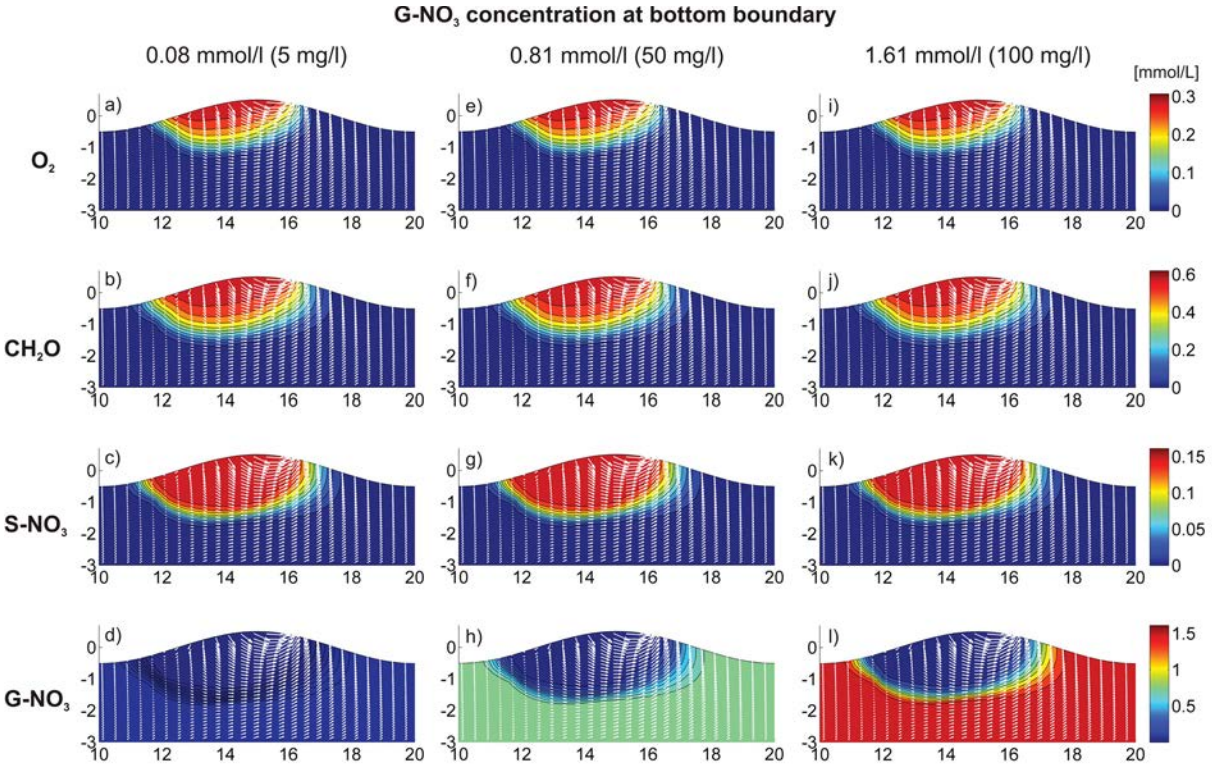

Figure 3.11: Cross sections of solute concentration along the x-z-plane at location y = 0.4 m under various NO_3 concentrations at the bottom boundary. The vectors depict the direction of the hyporheic flow. Stream flow direction is from left to right. Simulated using the scenario #2 with low stream discharge $Q_{surf} = 7.4\,\mathrm{m}^3/\mathrm{s}$.

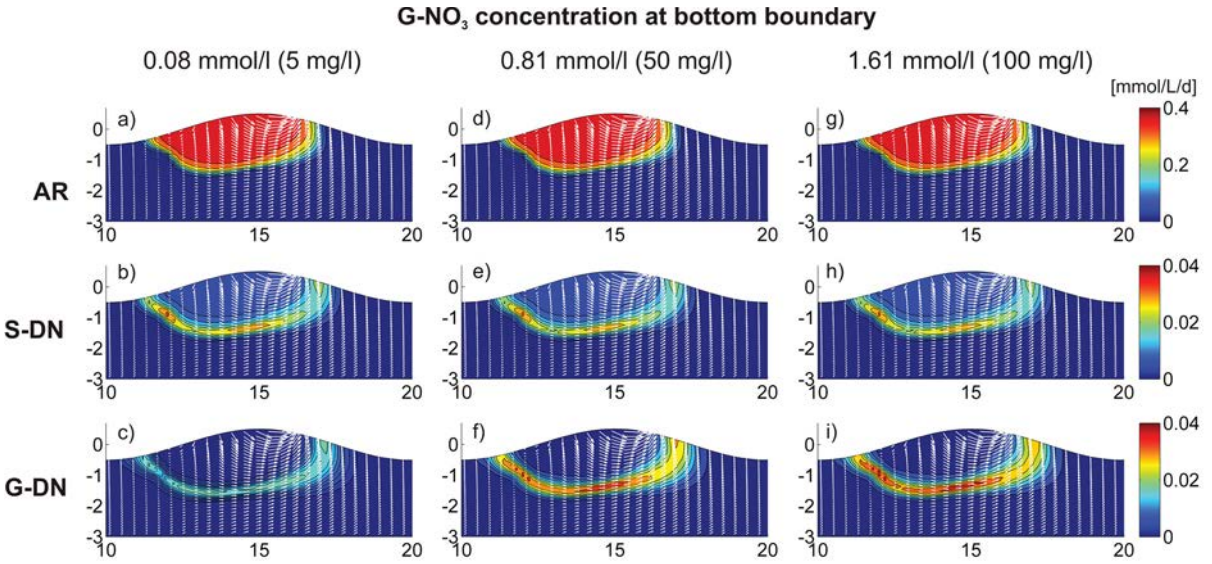

Figure 3.12: Cross sections of of solute consumption rates along the x-z-plane at location y = 0.4 m under various NO_3 concentrations at the bottom boundary. The vectors depict the direction of the hyporheic flow. Stream flow direction is from left to right. Simulated using the scenario #2 with low stream discharge $Q_{surf} = 7.4\,\mathrm{m}^3/\mathrm{s}$.

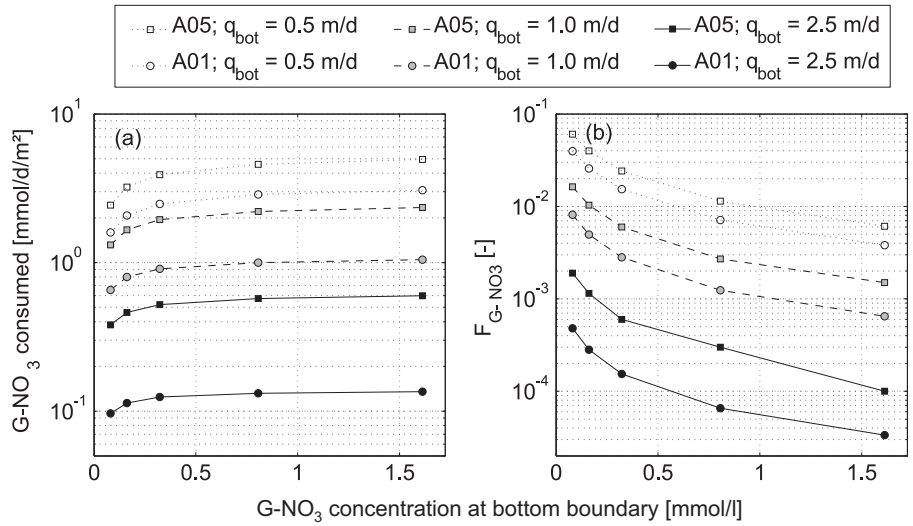

Figure 3.13: (a) Consumption rate of G-NO_3 as a function of the G-NO_3 concentration at the bottom boundary. (b) G-NO_3 consumed as a fraction of the total G-NO_3 influx ($F_{G\text{-}NO3}$). Simulated using scenario #2.

3.13b), when the G-NO_3 influx is lowest. In turn, under high q_{bot} and high G-NO_3 concentrations only small G-NO_3 fractions are consumed due to the high G-NO_3 influx, small reactive zones, and short residence times. These conditions result in the highest G-NO_3 fluxes exfiltrating into the stream across the streambed.

3.4 Discussion

3.4.1 Factors Controlling AR and DN in the HZ

In this study, we systematically analyze the impact of bedform morphology, stream discharge and ambient groundwater flow magnitude, direction, and chemistry on biogeochemical reactions in the HZ of a pool-riffle stream. Our results show that under gaining conditions AR and DN potential in the HZ strongly depend on the size of the hyporheic flow cells (HFC) and the influx of solutes to the HZ. Here the size of the reactive zone for AR is directly controlled by the size of the HFC as is the size of a reactive fringe for anaerobic reactions surrounding this aerobic zone and retention times within the HZ [Trauth et al., 2013]. Consequently, factors that influence the size of the HFC in turn affect the potential for AR and DN in the HZ. The size of the HFC, and subsequent potential for AR and DN, is highly sensitive to the magnitude of upwelling groundwater during gaining conditions. Under losing conditions, the influx of solutes across the streambed is also controlled by morphology, stream discharge and the magnitude of q_{bot}. However, in contrast to the gaining case, AR and DN are uncorrelated with the extent of the HFC, because reactions also occur outside of the HFC. While the size of the HFC decreases with magnitude of q_{bot} [Trauth et al., 2013], the size of the AR zones increase and exceed the HFC. Hence, under losing conditions consumption of O_2 is controlled by the residence time in the modeling domain, decreasing with increasing magnitude of q_{bot}. When infiltrating O_2 is significantly consumed during downward flow, reaction rates of DN are high. Under these conditions, reactive zones of DN not only surround the aerobic zones in a narrow reactive fringe but are also present in larger contiguous areas.

With increasing q_{bot}, the fraction of solutes that leaves the model domain across the bottom

boundary increases. In a real system, these solutes would continuously react beyond the extent of our theoretical modeling domain as long as a DOC source is available. Supposing no return of the infiltrated solutes to the river by upwelling farther downstream, first O_2 and subsequently S-NO_3 would presumably be significantly consumed on the flow through the underlying aquifer. However, these reactions are not captured by our model. As a result, higher AR and S-DN consumption rates can presumably be expected, than shown in our study for the losing case. This poses the question of the adequate depth of the modeling domain in order to reliably capture all reactions. Increasing the extent of the model domain would include further reactions. However, depending on the magnitude of the vertical flux, fractions of O_2 or S-NO_3 and DOC will still be leaving the modeling domain at the bottom, and not all reactions will be fully captured. Hence, the adequate domain depth also depends on the magnitude of q_{bot}: The higher the magnitude of q_{bot}, the deeper the lower model boundary has to be in order to entirely capture all reactions within the modeling domain. We think that despite this limitation, our model demonstrates that for the losing case the magnitude of ambient groundwater flow essentially controls solute transport and, hence, also efficiency of AR and DN in the HZ.

Although stream discharge and riffle morphology influences the size of the HFC by dictating the pressure gradient between upstream and downstream side of the riffle [Trauth et al., 2013], their impact on the size of the HFC, and in turn on AR and DN in the HZ, is minor in comparison to the influence of the magnitude of ambient groundwater flow.

Under gaining conditions the observed reactions between solutes from the stream water and from the groundwater imply that these solutes are mixed via dispersion. Jin et al. [2010], Hester et al. [2013], and Bardini et al. [2012] reported large effects of dispersivity on solute mixing in artificial numerical models of the hyporheic zone. Therefore, using higher dispersivities in our model parameterization likely would have generated larger reactive zone for G-DN. However, we intentionally kept dispersivity constant in all simulations in order to derive the impact of hydraulic and morphological factors on reactions in the HZ. Dispersivity values used in our model are at the upper end of the range of those used in comparable studies [Marzadri et al., 2012; Bardini et al., 2012; Jin et al., 2010; Hester et al., 2013] and decreasing these values would lead to a further decline in reactivity potential of the HZ.

3.4.2 Residence Times and Correlated Reactions in the HZ

Based on particle tracking Trauth et al. [2013] calculated flux-weighted residence times (RT) for flow paths within HFC for the different flow scenarios. The relationship between the median of the RTs (MRTs) and F_{O2} and $F_{S\text{-}NO3}$ can be approximated by power functions as shown in Figures 3.14a to 3.14d. These results agree with the findings of Pinay et al. [2009], Boano et al. [2010], Zarnetske et al. [2011a] and Marzadri et al. [2012] who showed that O_2 and NO_3 concentrations decrease with increasing RT. However, it should be emphasized that the MRTs of Trauth et al. [2013] do not include the RT of flow paths outside the HFC, directed from domain bottom to the streambed and vice versa. Consequently, upwelling G-NO_3 does not react along its path until it reaches the reactive fringe and mixes with DOC derived from the stream, leading to a weak correlation with the MRTs (Figure 3.14e). Also, under losing conditions the consumption of O_2 and S-NO_3 outside the HFC cannot be physically related to the MRTs. The correlation between F_{O2} and $F_{S\text{-}NO3}$ and the MRT of Trauth et al. [2013] under losing conditions

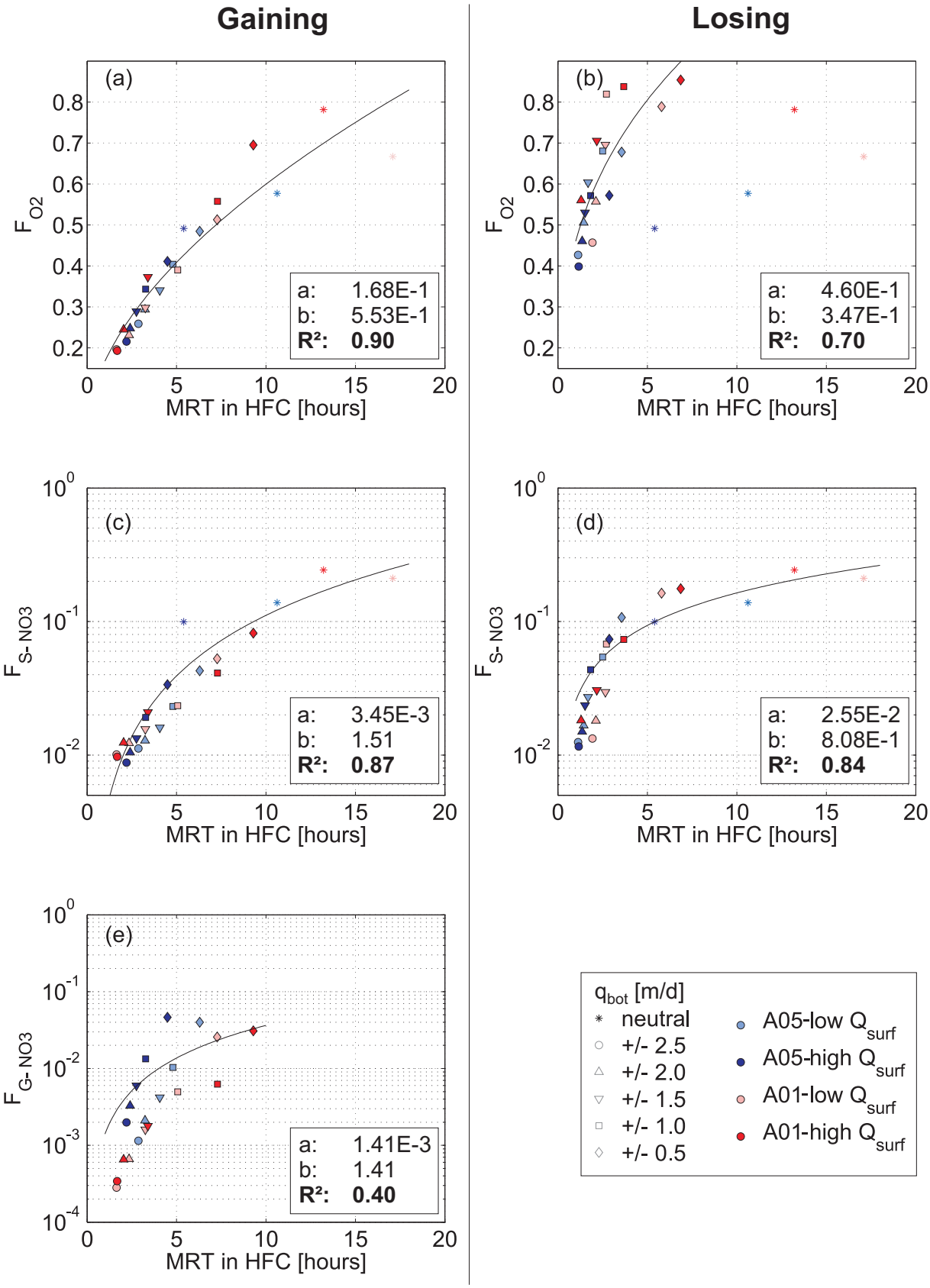

Figure 3.14: Solute consumption as a fraction of total influx (F_{O2}, $F_{S\text{-}NO3}$, and $F_{G\text{-}NO3}$) as a function of the median residence times (MRTs) from Trauth et al. [2013]. Black lines represent fitted power functions of the type $F_{Species} = a \times MRT^b$. Fitting parameters a, b, and R^2 are included in the figures. For the fit of F_{O2} under losing conditions (Figure 3.14b) the outliers of the neutral case are excluded. Note that the MRTs refer to residence times within the hyporheic flow cell (HFC) and not necessarily to the timing of the reactions (see explanations in section 3.4.2). Data are from base case scenario.

(Figures 3.14b and 3.14d) are based on the strong relation between the RTs within the HFC and the RTs outside the HFC: By increasing the magnitude of losing q_{bot}, the magnitude of the hydraulic gradient between upper and lower model boundary increases, leading to shorter RT in the entire modeling domain and hence a simultaneous decrease of RT within and outside the HFC. In conclusion, only the correlations between F_{O2} (AR) and $F_{S\text{-}NO3}$ (S-DN) under gaining conditions and the MRT of Trauth et al. [2013] are physically meaningful (Figures 3.14a and 3.14c) as justified by high correlations ($R^2 > 0.87$).

For an accurate assessment of AR and DN in the HZ using RTs, it is important to ensure, that the RTs are correlated with these reactions. Relating aerobic and anaerobic zones in the HZ to RTs, as reported by Zarnetske et al. [2011a] and Marzadri et al. [2012], is not feasible in our study. In particular, the reactive fringe of G-DN under gaining conditions is not related to either the RTs of upwelling groundwater or to RTs of flow within the HFC. Instead, the occurrence of the reactive fringe is based solely on the mixing of two reactants, the DOC of stream water and G-NO_3, independent of hyporheic RTs. Mixing of solutes within the HZ was recently studied by Hester et al. [2013], who observed that only 12.7 % of an upwelling conservative tracer was mixed with infiltrating stream water. They conclude that reactions in the HZ depend on solute mixing in addition to residence times, which supports our results for upwelling G-NO_3 and O_2. Although residence times can be a valuable proxy for assessing reactivity in hydrology, a profound conceptual understanding of flow paths and solute concentrations involved in the reactions is essential.

3.4.3 Potential of AR and DN in the HZ of Pool-Riffle Systems

The simulated rates of O_2 consumption ($\leq 360\,\mathrm{mmol/d/m^2}$) are within the range observed in field studies [Hall and Tank, 2005; Uehlinger, 2006; Edmonds and Grimm, 2011]. The range of simulated NO_3 consumption rates (0.02 to $23\,\mathrm{mmol/d/m^2}$) is likewise in line with denitrification rates observed in streambed sediments [García-Ruiz et al., 1998; Laursen and Seitzinger, 2002; Opdyke et al., 2006; Arango et al., 2007; Birgand et al., 2007; Wagenschein and Rode, 2008; Pinay et al., 2009]. Our results indicate that the HZ has a significantly higher potential for net consumption rates of AR compared to DN. Under neutral conditions ($q_{bot} = 0$), the consumption rate of O_2 is up to 10 times higher than the consumption rate of S-NO_3. This relation is generally in line with the findings by Kessler et al. [2012] who observed a dominance of AR, with consumption rates of up to 20 times higher than for DN in a flume where ambient groundwater was not considered. However, for large magnitudes of q_{bot} ($q_{bot} > 1$ and $q_{bot} < -1$), consumption rates for AR and DN (sum of consumption rates of S-NO_3 and G-NO_3) may be different by up to a factor of 70. These relations indicate that DN is highly sensitive to ambient groundwater flow, whereas variability in AR is not as strongly affected by q_{bot}.

We emphasize that our simulations only take the HZ of pool-riffle systems into account. Streambed morphologies on smaller and larger scales, like dunes and ripples [Bardini et al., 2012], meanders [Boano et al., 2010], and the riparian zone [Gu et al., 2012] also contribute to the integrated denitrification potential of a fluvial system. Furthermore, processes of N assimilation by benthic biofilms and macrophytes are not considered in our model but also play an important role in the N–cycle [Birgand et al., 2007].

Reducing NO_3 concentrations in the stream water is possible through exfiltration of reacted water with lower NO_3 concentrations from the HZ into the stream. The source of this exfiltrating hyporheic water depends highly on losing or gaining conditions. Under losing conditions, the flux of infiltrating S-NO_3 is both recirculated back to the stream at the downstream side of the riffle and leaves the domain across the bottom boundary, reaching the groundwater (Figures 3.15a and 3.15b). The recirculated fraction is transported within the HFC and is partially consumed by S-DN (red markers in Figure 3.15c) whereas the groundwater fraction is consumed on the flow paths toward the bottom boundary (green markers in Figure 3.15c). The major reactive potential therefore exists outside the HFC, except under very slight losing conditions ($q_{bot} > -0.25$ m/d). However, from the perspective of the stream water, only S-NO_3 that is degraded within the HFC can directly affect NO_3 concentrations in the stream. Hence, under losing conditions, the HZ always acts as a sink for stream NO_3. Up to 90 % of the S-NO_3 influx is flowing toward the groundwater (green markers in Figure 3.15b), and is temporarily removed from the fluvial system. This fraction does not directly affect NO_3 concentrations in the stream within the span of an individual pool-riffle sequence. Outside the HFC S-DN is more effective, contributing to potential decreases in NO_3 concentrations in deeper areas beneath the streambed as long as a carbon source is available. Eventual upwelling of this water, e.g., farther downstream of the river, should therefore decrease NO_3 concentration in the stream over a larger scale.

Under gaining conditions upwelling groundwater contributes an additional source of NO_3 to the stream. Our model shows that DN in the HZ does not have the potential to completely degrade the upwelling G-NO_3 (Figure 3.15c) and the residuals of unreacted G-NO_3 and S-NO_3 exfiltrate to the stream (Figure 3.15a, and black line in Figure 3.15b). When G-NO_3 concentration exceeds the concentration in the stream water, in-stream NO_3 concentration increases (model set up of scenario #2). In reverse, when G-NO_3 infiltrates

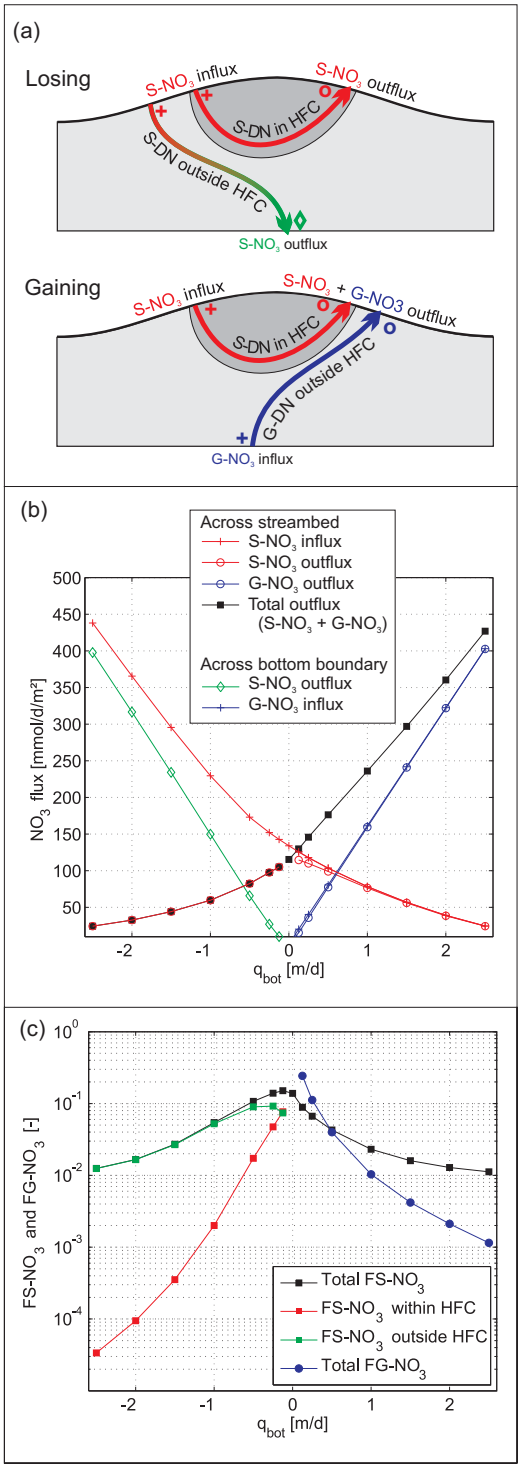

Figure 3.15: (a) Conceptual flow paths of S-NO_3 and G-NO_3 under losing and gaining conditions and (b) S-NO_3 and G-NO_3 flux across the streambed and the bottom of the domain; markers correspond to those shown in the conceptual panel. (c) Separation of $F_{S\text{-}NO3}$ into specified area of reaction within the HFC and outside. $F_{S\text{-}NO3}$ within the HFC possibly affects stream water chemistry, whereas $F_{S\text{-}NO3}$ outside the HFC contributes to the groundwater (base case, low $Q_{surf} = 7.4\,\mathrm{m^3/s}$).

the HZ with concentrations already lower than in the
stream, NO_3 concentrations in stream water decrease by dilution. In this case, the hyporheic NO_3 "sink" is not based on biogeochemical processes but rather on simple mixing of high in-stream NO_3 concentrations with lower G-NO_3 concentrations. Under neutral conditions the HZ still acts as a NO_3 sink for the stream, but in this case solely due to consumption of S-NO_3, and not of solutes derived from the groundwater (Figures 3.15b and 3.15c at $q_{bot} = 0$ m/d). This is in line with previous reactive transport studies [Bardini et al., 2012; Kessler et al., 2012; Marzadri et al., 2012], where the ambient groundwater flow is not considered and NH_4 concentrations are low. In our study, we assume quasi-pristine stream water with negligible NH_4 concentrations in comparison to NO_3, and thus we assume nitrification is an insignificant process [Hill et al., 1998; Storey et al., 2003; Kasahara and Hill, 2006]. However, if NH_4 concentrations are high relative to NO_3 concentrations, nitrification can contribute a significant source of NO_3 from the HZ [Jones et al., 1995; Duff and Triska, 2000; Bardini et al., 2012; Marzadri et al., 2012]. Nonetheless, an additional source of NO_3 from nitrification would not significantly increase the potential of DN, because the limitations of restricted reactive areas and short residence times still exist.

3.5 Conclusion

In this study, we used reactive transport simulations through the sediments of 3-D pool-riffle streambeds to investigate biogeochemical process in the HZ. To our knowledge, this is the first study to systematically analyze the impact of ambient groundwater flow (losing and gaining conditions) on aerobic respiration (AR) and denitrification (DN) in the HZ. Our results demonstrate the strong impact of ambient groundwater flow on the distribution and extent of redox zonation in the HZ. The flux of solutes into the HZ, their residence times, and the size of the reactive zones are all influenced by the presence, magnitude, and direction of ambient groundwater flow (q_{bot}). Upwelling groundwater decreases the RTs and the size of the reactive zone of AR. A smaller aerobic zone also results in a smaller reactive fringe where favorable conditions for DN exist. Hence, reactions in the HZ are significantly reduced by upwelling groundwater. Here AR efficiency is up to 4 times lower when magnitude of q_{bot} is high compared to when groundwater flow is absent (neutral condition, $q_{bot} = 0$). Also, high magnitudes of q_{bot} decrease efficiency of S-DN by more than an order of magnitude and G-DN by up to 3 orders of magnitude. Comparing net consumption rates, the HZ has a significantly higher potential for AR compared to DN.
Under slightly losing conditions, AR and DN are mainly controlled by the residence time (RT) of solutes within the HZ. Depending on the magnitude of negative q_{bot}, and the resulting hyporheic RTs, a portion of the infiltrating solutes exfiltrate back to the stream (Figures 3.15a and 3.15b). However, for $q_{bot} < -0.5$ m/d, the bulk of the infiltrating solutes are not restricted to the extent of the HFC and flow downward to the lower model boundary. Here the solutes leave the modeling domain, and hence, their possible reactions outside the domain are not captured by our model. Taking the continuing reactions outside the modeling domain into account would presumably increase total efficiency of AR and S-DN as long as the carbon source DOC is available. Despite these model limitations related to solutes leaving the modeling domain, our results show how losing ambient groundwater conditions dramatically decrease solute transport and reactions

along flow paths within the HFC (Figure 3.15c).

Rising stream discharge increases solute consumption rates but decreases consumption efficiencies. Exaggerated pool-riffle morphology (high pool-riffle amplitudes, A05) also increases consumption rates but efficiency of AR and S-DN is lower, due to increased solute influx. However, in comparison to the impact of ambient groundwater, stream discharge and morphology exert relatively minor control on hyporheic biogeochemistry.

Variations of O_2 and NO_3 concentrations in the groundwater show that the highest DN efficiency in the HZ is reached when concentrations of O_2 and G-NO_3 are low and the magnitude of upwelling groundwater is low as well. Furthermore, DN efficiency increases with decreasing O_2 concentration in upwelling groundwater (scenario #1).

The HZ of pool-riffles systems is able to significantly degrade organic carbon under aerobic conditions. However, under anaerobic conditions the maximum degradation of NO_3 is 27 % of the NO_3 influx into the HZ for conditions of no ambient groundwater flow (neutral case). However, slight ambient groundwater flow strongly decreases DN efficiency. These results demonstrate the significant control that groundwater flow magnitude and direction have on biogeochemical processes in the HZ underneath pool-riffle sequences.

4 | Hydraulic controls of in-stream gravel bar hyporheic exchange and reactions

This chapter is published as:
Trauth, N., C. Schmidt, M. Vieweg, S.E. Oswald, and J. H. Fleckenstein (2015), Hydraulic controls of in-stream gravel bar hyporheic exchange and reactions, *Water Resources Research*, 51, doi:10.1002/2014WR015857.

Abstract

Hyporheic exchange transports solutes into the subsurface where they can undergo biogeochemical transformations, affecting fluvial water quality and ecology. A three-dimensional numerical model of a natural in-stream gravel bar (20 m × 6 m) is presented. Multiple steady state stream flow is simulated with a computational fluid dynamics code that is sequentially coupled to a reactive transport groundwater model via the hydraulic head distribution at the streambed. Ambient groundwater flow is considered by scenarios of neutral, gaining and losing conditions. The transformation of oxygen, nitrate and dissolved organic carbon by aerobic respiration and denitrification in the hyporheic zone are modeled, as is the denitrification of groundwater-borne nitrate when mixed with stream-sourced carbon. In contrast to fully submerged structures, hyporheic exchange flux decreases with increasing stream discharge, due to decreasing hydraulic head gradients across the partially submerged structure. Hyporheic residence time distributions are skewed in the log-space with medians of up to 8 hours and shift to symmetric distributions with increasing level of submergence. Solute turnover is mainly controlled by residence times and the extent of the hyporheic exchange flow, which defines the potential reaction area. Although stream flow is the primary driver of hyporheic exchange, its impact on hyporheic exchange flux, residence times and solute turnover is small, as these quantities exponentially decrease under losing and gaining conditions. Hence, highest reaction potential exists under neutral conditions, when the capacity for denitrification in the partially submerged structure can be orders of magnitude higher than in fully submerged structures.

4.1 Introduction

Streambed structures enhance the exchange of water and solutes between the stream and the streambed sediments, known as hyporheic exchange [Harvey and Bencala, 1993; Packman et al., 2004]. Hyporheic exchange is typically characterized by complex flow processes at nested scales ranging from ripples and dunes to pool-riffles and gravel bars to meanders [Stonedahl et al., 2010]. Typically, stream water infiltrates at the upstream side of structures and exfiltrates back to the stream further downstream, at the lee side of the structure, as the result of spatially varying hydraulic heads across the streambed structure [Thibodeaux and Boyle, 1987; Elliott

and Brooks, 1997b; Tonina and Buffington, 2009a]. Solutes in the stream water are transported into the subsurface mainly advectively [Elliott and Brooks, 1997b; Packman et al., 2004]. Once in the streambed sediments solutes may undergo biogeochemical reactions that degrade nutrients and contaminants thus providing an attenuation or "self-cleaning" mechanism of stream systems. Furthermore, about 88 % of whole-stream ecosystem respiration has been attributed to processing within the hyporheic zone [Kaplan and Newbold, 2000]. When groundwater interacts with the stream, solutes from both the stream and groundwater compartments mix, leading to complex reaction patterns in the subsurface [Triska et al., 1993; McCutchan et al., 2002; Krause et al., 2013; Trauth et al., 2014].

The exchange flux and solute transport induced by submerged features like dunes, ripples and pool-riffles have been intensely studied in flume [Elliott and Brooks, 1997b; Tonina and Buffington, 2007; Fox et al., 2014] and numerical experiments [e.g. Cardenas and Wilson, 2007a; Janssen et al., 2012; Trauth et al., 2013]. Recently, reactive transport models were used to simulate reactions in the hyporheic zone at these scales, as presented by Bardini et al. [2012], Kessler et al. [2012], Hester et al. [2014] and Trauth et al. [2014]. However, the effects of hyporheic exchange on solute transformations in non-submerged features, including fluvial islands or in-stream gravel bars, have received less attention, although these morphological structures occur frequently in gravel bed rivers [Osterkamp, 1998] and are of great importance for stream-groundwater interactions [Shope et al., 2012]. In contrast to submerged features, the degree of submergence in partially submerged structures is controlled by stream water level, adding additional complexity to the hydraulic system that drives hyporheic exchange.

Several field studies have attempted to quantify water flow and residence time in non-submerged structures by using stream stage alone [Dent et al., 2007] and in combination with piezometric head data from the structure [Shope, 2009; Francis et al., 2010]. Residence times in the non-submerged structures have been estimated from artificial tracer additions [Dent et al., 2007; Zarnetske et al., 2011a] and through the use of natural variations of electrical conductivity [Schmidt et al., 2012]. Field observations combined with either two-dimensional [Cardenas, 2010] or three-dimensional modeling [Shope et al., 2012] approaches have also been used to estimate flow fields. However, to the best of our knowledge, biogeochemical reactions within the sediments of fluvial islands, and their controlling hydraulic factors, have not been considered yet.

In this study, we use a reactive transport model to investigate the impact of stream discharge and ambient groundwater flow conditions on hyporheic exchange flux, solute transport, aerobic respiration, and denitrification in the sediments of an in-stream gravel bar (ISGB). We apply multiple steady state three-dimensional computational fluid dynamics (CFD) simulations to the surveyed streambed morphology of a natural ISGB at the Selke River, Germany. Simulations for several steady state stream discharge conditions are combined with scenarios of gaining and losing groundwater flow conditions to provide a comprehensive range of hydraulic conditions of groundwater-surface water exchange. Furthermore, we use particle tracking to derive the residence times and the spatial orientation of the subsurface flow paths. Our study improves the understanding of complex hyporheic flow regimes and their biogeochemical implications and provides a quantitative method for assessing the reactive efficiency of in-stream gravel bars and their contribution to net fluvial solute retention.

4.2 Methodology

4.2.1 Field Site and Streambed Morphology Characterization

The Selke River is a third-order stream in the northern foreland of the Harz Mountains in central Germany (N51°43′37.29” E11°18°18′48.54”, and an intensive test site within the TERENO observatory (`http://teodoor.icg.kfa-juelich.de/observatories/HCGL_Observatory/hydrological-observatory-1/intensive-test-site-selke`). The Selke River has a long-term mean annual discharge of 1.5 m^3/s and is characterized by natural fluvial morphologies including meanders, pools and riffles, side bars, and in-stream gravel bars (ISGB). The stream slope averages to 1 % but is locally increased at pronounced pool-riffles and steps. We investigate an ISGB typical of the Selke and other third order gravel bed rivers. Under low flow conditions (0.18 m^3/s) the ISGB is 20 m long and 6.5 m wide (Figure 4.1a), and stream water flows through both stream channels surrounding the ISGB. Below 0.18 m^3/s the right (secondary) channel becomes disconnected and surface water flows only through the left (primary) channel, which is deeper and wider than the secondary channel. The non-submerged area of the ISGB decreases with increasing discharge until it is completely inundated at discharges > 3.6 m^3/s, resulting in a riffle structure. The specific rating curve (stage-discharge relationship) at the field site was calculated based on manual discharge measurements and automatically recorded stream stage.

The stream section surrounding the ISGB is composed of heterogeneous, predominantly gravelly

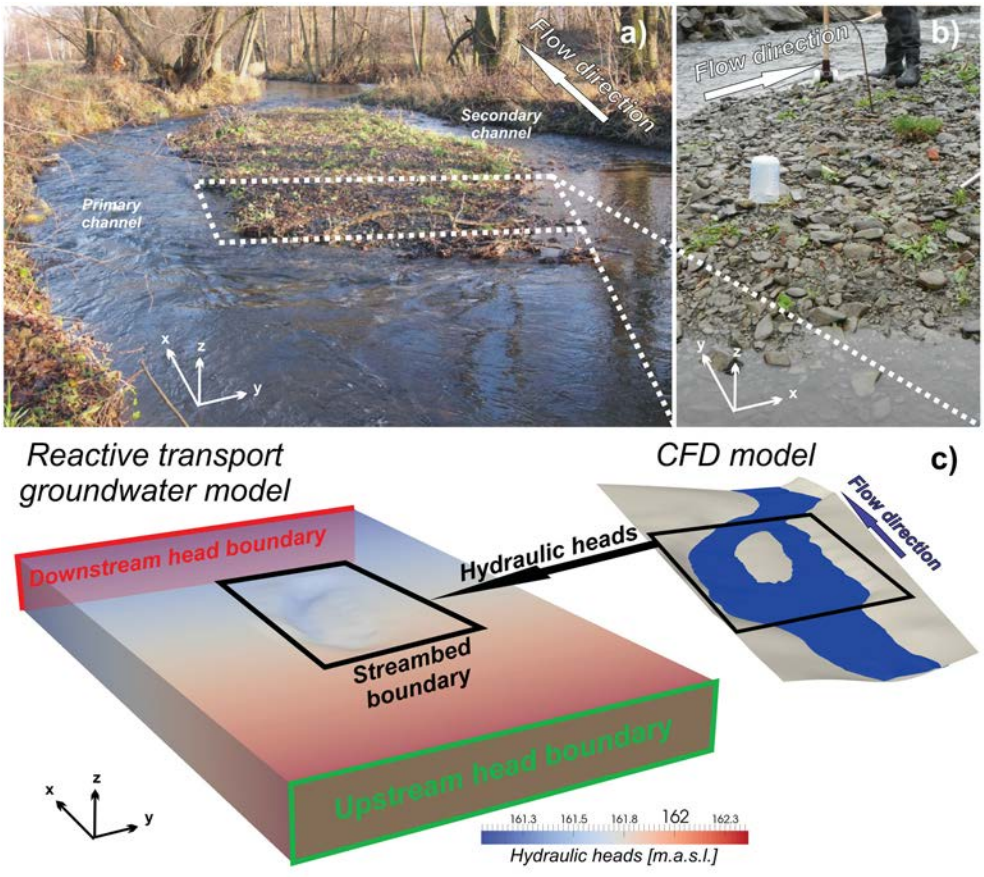

Figure 4.1: a) Photograph of the in-stream gravel bar studied, b) detailed photograph of the armor layer, and c) modeling domains of the CFD model and the reactive transport model including the hydraulic boundary conditions.

fluvial sediments with grain sizes ranging from medium sands to coarse gravels. Hydraulic conductivity of the streambed sediments, determined from slug tests and freeze coring, are in the range of 2.7×10^{-4} to 6×10^{-3} m/s. The top layer of the streambed is covered by an armor layer of cobbles (D16: 21 mm, D50: 42 mm, D84: 100 mm, sorting index: 4.76) (Figure 4.1b), which restricts considerable bed mobilization by the range of flows considered here. Drilling logs reveal clay and silt deposits at 10 m depth below the streambed which confine the bottom of the alluvial aquifer. Streambed morphology of the ISGB and the stream banks were surveyed by a differential GPS in combination with a laser tachymeter (Trimble GPS R8), measuring approximately 500 data points in total. The MATLAB tool gridfit (`http://www.mathworks.com/matlabcentral/fileexchange/8998-surface-fitting-using-gridfit`) was used to interpolate the surveyed data points and produce a highly resolved elevation map of the streambed surface. We use the term ISGB to refer to the entire morphological structure of an in-stream gravel bar, independent of the level of submergence. Thus, the term ISGB is still used if the in-stream gravel bar is completely inundated, even though the bar resembles a riffle structure under those conditions.
About 30 water samples each from the stream water and the groundwater were collected for chemical analysis during the summer months of 2012. Stream water was fully saturated with O_2. DOC concentrations of 8.0 mg/L and nitrate concentrations of around 10.0 mg/L were observed. In the groundwater dissolved oxygen concentrations ranged from 0 to 5.5 mg/L, depending on the distance from the stream. DOC concentrations were lower than 2.0 mg/L, and nitrate concentrations of more than 100 mg/L were observed.

4.2.2 Stream Water Simulations

Stream flow around the ISGB is simulated using the open-source CFD code OpenFOAM, which solves the Navier-Stokes equations with the Large-Eddy Simulation turbulence closure model. To simulate the subgrid scales, the original Smagorinsky subgrid scale model [Smagorinsky, 1963] is used with a filter width determined by the cubic root from the mesh cell volume. OpenFOAM provides two-phase simulations by the volume of fluid method [Hirt and Nichols, 1981], where both the air and the water fraction can be simulated. Hence, non-submerged areas of the ISGB for a specific discharge are simulated realistically as non-wetted areas. The CFD modeling domain comprises a stream section of 65 m in the stream flow direction (x) and 26.5 m in the lateral direction (y) (Figure 4.1c) and includes stream banks and stream sections upstream and downstream of the ISGB in order to avoid effects of inlet and outlet boundary conditions. The mesh consists of hexahedral cells with a maximum size of 0.26 m in the planar x and y direction, and 0.05 m in the vertical z-direction, resulting in a total of 604,111 cells.
Water enters the modeling domain 15 m upstream of the ISGB, with defined level and velocity. Inflow of air into the domain is predicted numerically. At the domain outlet water and air leave the domain unrestricted. A no-slip boundary condition was used for the streambed, analogous to similar studies that have coupled CFD models to porous media [Cardenas and Wilson, 2007a; Janssen et al., 2012; Kessler et al., 2012; Trauth et al., 2013]. Using a more complex roughness wall boundary would require a roughness length scale parameter, which can be derived from the grain size distribution. However, this parameter must be smaller than half the height of the near-bed cells to have an effect on near-bed velocity [Nicholas, 2001]. For the observed grain size distribution at our site, this length scale parameter is larger than half the height of the near-bed

cells, hence, we neglect grain roughness at the streambed and used the no-slip boundary. This simplification is further justified by earlier studies of Lane et al. [2004] and Janssen et al. [2012] who demonstrated that grain roughness has a negligible effect on the pressure distribution at the streambed, which in turn provides the crucial boundary condition for the subsequent coupling to the groundwater model. The lateral sides of the modeling domain are also treated as no-slip conditions, but, because the water fraction is bounded by the streambed channels, the lateral sides are only in contact with air. Further information on the CFD modeling is given in Trauth et al. [2013], which used similar CFD toolbox and boundary conditions, and to the OpenFOAM documentation at `www.openfoam.org`.

By setting an initial stream stage and velocity field in the modeling domain, the quasi steady state could be reached faster than with an initially empty domain. We simulated 10 steady state discharge scenarios, ranging from low discharges of $0.18 - 4.97\,\mathrm{m}^3/\mathrm{s}$, where the ISGB is completely inundated. Reactions in the open water are neglected in the surface water model, as they are assumed to be of minor importance for total whole-stream ecosystem respiration [Fuss and Smock, 1996; Naegeli and Uehlinger, 1997] and turnover, especially along short stream reaches, as considered in this study.

4.2.3 Reactive Transport Model

The hydraulic head distributions at the streambed surface, provided by the CFD simulations, are used as the upper hydraulic boundary condition for a reactive transport model of the subsurface, as in Trauth et al. [2013] and Trauth et al. [2014]. In contrast to these prior studies, which looked at fully submerged pool-riffle structures, this study includes an unsaturated zone up to 0.3 m thick, which decreases with increasing stream discharge. Only the hydraulic heads of the wetted areas of the ISGB are considered for the coupling process. Coupling between the surface and the porous domains is one-way sequentially; feedbacks to surface water flows resulting from subsurface flow into the surface water domain are not considered. This simplification is reasonable because the small fraction of total stream discharge derived from subsurface flows [Trauth et al., 2013] has a negligible effect on the hydrodynamics of the overall stream flow [Prinos, 1995].

For simulating steady state groundwater flow, and reactive transport in the subsurface of the ISGB, we use the groundwater flow and reactive transport code MIN3P, which solves the Richard's equation for variably saturated flow [Mayer et al., 2002]. Hydraulic heads are assigned as Dirichlet boundaries to the top layer of the groundwater model (Figure 4.1c). Dry parts of the streambed are defined as no-flow boundaries. Constant groundwater heads are assigned to the lateral boundaries upstream and downstream of the groundwater model domain, enabling an ambient groundwater flow field with a defined slope in the direction of stream flow. This slope is equal to the average longitudinal slope of the hydraulic head distribution at the streambed of the ISGB and, hence, varies slightly between each stream discharge scenario. We assign a range of groundwater heads at the upstream and downstream boundaries to induce an ambient groundwater flow field that interacts with the local flow field at the ISGB induced by hydraulic heads at the streambed. In this way we consider a wide range of possible hydraulic conditions at the ISGB, from losing to neutral (no net hydraulic gradient between groundwater and stream) to gaining conditions. The bottom of the domain, at a depth of 10 m below the streambed, is

treated as a no flow boundary, coinciding with the base of the alluvial aquifer. Similarly, the right and left panels of the domain are treated as no-flow boundaries. The ISGB is situated in the center of the domain, and the elevation of the top boundary matches the streambed morphology (Figure 4.1c).

Preliminary groundwater flow simulations, with stepwise enlarged model domains, were conducted in order to identify an appropriate model domain extent where the lateral boundaries would have negligible effects on fluxes across the streambed. Based on these simulations, the total extent of the groundwater model domain is set to 130 m in the direction of stream flow (x) and 80 m perpendicular to it (y). In total, the mesh of the groundwater model consists of 998,640 hexahedral cells. The mesh is refined around the ISGB with cell size of 0.35 m by 0.3 m in x and y direction. Toward the outer boundaries, the planar cell size increases to a maximum of 1.8 by 1.6 m. Vertically, the height of the mesh cells decreases by a quadratic function from a maximum height of 0.36 m at the domain bottom to a minimum of 0.005 m at the top layer (streambed). This mesh assures that the strong hydraulic and chemical gradients, and spatially varying reactions, expectable next to the streambed, are accurately captured.

Forward advective particle tracking is conducted using the open-source visualization software ParaView, Version 4.1.0 [Henderson et al., 2004], based on a fourth–fifth-order Runge-Kutta integration of the steady state pore water velocity field. Four particles per mesh cell are released at the wetted-streambed areas. Thus, the number of particles released varied between 11,219 and 21,135, depending on the size of the area that is fully submerged in the CFD-simulations. In subsequent analyses all particle tracks are flux weighted and evaluated with respect to their median residence time, distribution, and orientation in the subsurface.

The groundwater model MIN3P simulates transport of dissolved and gaseous species by advective-dispersive transport and Fickian diffusion processes, respectively [Mayer et al., 2002]. In our scenarios, we use MIN3P to simulate aerobic respiration and denitrification of DOC, represented by carbohydrate (CH_2O), according the following reaction equations:

Aerobic respiration:

$$CH_2O + O_2 \rightarrow CO_2 + H_2O \tag{4.1}$$

Denitrification:

$$5CH_2O + 4NO_3^- + 4H^+ \rightarrow 5CO_2 + 2N_2 + 7H_2O \tag{4.2}$$

According to equation 4.1 and 4.2, three solutes could react with the DOC source: Oxygen (O_2), nitrate originating from stream water (S-NO_3), and nitrate originating from the groundwater (G-NO_3). Reactions are simulated using Monod-kinetics, parameterized similarly to the reactive transport modeling of Trauth et al. [2014]. In Monod-kinetics, denitrification is inhibited by the presence of O_2 and, hence, significant NO_3 consumption occurs only under anaerobic conditions.

Constant concentrations for the chemical boundary conditions at the streambed and the lateral upstream boundary are defined by a Dirichlet type boundary condition. We assumed constant stream water solute concentrations for all scenarios. As determined by the analysis of water samples (see section 4.2.1), concentrations of 0.31 mmol/L (10 mg/L) dissolved O_2 and 0.26 mmol/L (10 mg/L) NO_3 are assigned to the chemical streambed boundary. We assume that DOC does not limit the reactions, and use a concentration of 0.26 mmol/L (18.66 mg/L) CH_2O (twice the molar mass of the O_2). We base this assumption on the fact that particulate organic

Table 4.1: Parameterization of the Reactive Transport Model MIN3P

Parameter	Value
Water flow and solute transport	
Hydraulic conductivity K, x-y direction [m/s]	5.96×10^{-3}
Hydraulic conductivity K, z direction [m/s]	4.47×10^{-4}
Porosity [-]	0.3
Longitudinal dispersivity [m]	0.1
Transversal horizontal dispersivity [m]	0.01
Transversal vertical dispersivity [m]	0.001
Diffusion coefficient, aqueous phase (saturated zone) [m^2/s]	1×10^{-9}
Diffusion coefficient, gaseous phase (unsaturated zone) [m^2/s]	1×10^{-5}
van Genuchten – α [m^-1]	2
van Genuchten – n [-]	1.5
Parameterization of Monod kinetics for solute reactions	
Half-saturation constant K_{O_2} [mmol/L]	6.25×10^{-3}
Half-saturation constant K_{NO_3} [mmol/L]	3.23×10^{-2}
Half-saturation constant K_{DOC} [mmol/L]	1.07×10^{-1}
Inhibition constant for denitrification K_I [mmol/L O_2]	3.13×10^{-2}
maximum reaction rate of aerobic respiration $\mu_{max,AR}$ [mmol/L/d]	4.78×10^{-1}
maximum reaction rate of denitrification $\mu_{max,DN}$ [mmol/L/d]	8.64×10^{-2}

Solute concentrations at model boundaries		
	Streambed boundary	Lateral upstream boundary
O_2 [mmol/L]	0.31	0.0781
DOC (CH_2O) [mmol/L]	0.62	0
NO_3 [mmol/L]	0.161 (as S-NO_3)	1.61 (as G-NO_3)

matter can represent an additional carbon source within the shallow streambed sediments in addition to DOC in stream water [Pusch, 1996; Brunke and Gonser, 1997; Brugger et al., 2001]. Solute concentrations at the lateral upstream boundary, representing the ambient groundwater, are set to 0.078 mmol/L (2.5 mg/L) dissolved O_2 and 1.61 mmol/L (100 mg/L) G-NO_3. Although low concentrations of DOC (< 2 mg/L) are present in the groundwater, we assume that this DOC does not consist of easily biodegradable (labile) carbon [Kaplan and Newbold, 2000; Benner, 2003] and is not utilized by denitrifying bacteria, as indicated by the very high nitrate concentrations in ambient groundwater. Therefore, concentrations of 0 mmol/L CH_2O is assigned to the lateral upstream boundary.

The values used for the parameterization of the reactive transport groundwater model are listed in Table 4.1 and are explained in detail in Trauth et al. [2014], where the same modeling protocol was used.

4.2.4 Test of the CFD and Subsurface Flow Model

Stream stage and discharge from the CFD simulations are compared against the rating curve developed from discharge measurements at the field site (Figure 4.2a). Overall, the simulated stream stages and discharges fit the observed power function rating curve well, with a $R^2 > 98\,\%$. This confirms the physical correctness of the stream water CFD simulations and the resulting hydraulic head distribution at the streambed, which is subsequently coupled to the groundwater model.

To calibrate the groundwater model we compare residence times calculated from electrical conductivity (EC) time series, measured in the sediment of the ISGB, against simulated residence times. When stream water infiltrates into the streambed EC fluctuations in the stream propagate into the subsurface with a specific time lag. By cross-correlating EC time series in the stream and streambed, the peak residence times for water infiltrating from the stream and flowing to the subsurface can be estimated. EC-based residence times are calculated in this manner using EC-time series measurements from the stream and in 10 mini-piezometers distributed across the ISGB at depths of 0.44 m below the streambed surface. These EC-time series were measured over a period of relatively constant stream discharge of $1.7\,\mathrm{m}^3/\mathrm{s}$.

To simulate residence times we parameterize our modeling approach according to the same stream discharge of $1.7\,\mathrm{m}^3/\mathrm{s}$ and the groundwater heads observed in the wells at the stream bank of the field site. Residence times are simulated using backward particle tracking starting at the 10 mini-piezometers. By adjusting the hydraulic conductivity in both the lateral and vertical direction, an optimal fit with the observed residence times is found for hydraulic conductivities of 5.96×10^{-3} m/s in x and y direction and 4.47×10^{-4} m/s in vertical (z) direction. Thus, the

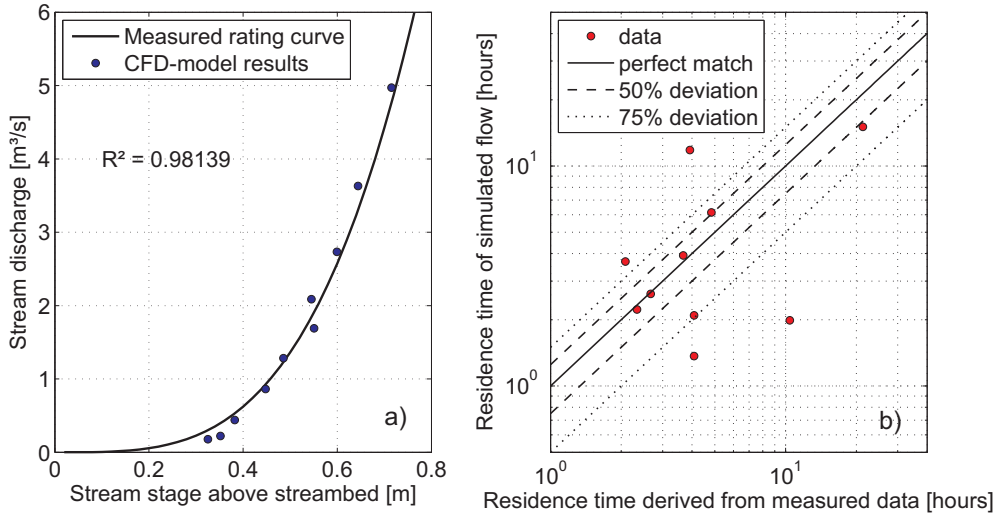

Figure 4.2: a) Measured and modeled stage-discharge relationship b) Residence times derived from measured electrical conductivity data by cross-correlation versus residence times of flow simulations for stream discharge of $1.7\,\mathrm{m}^3/\mathrm{s}$.

anisotropy ratio between lateral and vertical hydraulic conductivity was inferred to be on the order of 13. This relatively high anisotropy ratio can be explained by the strong preferential orientation of ellipsoidal, flat gravels and cobble stones in the direction of flow (imbrication), as have been observed at the streambed surface and in freeze cores of the streambed sediments. Similar and even higher anisotropic ratios have been reported for alluvial aquifers by Yager

[1993], Chen and Chen [2003] and Cheng and Chen [2007].
Both the shortest and longest EC-based calculations of residence times agree with the simulated residence times indicating that the model adequately represents the entire range of real world hyporheic residence times (Figure 4.2b). Discrepancies between the simulated and calculated residence times could originate from small-scale heterogeneities in hydraulic conductivity and porosity, which are not represented in our model.

4.3 Results

4.3.1 Stream Flow and Hydraulic Heads at the ISGB

Below discharges of $3.63\,\mathrm{m}^3/\mathrm{s}$, the ISGB is not fully submerged and the stream splits into a primary and secondary flow channel (left and right channel in flow direction in Figures 4.3a–4.3c and 4.4a). Downstream of the ISGB the two channels merge again to form one single stream channel. The length to width ratio of the submerged parts of the ISGB increases with stream discharge from 3.1 to 3.8, with an average ratio of 3.4. These ratios are in line with those of naturally occurring fluvial islands surveyed by Wyrick [2005].
The CFD model calculates the hydraulic head distribution at the streambed as shown in Figures 4.3d–4.3f. The longitudinal (parallel to stream flow) component of the hydraulic gradient is evaluated between two points up- and downstream of the gravel bar ("Up" and "Down" in Figures 4.3d–4.3f); subsequently referred to as ∇H_{Long}. Similarly a lateral component of the head gradient (∇H_{Lat}) perpendicular to the general stream flow direction is calculated between the points "Prime" and "Second" in Figures 4.3d–4.3f). Both gradients decrease with increasing stream discharge (Figure 4.4b), reaching a minima when the ISGB is inundated. During lower discharges ($< 1.2\,\mathrm{m}^3/\mathrm{s}$), lateral hydraulic head gradients predominate longitudinal gradients ($\nabla H_{Lat} > \nabla H_{Long}$). The strong lateral gradients across the ISGB under these flow conditions are caused by a non-uniform decline in hydraulic heads along the two stream channels, induced by diagonally opposed riffles, such as in Figure 8c in Wondzell and Gooseff [2013]. At the entry to the primary channel a riffle induces a drop in the hydraulic heads in the primary channel, producing a slope of 3–4 %. In contrast, in the secondary channel a riffle occurs toward the end of the channel, accompanied by a drop in hydraulic head of a similar slope. This effect is most pronounced under low discharge conditions ($0.18\,\mathrm{m}^3/\mathrm{s}$), when the maximum difference in hydraulic heads occurs between the two channels. When the ISGB is largely or completely submerged lateral variations of the hydraulic gradients are comparatively minor. However, at high discharges surface waves induce variations in the hydraulic head distribution and local variations in the longitudinal hydraulic head gradient.

4.3.2 Subsurface Flow Field and Hyporheic Exchange

The interplay between the hydraulic head distributions at the streambed and the up- and downstream hydraulic boundary conditions in the groundwater model induce four general types of flow paths in the subsurface. These flow paths can be distinguished by their entry points into and exit points out of the subsurface modeling domain.

1. Hyporheic flow paths: stream water enters and leaves the modeling domain across the streambed. These flow paths define what we call hyporheic exchange flux (HEF). Stream

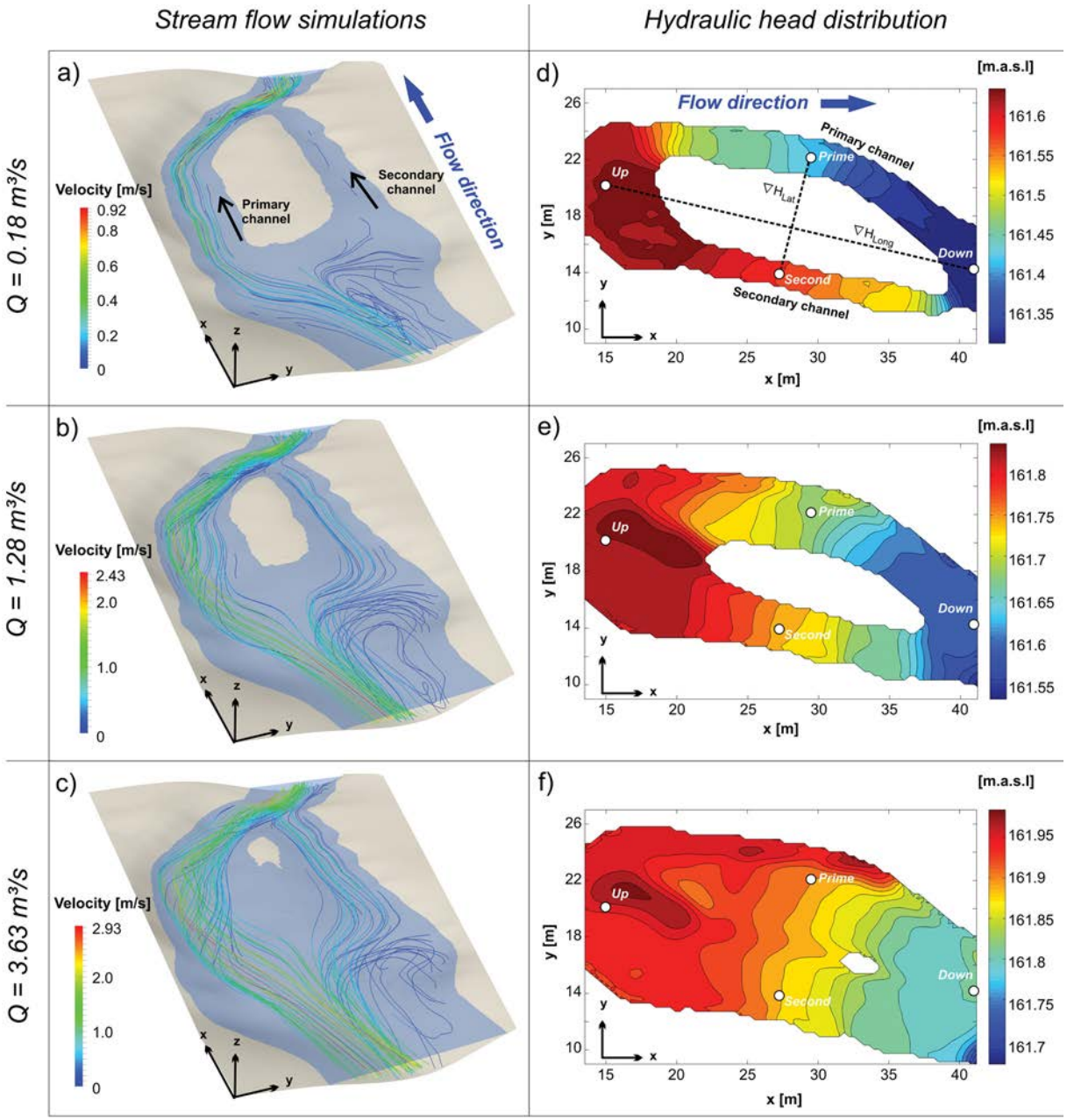

Figure 4.3: CFD simulations of low, moderate and high stream discharge scenarios and resulting hydraulic head distribution at the streambed. a–c) Water level surrounding the ISGB and stream lines represent flow velocity. d–f) Corresponding hydraulic heads at the streambed. Please note the four locations "Up", "Down", "Prime", "Second" used for calculation of longitudinal and lateral head gradients ∇H_{Long} and ∇H_{Lat} along the dashed lines in d).

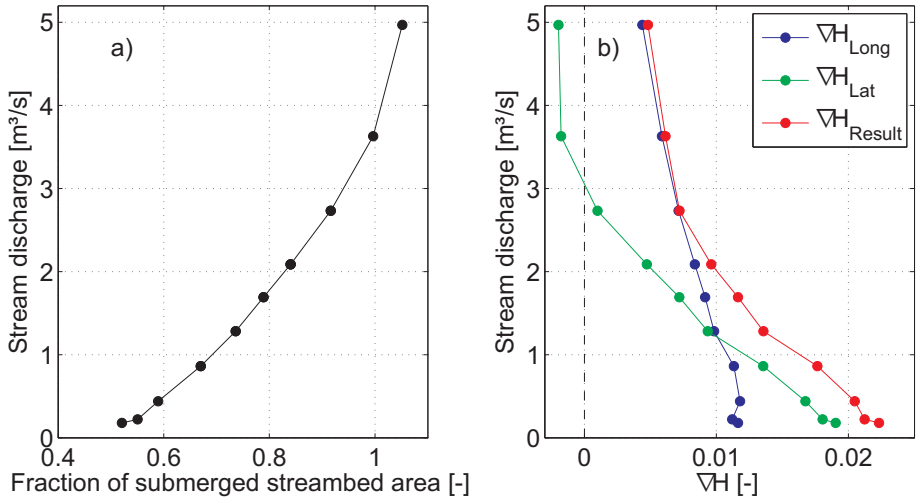

Figure 4.4: a) Stream discharge versus submerged streambed area. Streambed area is normalized to the streambed area at Q = 3.6 m^3/s, where the ISGB is completely inundated. Higher discharges inundate the channel boundaries toward the stream banks. b) Stream discharge versus hydraulic head gradients between the secondary and the primary channel (blue), upstream and downstream ends of the ISGB (green), and the resulting gradient (red). Gradients are calculated by using hydraulic heads of the locations "Up", "Down", "Prime", "Second" , as shown in Figure 4.3d.

water infiltrates mainly in the secondary channel and exfiltrates into the primary channel, forming a hyporheic flow cell with characteristic depth and width (dark and light blue markers in Figures 4.5a–4.5e).

2. Losing flow paths: stream water infiltrates into the subsurface domain through the streambed and leaves it via the downstream lateral boundary (red markers in Figures 4.5a–4.5e).

3. Gaining flow paths: groundwater enters the subsurface domain at the upstream lateral boundary and exfiltrates through the streambed (green markers in Figures 4.5a–4.5e).

4. Underflow: groundwater enters the subsurface domain at the upstream lateral boundary and exits at the lateral downstream boundary. These flow paths do not interact with the streambed but are present in all scenarios.

Figures 4.5a–4.5e shows the infiltrating and exfiltrating locations on the streambed surface for the different flow path types (#1 to #3 from above) under low, moderate and high stream discharge conditions, as well as for neutral, losing and gaining conditions. The occurrence and frequency of these flow path types depend primarily on the hydraulic head distribution at the streambed and secondarily on the direction and magnitude of surface water-groundwater exchange. To quantify the latter, we denote Δh as the difference between the ambient groundwater heads at the center of the ISGB and the mean of the hydraulic head distribution at the streambed. In general, positive Δh values indicate net gaining conditions (groundwater upwelling), while negative Δh values indicate net losing conditions (stream water downwelling). When $\Delta h = 0$ m the ambient groundwater heads and the average hydraulic heads at the streambed are balanced (neutral conditions). Even under neutral conditions both locally gaining and losing flow paths can occur due to local variations in streambed morphology and the resulting near-bed pressures (see Figures 4.5a–4.5c).

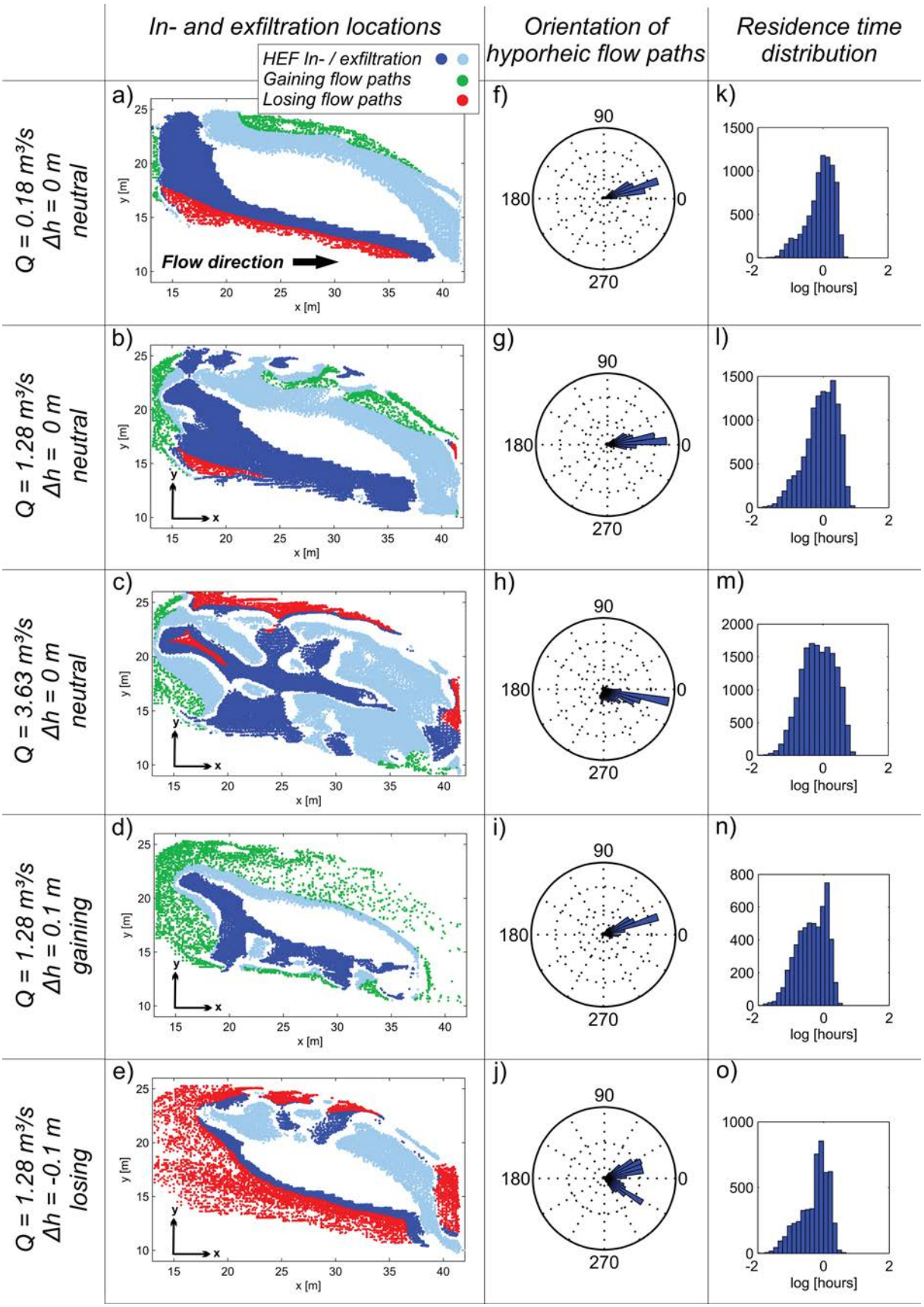

Figure 4.5: a–e) Infiltration and exfiltration locations at the streambed for hyporheic flow paths (infiltration: dark blue, exfiltration: light blue), gaining flow paths (green), and losing flow paths (red). Low, moderate and high stream discharges (a–c) under neutral conditions ($\Delta h = 0\,\mathrm{m}$) and gaining and losing conditions (d and e) for constant stream discharge. f–j) Orientation of hyporheic flow paths. An orientation of 0° refers to the positive x-direction, 90° refers to positive y-direction. k–o) Residence time distributions for hyporheic flow paths. The x-scale is logarithmic.

4.3.2.1 Effects of Hydraulic Head Distribution at the Streambed

The hydraulic head distribution at the streambed surrounding the ISGB induces a hyporheic flow field where stream water generally infiltrates in the secondary stream channel and flows towards the primary stream channel. These flow paths span the hyporheic flow cell. The hydraulic head distribution and, thus, the lateral and longitudinal hydraulic gradients, vary with the stream discharge (see section 4.3.1). As a result, the direction of the hyporheic flow paths also changes significantly with stream discharge. Under low stream discharge conditions, when $\nabla H_{Lat} > \nabla H_{Long}$, the bulk of the flow paths are directed from the secondary towards the primary stream channel with a mean angle of 25° to 45° relative to the x-direction (0°). With increasing stream discharge, the mean direction of the flow paths rotates in the clockwise direction to an angle between 0° and 310°, representing mainly longitudinal flow paths oriented in the direction of stream flow (Figure 4.5f–4.5h). Higher discharges lead to higher variance in flow direction, indicating that the hyporheic flow paths are highly non-uniform in direction. This effect is most pronounced for high discharge where ∇H_{Lat} is very small compared to ∇H_{Long} (Figure 4.4b). However, ∇H_{Long} is not constant across the streambed of the inundated ISGB, because local variations in the stream water level induce near-bed pressure variations. The directions of the hyporheic flow path deviate from exclusively longitudinal flow and, hence, scatter within a range of up to 180°.

Residence times (RTs) of the hyporheic flow paths are generally log-normally distributed (Figure 4.5k–4.5o) with median RTs of up 8.3 hours. We observed a decreasing negative skewness of the log-normal distribution with increasing stream discharge (Figure 4.5k–4.5m). In the inundated ISGB scenarios, the log-normal distributions tend to be symmetric (Figure 4.5m). A strongly negative skewness represents a lower frequency of hyporheic flow paths with short RTs. This low frequency is due to the fact that under low discharge conditions no additional, separated, small hyporheic flow cells exist. Rather, at low discharge the majority of the hyporheic flow paths span the full longer distance from the secondary channel to the primary channel, forming a single hyporheic flow cell with relatively long RTs. Furthermore, standard deviations of the RTD are smaller under low discharge condition which is a result of relatively similar flow paths length and spatial orientation leading to a higher uniformity of the hyporheic flow field.

As shown above, stream discharge and, in turn, hydraulic head distribution at the streambed, control hyporheic flow path orientation and residence time distribution. Similarly, the magnitude of the hyporheic exchange flux (HEF), the extent of the hyporheic flow cells, and the median residence times of those cells are controlled by the hydraulic head distribution. These effects are most visible during neutral conditions ($\Delta h = 0\,\mathrm{m}$), when the impact of ambient groundwater flow conditions on hyporheic exchange is the lowest.

We observe three characteristic hyporheic flow regimes for stream discharges of $< 1.2\,\mathrm{m^3/s}$, 1.2 to $3.6\,\mathrm{m^3/s}$ and $> 3.6\,\mathrm{m^3/s}$ (indicated by roman numerals I, II, III in Figure 4.6).

I. At discharges lower than $1.2\,\mathrm{m^3/s}$, when the lateral gradient predominates over the longitudinal gradient ($\nabla H_{Lat} > \nabla H_{Long}$), the HEF is large (Figure 4.6a), the volumetric size of the hyporheic flow cell is small (Figure 4.6b) but extends relatively deep into the aquifer (Figure 4.6c), and median RTs are long (Figure 4.6d).

II. Between discharges of 1.2 and $3.6\,\mathrm{m^3/s}$ the hydraulic gradients shift, such that $\nabla H_{Lat} <$

∇H_{Long}. Under these conditions, the HEF is small and accompanied by a large but shallow hyporheic flow cell, leading to shorter median RTs compared to hyporheic flow regime I (Figure 4.6).

III. At discharges that inundate the ISGB ($Q > 3.6\,m^3/s$), the lateral gradient is absent and hyporheic exchange is exclusively driven by the longitudinal gradient. The HEF is high, hyporheic flow cell extent is even larger than in II and the shortest median RTs occur (Figure 4.6).

4.3.2.2 Effects of Neutral, Losing and Gaining Conditions

The in- and exfiltration patterns of hyporheic, losing and gaining flow paths (see list in 4.3.2) at the streambed differ between neutral, losing and gaining conditions (Figure 4.5b–4.5e). Under neutral conditions, the zones of hyporheic flow path in- and exfiltration are the largest, comprising up to 90 % of the wetted streambed area. With increasing magnitude of Δh (in both the losing and gaining scenarios), these zones decrease exponentially until Δh of ± 0.1 m, when approximately 60 % of the hyporheic flow paths transition to losing or gaining flow paths.

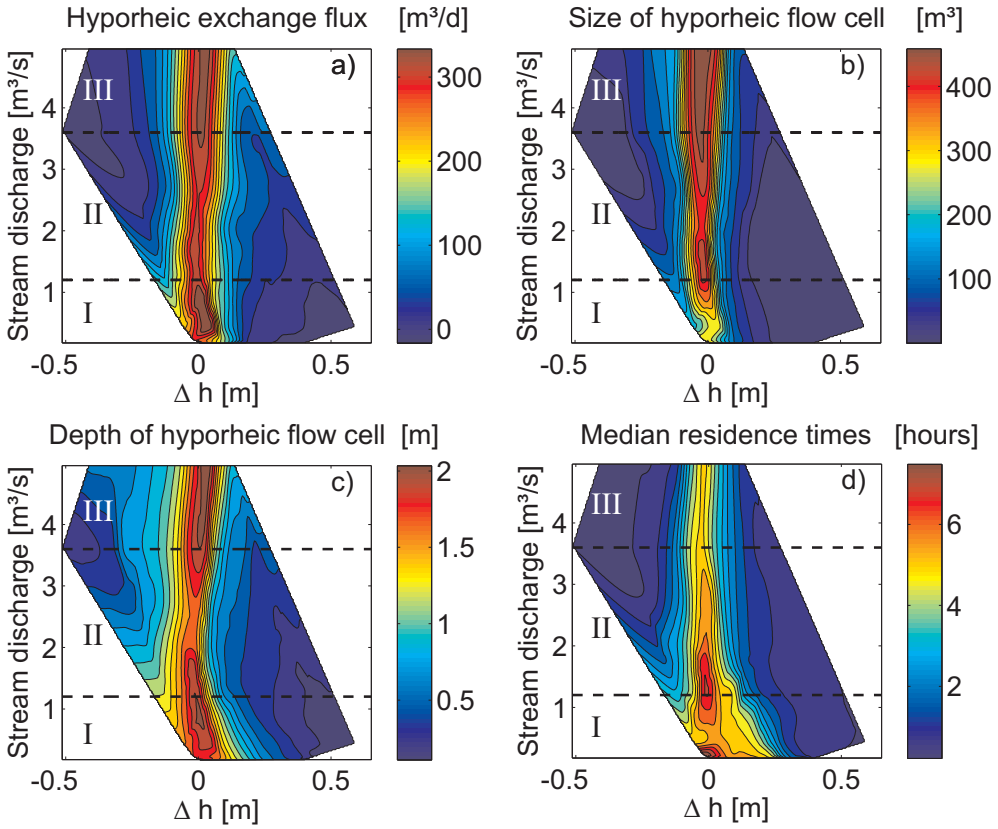

Figure 4.6: a) Hyporheic exchange flux, b) volumetric size of the hyporheic flow cell in the subsurface, c) maximum depth of the hyporheic flow cell below the maximum ISGB elevation (161.9 m.a.sl.), and d) median residence times of the hyporheic flow paths in relation to stream discharge and Δh. The roman numbers (I, II, III) refer to the three hyporheic flow regimes described in section 4.3.2.1.

Under losing conditions, the hyporheic flow paths infiltrate in a very narrow zone along the secondary channel, adjacent to the non-submerged areas of the ISGB, and exfiltrate over a much broader area along the primary channel. Additional small hyporheic flow cells occur, representing hyporheic exchange within the primary channel (Figure 4.5e). In contrast, under gaining conditions the hyporheic flow paths infiltrate through a broad area along the secondary

channel and exfiltrate in a narrow zone along the streambed of the primary channel. Opposite to the losing conditions, additional small hyporheic flow cells occur in the secondary channel (Figure 4.5d).

In addition to the strong impact losing and gaining conditions have on the spatial distribution of in- and exfiltrating zones, the size and extent of the hyporheic flow cells and the median RTs decrease exponentially with increasing magnitude of Δh. For a Δh of ± 0.1 m the size, extent and median RT of the flow cells decrease to at least 50 % of the values of the neutral case (Figure 4.6). Under gaining conditions, increasing flow along the gaining flow paths (flow path type #3 in section 4.3.2) decreases the extent of the hyporheic flow cells and the magnitude of HEF and median hyporheic RTs. Under losing conditions, infiltrating stream water is divided into hyporheic flow paths and losing flow paths (flow path types #1 and #2 in section 4.3.2). The stronger the losing conditions (i.e. the smaller Δh becomes), the higher the losing flux and the smaller the HEF (Figure 4.6a). Similar to the gaining case, the hyporheic flow cells in the losing case become smaller and shallower, resulting in shorter median RTs (Figure 4.6a–4.6d). Consequently, the highest HEF, largest hyporheic flow cell extent, and longest median RTs can be observed under neutral conditions ($\Delta h = 0$ m), where ambient groundwater heads and hydraulic heads are balanced. Under these conditions, losing and gaining fluxes are comparably small and their subsequent effect on hyporheic exchange is the lowest.

4.3.3 Solute Transport and Reactions in the Subsurface

Figure 4.7 shows the spatial distribution of solute reactions along longitudinal and lateral cross-sections of the ISGB for different discharges under neutral (Figures 4.7a–4.7c), gaining (Figure 4.7d) and losing conditions (Figure 4.7e). To quantify solute fluxes and reaction rates induced by a singular morphological streambed structure, like a ISGB, only solute transport and reactions along the hyporheic flow paths (flow path #1 in section 4.3.2), that both infiltrate and exfiltrate across the streambed, are considered and described in the following section. Solute transport and reactions outside the hyporheic flow cells, i.e. along losing and gaining flow paths are described in section 4.3.3.2. To be more comparable with other studies, solute influx and consumption are normalized to the total streambed area at the ISGB of 300 m^2 (30 m $\times$ 10 m) for all discharge scenarios, independent of the level of submergence.

4.3.3.1 Solute Transport and Reactions Along Hyporheic Flow Paths

Under neutral conditions ($\Delta h = 0$ m) the influx of O_2 along the hyporheic flow paths is at a maximum, as is the HEF (Figure 4.8a). Infiltrating O_2 creates large aerobic zones in the subsurface where aerobic respiration occurs. Consequently, O_2 consumption is highest with up to < 133 mmol/m^2/d in the largest hyporheic flow cells, occurring in the neutral case when Δh magnitudes are small (Figure 4.8b). The O_2 consumed as a fraction of the total O_2 influx (FO_2) is at a maximum with 42 % (Figure 4.8c). When the magnitude of Δh increases in either the negative or positive direction (losing or gaining, respectively), the size of the hyporheic flow cells and the influx of O_2 decrease (Figure 4.8a). As a result, reactive areas for aerobic respiration within the hyporheic flow cell decrease, RTs are shorter, and O_2 consumption decreases (Figure 4.8b). Likewise, the consumed fraction of O_2 influx (F_{O2}) decreases with increasing magnitude of Δh, indicating a simultaneous decrease in O_2 consumption with O_2 influx. O_2 consumption

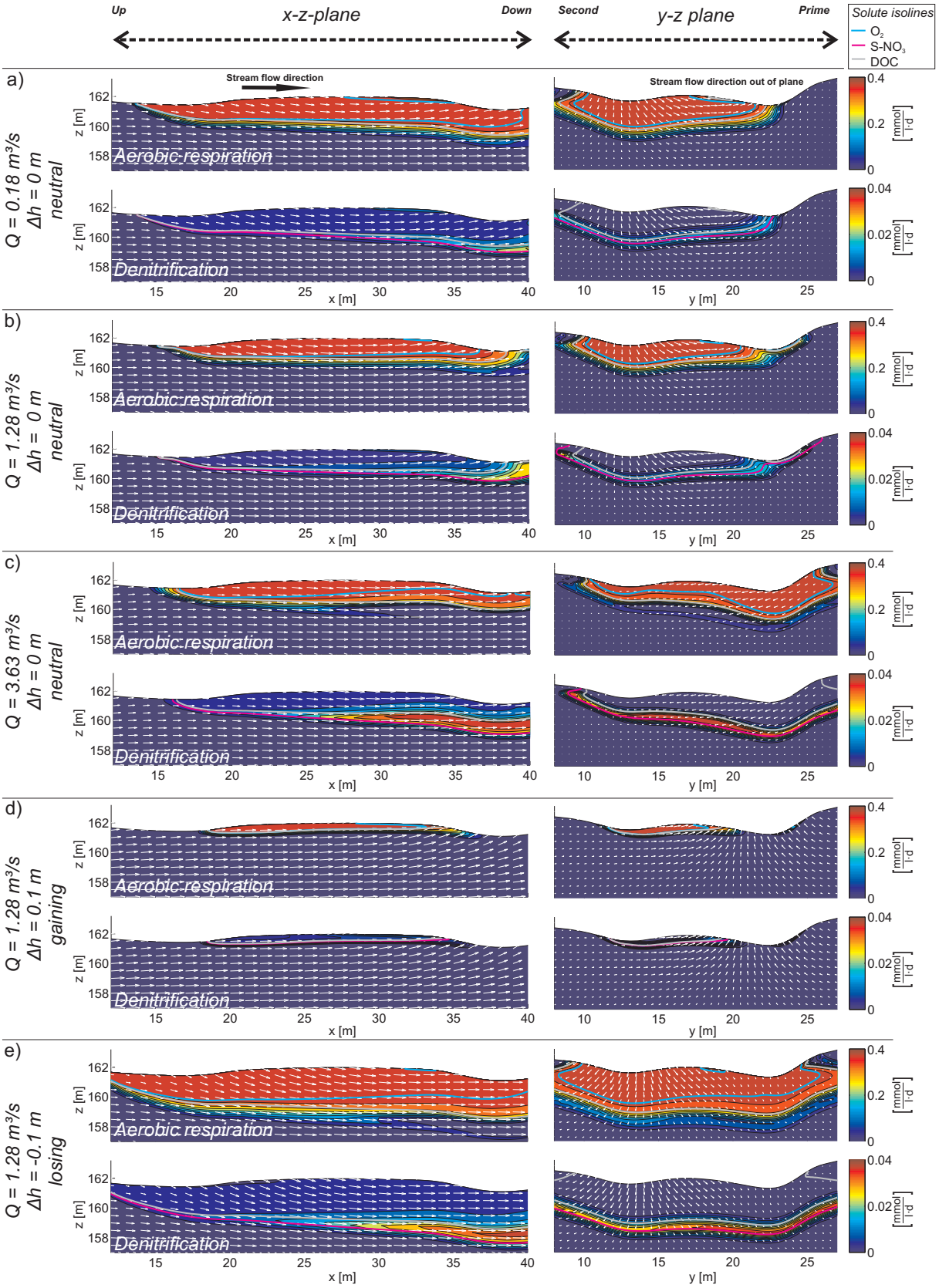

Figure 4.7: Cross-sections showing (top row) aerobic respiration and (bottom row) denitrification rates of stream water borne nitrate along the x-z-plane and y-z-plane between the locations "Up", "Down", "Prime", "Second" shown in Figure 4.3d. The scenarios and their order correspond to those of Figure 4.5: neutral conditions under (a) low, (b) moderate and (c) high discharges; (b) neutral, (d) gaining, and (e) losing conditions for constant discharge. The white arrows depict subsurface flow vectors (direction and magnitude), based on x-z velocity and y-z velocity components, respectively. Cyan, magenta and grey lines represent isolines for half of the maximum solute concentrations of O_2, S-NO_3 and DOC (CH_2O), respectively.

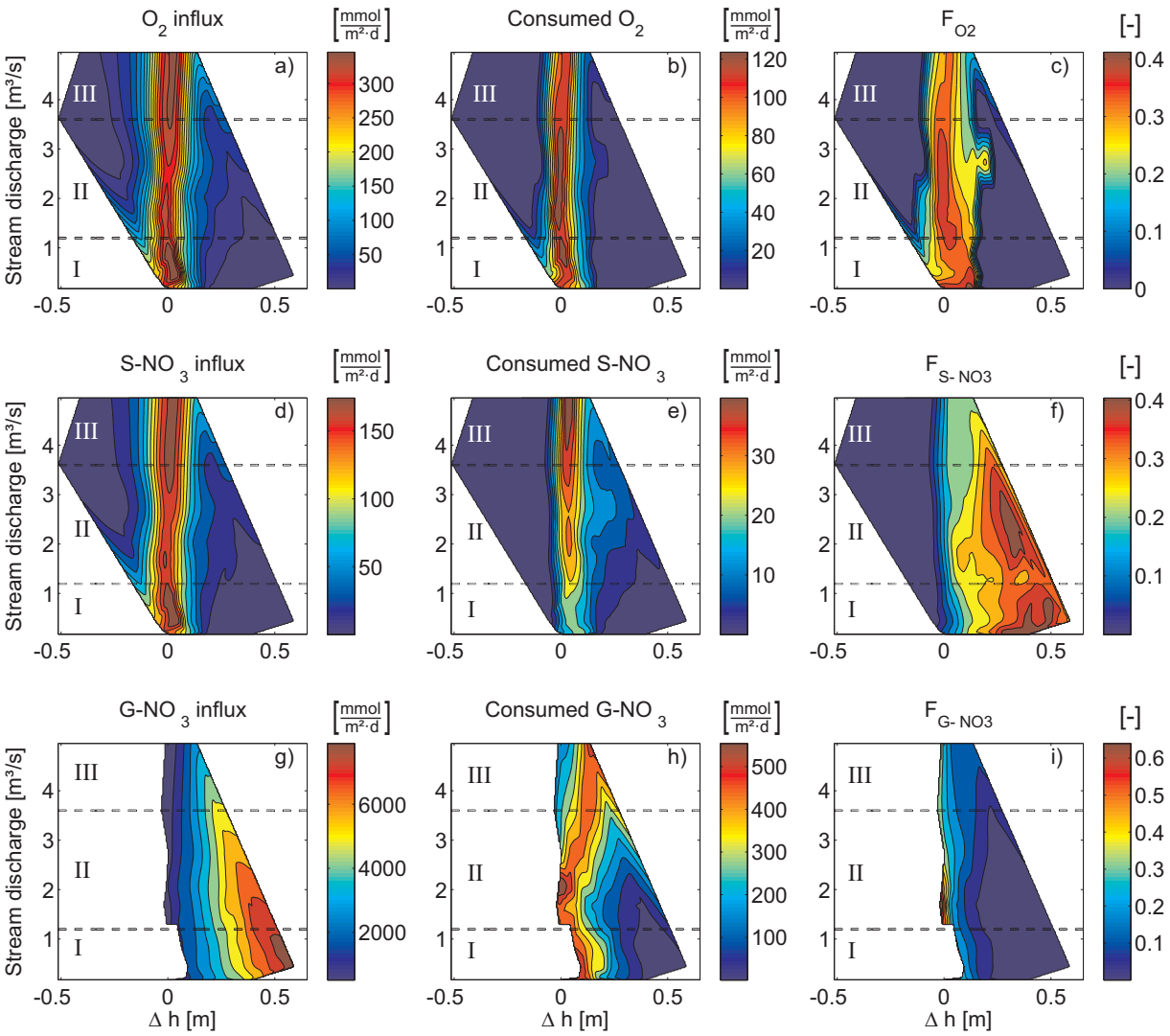

Figure 4.8: a) O_2 influx, b) consumed O_2, and c) consumed O_2 as a fraction of influx (F_{O2}) in relation to stream discharge and Δh, d) Stream water nitrate influx (S-NO_3), e) consumed S-NO_3, and f) consumed S-NO_3 as a fraction of influx ($F_{S\text{-}NO3}$) in relation to stream discharge and Δh, g) Influx of groundwater borne nitrate (G-NO_3), h) consumed G-NO_3, and i) consumed G-NO_3 as a fraction of G-NO_3 influx ($F_{G\text{-}NO3}$) in relation to stream discharge and Δh. Solute influx and consumed solutes are normalized to a streambed area of 300 m^2. The roman numbers (I, II, III) refer to the three hyporheic flow regimes described in section 4.3.2.1.

and F_{O2} decrease exponentially with increasing magnitude of Δh under both losing and gaining conditions. At $\Delta h = \pm 0.1$ m O_2 consumption and F_{O2} are only 30 % and 72 %, respectively, of the maximum values under neutral conditions. O_2 consumption and F_{O2} vary slightly with stream discharge, as is most pronounced under neutral conditions. The highest O_2 consumption and F_{O2} occur when discharge is smaller than 3.6 m^3/s (Figures 4.8b and 4.8c), as represented by hyporheic flow regimes I and II. Under these conditions long flow paths and long residence times occur (Figure 4.6d). In flow regime III, when the ISGB is completely submerged ($Q > 3.6\,m^3/s$), O_2 consumption is lower, because many separate longitudinally oriented smaller hyporheic flow cells with shorter RT occur allowing less time for aerobic respiration to take place.

Similar to the O_2 influx, the highest S-NO_3 influx and consumption by denitrification occurs under neutral groundwater conditions, when magnitudes of Δh are low (Figure 4.8d). Under these conditions, denitrification of S-NO_3 increases with stream discharge, inverse to O_2 consumption, with the maximum S-NO_3 denitrification, up to 40 $mmol/m^2/d$, being observed at the highest

stream discharges (Figure 4.8e). This effect can be explained by the increasing extent of the hyporheic flow cell with increasing stream discharge (Figures 4.6b and 4.8e) leading to larger reactive areas where the conditions for denitrification are met (depleted O_2, available DOC). In the gaining and neutral cases, the conditions for denitrification are met only in a narrow zone surrounding the aerobic zone, as a "reactive fringe" at the border of the hyporheic flow cell (Figures 4.7a–4.7d). The size of this reactive fringe is controlled by the size of the hyporheic flow cell and increases when the hyporheic flow cell size increases. The stronger the gaining conditions, the smaller the extent of the hyporheic flow cell and the reactive fringe and, as a result, the consumption of S-NO_3 by denitrification. This amount decreases exponentially with increasing Δh and is at 60 % of the value of the neutral case at $\Delta h = +0.1$ m (Figure 4.8e). The denitrified fraction of S-NO_3 influx ($F_{S\text{-}NO3}$) is highest under gaining conditions with fractions of up to 40 % (Figure 4.8f).

In the losing case, denitrification is not restricted to the hyporheic flow cell extent and, rather, is present everywhere where O_2 is significantly depleted and DOC is still available. Consequently, S-NO_3 denitrification does not occur solely along hyporheic flow paths but also along infiltrating flow paths, regardless of whether they return to the stream (hyporheic) or not (losing). This effect reflects the different hydraulic conditions driving S-NO_3 denitrification under losing and gaining conditions. Under losing conditions, the exponential decrease in S-NO_3 denitrification with decreasing Δh is significantly steeper, and only 1 % of the value of the neutral case of S-NO_3 consumption is denitrified at $\Delta h = -0.1$ m. This steeper decline in denitrification under losing conditions reflects the fact that S-NO_3 denitrification occurs mainly along the losing flow paths (flow paths #2 in section 4.3.2) that contribute flow to the ambient groundwater system (Figure 4.7e) (see detailed explanation in next section 4.3.3.2). Hence, S-NO_3 that circulates within the hyporheic flow cell, which is mainly oxic, exfiltrates back to the stream untransformed to large portions and, thus does not contribute to net stream nitrate consumption.

4.3.3.2 Solute Transport and Reactions Along Losing and Gaining Flow Paths

Under losing conditions, a fraction of the infiltrating stream solutes is transported outside the hyporheic flow cell toward the downstream model boundary, along the losing flow paths. While O_2 is primarily consumed in the vicinity of the ISGB (Figure 4.7e), DOC and S-NO_3 are still present downstream of the ISGB toward the downstream model boundary (magenta and gray isoline in Figure 4.7e). Here, these solutes likely undergo further reactive processing. However, the products of this processing do not return to the surface water by way of hyporheic exchange through the ISGB and are therefore not considered in our evaluation. The magnitude of reactive processing not considered is highest under strongly losing conditions ($\Delta h < 0$ m), when a large fraction of the S-NO_3 denitrification zones are located outside the hyporheic flow cell (Figure 4.7e).

Under gaining conditions ($\Delta h > 0$ m), groundwater-borne nitrate (G-NO_3) and low concentrations of groundwater-borne O_2 enter the modeling domain at the upstream boundary. A portion of these groundwater solutes is transported toward the ISGB following the gaining flow paths (shown in Figure 4.8g) while the remainder flows straight toward the downstream model boundary as underflow (data not shown). G-NO_3 can be denitrified only in the vicinity of the ISGB, where stream-sourced DOC is present and O_2 is significantly depleted. These conditions for

denitrification are met beneath the aerobic zone of the hyporheic flow cell, and thus G-NO_3 is denitrified in a reactive fringe similar to S-NO_3. The higher the magnitude of the gaining Δh, the higher the influx of G-NO_3 along the gaining flow paths flowing towards the ISGB (Figure 4.8g). The highest total consumption of G-NO_3 can be observed under neutral and slightly gaining conditions (Figure 4.8h). Similarly, the fraction of G-NO_3 influx consumed ($F_{G\text{-}NO3}$) decreases with increasing magnitude of Δh (Figure 4.8h). Hence, highest fractions of solute influx consumed are observed at the lowest Δh and at relatively low stream discharges, where the total influx of solutes is low but consumption of G-NO_3 is high. Under these conditions, the size of the hyporheic flow cell is large, as is the resulting reactive fringe where DOC from the stream and G-NO_3 can mix.

4.4 Discussion

4.4.1 Characteristics and Relevance of Hyporheic Exchange and Reactions in In-Stream Gravel Bars

Hyporheic exchange occurs over the full scale range of morphological structure, from dunes to meanders to the catchment scale [Cardenas, 2008; Stonedahl et al., 2010; Boano et al., 2014]. HEF through submerged streambed structures, like dunes and riffles, increases with increasing discharge [Packman et al., 2004; Cardenas and Wilson, 2007a; Trauth et al., 2013; Fox et al., 2014]. In contrast, HEF through partially submerged structures decreases with increasing discharge, as observed by Shope et al. [2012], Schmidt et al. [2012] and this study (see section 4.3.2.1). This is caused by the different mechanisms that affect the controlling hydraulic head gradients. Hydraulic head gradients along the streambed of submerged bedforms are the result of pressure differences between the upstream and downstream sides of these structures, induced by strong water level variations and local changes in velocity head related to hydraulic jumps, surface waves and eddies. With increasing stream discharge these hydraulic effects become increasingly important resulting in more pronounced pressure (hydraulic head) variations across the streambed [Elliott and Brooks, 1997b; Tonina and Buffington, 2007]. In contrast, hydraulic head gradients across partially submerged structures, such as ISGBs, are not as strongly related to eddies and surface water waves, but to water level differences between the channels surrounding the ISGB (section 4.3.1). With increasing discharge and water level, hydraulic heads in the two channels begin to equilibrate, thus, hydraulic head gradients across the ISGB and HEF decrease. The minimum HEF in our simulation is reached at a stream discharge of approximately 2.7 m^3/s, where about 90 % of the ISGB area is submerged (Figure 4.6a).
Comparing normalized HEF of the ISGB with that of submerged pool-riffle morphologies, HEF through submerged pool-riffle morphologies is 6 times higher than through the ISGB (calculated as the average HEF in the neutral cases for the non-submerged ISGB scenarios and pool-riffle morphology A05 from Trauth et al. [2013]; HEF is normalized by dividing with the geometric mean of lateral and vertical hydraulic conductivities and infiltration areas of hyporheic exchange). To quantify the overall potential of stream water movement through a bedform structure, the ratio between HEF and stream discharge is a useful metric. The HEF:discharge ratios for our non-submerged ISGB are on the order of 0.1 - 2 %, and decrease with increasing discharge and increasing magnitude of losing and gaining conditions. Thus, the HEF:discharge ratio is at a

maximum in hyporheic flow regime I, under neutral conditions, where highest HEF and lowest discharge occur (Figure 4.6a). Compared to a fully submerged ISGB or submerged pool-riffle morphologies these fractions are up to 2 orders of magnitudes higher [Trauth et al., 2013]. This suggests that significantly higher hyporheic exchange rates can occur in partially submerged bedforms, in particular under low stream discharge conditions.

Hyporheic residence time is a useful metric to assess the reactive potential of hyporheic zones, since the longer the residence time, the higher the potential for solute transformation [Jones and Holmes, 1996; Boano et al., 2010; Zarnetske et al., 2011a]. Our results show that the consumption of solutes is positively correlated with the median RTs of the hyporheic flow paths (Figure 4.9a). The RTs are, in turn, related to the size and the extent of the hyporheic flow cell. With decreasing

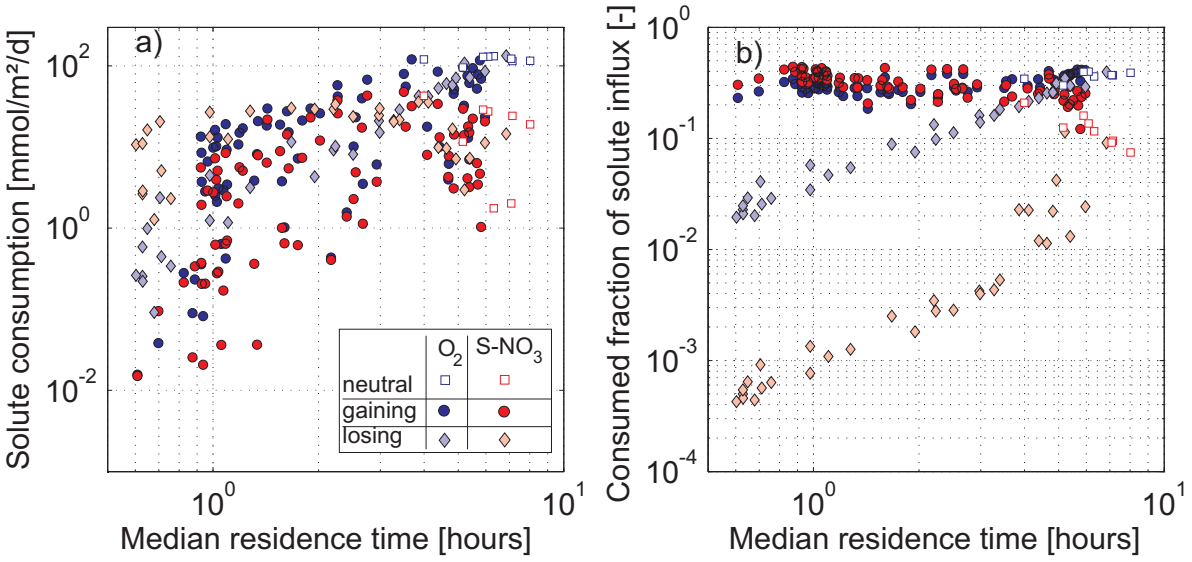

Figure 4.9: Median residence times of hyporheic flow paths versus a) consumed solutes per streambed area, and b) consumed fraction of solute influx (F_{O2} and $F_{S\text{-}NO3}$). Neutral conditions are defined as $-0.02\,\mathrm{m} > \Delta h < +0.02\,\mathrm{m}$. Gaining and losing conditions are defined as $\Delta h > +0.02\,\mathrm{m}$ and $\Delta h < -0.02\,\mathrm{m}$, respectively.

size of the hyporheic flow cell the RT shortens and the size of the reactive zones shrinks, which further reduces solute consumption. Similarly, the fraction of the solute influx consumed in the reactive zones (F_{O2} and $F_{S\text{-}NO3}$) increases with increasing RTs for both O_2 and S-NO_3 (red markers in Figure 4.9b). Under gaining conditions, however, the fractions F_{O2} and $F_{S\text{-}NO3}$, are relatively insensitive to changes in RTs. This insensitivity is based on the fact that the larger the hyporheic flow cell size (reactive zones), the higher solute influx and, in turn, the longer the RTs, leading to proportional changes in both solute influx and consumption. In general, median RTs in the ISGB are similar to those of the pool-riffle morphologies of Trauth et al. [2013]. The RT distributions at these pool-riffle structures follow a symmetric log-normal distribution. In contrast, in our ISGB the RT distribution is negatively skewed, with short hyporheic flow paths and short residence times being less frequent (see section 4.3.2.1). Consequently, the fraction of O_2 influx consumed in the ISGB is 20–30 % lower than in the pool-riffle morphology. However, the fraction of nitrate influx denitrified is about 35–50 % higher in the ISGB, because denitrification takes place at the margin of the hyporheic flow cell, where long flow paths exist which are unaffected by the skewed residence time distribution.

Ambient groundwater flow in both the gaining and losing direction decreases hyporheic exchange

flow, hyporheic flow cell extent and residence times. This effect is generally in line with previous results from submerged structures [Cardenas and Wilson, 2007c; Boano et al., 2008; Trauth et al., 2013]. In addition, our results show that solute consumption in the hyporheic zone strongly decreases with increasing magnitude of losing and gaining flow, similar to the result of Trauth et al. [2014]. In our model, respiration rates of up to 133 mmol/m^2/d across an ISGB are simulated which are comparable to field and laboratory studies of e.g., Edmonds and Grimm [2011], Pusch [1996] and Mermillod-Blondin et al. [2005]. We observe maximum simulated S-NO_3 denitrification rates of up to 40 mmol/m^2/d, which are in line with denitrification rates observed in similar settings in hyporheic sediments by e.g., Opdyke et al. [2006], Arango et al. [2007], Birgand et al. [2007] and Pinay et al. [2009].

4.4.2 Net Denitrification of Stream Water-Derived Nitrate in an In-Stream Gravel Bar

Infiltrating stream water-borne NO_3 is consumed within the hyporheic flow cell and, as a result, the water that re-enters the stream has potentially lower NO_3 concentrations, leading to net attenuation of in-stream nitrate loads. This change in in-stream NO_3 load can be calculated by dividing the consumed solutes in the HZ per streambed area by the NO_3 load in the stream water:

$$\text{Removed fraction of } NO_3 \text{ load} = 100 \times \frac{NO_3 \text{ denitrification in the HZ} \times \text{Streambed area}}{NO_3 \text{ load in stream water}} \tag{4.3}$$

Figures 4.10a and 4.10b show the resulting fraction of the NO_3 load removed for a hypothetical stream reach of 1 km, with a width of 10 m and in-stream NO_3 concentration of 10 mg/L. The highest removal, of up to 8 % of the in-stream NO_3 load is observed at the lowest stream discharge, when the total in-stream NO_3 load is low and hyporheic RTs are long. However, with increasing stream discharge, the fraction of stream NO_3 load removed decreases rapidly with increasing stream discharge, to near 0 % removal at high discharge, because the stream NO_3 load increases more rapidly with discharge than does its consumption in the hyporheic sediments. In addition, even minor groundwater losing and gaining conditions significantly decrease NO_3 removal of NO_3 load in the stream water. NO_3 removal under losing conditions is significantly lower than under gaining, an effect of denitrification occurring outside of the hyporheic flow cells (section 4.3.3.1). In addition to the stream water borne nitrate, upwelling groundwater also represents a source of nitrate to the hyporheic zone (denoted as G-NO_3 in our model). At the reactive fringe of the hyporheic flow cell, stream solutes and groundwater solutes mix, stimulating reactions. In our model, the magnitude of the upwelling nitrate source G-NO_3 increases with increasing magnitude of Δh. Under these conditions, the size of the hyporheic flow cell and of the reactive fringe where denitrification of G-NO_3 is possible, is also the smallest. Thus, due to reduced reactive zones, the higher the G-NO_3 solute influx the lower its total consumption and its consumption as a fraction of the influx. Strikingly, our model indicates that only very small fractions of the G-NO_3 influx are consumed and, consequently, ambient groundwater inflow into the stream can be a source of unreacted G-NO_3 to the stream. This suggests that if groundwater NO_3 concentrations are higher than concentrations in the stream, gaining conditions could result in increased NO_3 concentrations and load in the stream.

It should be noted that, in our model, NO_3 concentrations in the stream are not adjusted for the

effects of dilution by the mass of hyporheic water that exfiltrates back to the stream. However, as the amount of hyporheic water re-entering the stream is very small compared to total stream discharge, resulting effects on stream discharge, and therefore on stream concentrations, would be minor. In addition, NO_3 loads in our model are assumed to be constant across the range of simulated stream discharges.

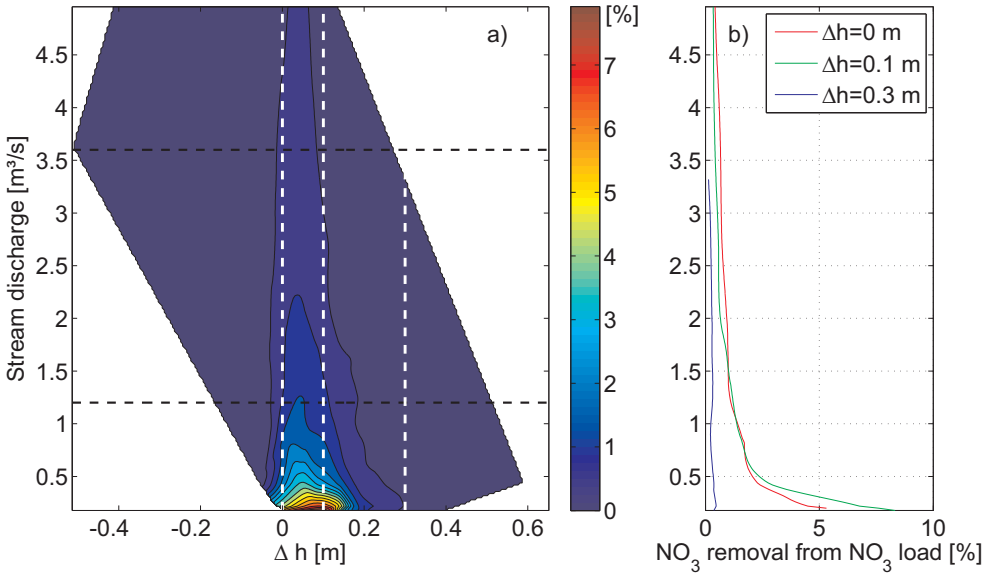

Figure 4.10: a) Percentage of S-NO_3 removed from S-NO_3 load in the stream water along a hypothetic 1 km long stream section plotted in relation to stream discharge and Δh, b) extracted values at three constant Δh for the gaining case, from along the white dashed lines of the contour plot in Figure 4.10a.

4.4.3 Limitations and Simplifications of the Modeling Approach

In this study, we evaluate the effect of one type of morphological structure, an ISGB, on hyporheic exchange. In reality, hyporheic exchange would also be generated at smaller morphological features (e.g. ripples) as well as at larger scales (e.g. intra-meander flow, deeper hyporheic flow paths), broadening the distribution of hyporheic residence times. Compared to studies of hyporheic exchange at these different scales [e.g. Cardenas and Wilson, 2007a; Boano et al., 2010] hyporheic residence times through our modeled ISGB are intermediate but long enough for denitrification to take place [Zarnetske et al., 2011a; Boano et al., 2014]. Including longer hyporheic flow paths, e.g. across a larger ISGB or a sequence of structures, would likely increase the potential for denitrification, whereas incorporating shorter flow paths would have no effect on net denitrification. The effects of including longer hyporheic flow paths could be particularly relevant under losing conditions. Here, a significant portion of the infiltrating stream solutes could potentially rejoin to the stream at a subsequent downstream feature, instead of leaving the modeling domain in subsurface flow paths, as occurs in our modeling approach. In this sense our results have to be seen as a lower envelope for the denitrification capacity in streams with ISGB morphology.

Overall, our estimates of net denitrification (section 4.4.2) are on the same order of magnitude as previously reported by field studies for river systems of similar size and morphology. Dent et al. [2007] reported total in-stream NO_3 removal of 7 % for a 400 m stream reach with a sequence of fluvial islands and gravel bars. Alexander et al. [2009] observed removal of up to 10 % per

kilometer in a third order stream with a comparable nitrate load in the month of July. During the subsequent summer months, this percentage increased up to 30 %. The higher nitrate removal calculated by both these studies can be attributed to longer hyporheic flow paths enabling higher denitrification efficiency and other removal pathways (e.g. biological assimilation). However, our results clearly suggest that in-stream structures of the type investigated here could be an important contributor to hyporheic denitrification efficiency.

In our modeling approach we simulate multiple steady state conditions to represent hydrological variability. By doing so we do not capture the full complexity of transient surface-subsurface water exchange (e.g. bank storage) induced by seasonal and event based stream and groundwater level fluctuations. Cardenas [2010] showed that transient conditions lead to an increase in hyporheic flux through an in-stream gravel bar. Similarly, Boano et al. [2007] and Shope [2009] observed that unsteady flows increased water exchange rates, accompanied by shorter hyporheic residence times. In our steady state modeling we may, therefore, overestimate solute consumption efficiency during times with pronounced surface water transients. However, it should be noted that rivers with natural flow regimes versus those with artificial flow regimes such as the pulsed flow regime caused by reservoir releases in Cardenas [2010], often experience extended periods of relatively steady stream flow (especially during phases of lower stream flows). If these periods extend significantly longer than the mean hyporheic residence times, our steady state assumption is justified.

In our simulations hydraulic conductivity is homogeneous, with an anisotropy ratio of 13, and the same for all simulations (see section 4.2.4). An increased hydraulic conductivity (proportionally in all three spatial directions) would increase HEF and solute influx, but at the same time decrease residence times. Consequently, for scenarios with higher hydraulic conductivity absolute solute consumption could increase, but the fraction of removal would presumably be lower. Nevertheless, assuming homogeneous hydraulic conductivity remains a simplification, as streambeds typically show some heterogeneity. Studies on the effect of heterogeneous streambed sediments have revealed inconsistent results with respect to hyporheic exchange and residence times, ranging from strong to negligible [Salehin et al., 2004; Sawyer and Cardenas, 2009; Bardini et al., 2013; Gomez-Velez et al., 2014].

Furthermore, dispersivity has an effect on solute transport and reactions, with higher dispersivity reflecting a less sharp solute front [Jin et al., 2010; Bardini et al., 2012; Hester et al., 2014]. Higher dispersivity would enhance solute mixing, presumably enlarging reactive areas and, consequently, increasing reactive efficiency. This effect would be most relevant when solutes are not evenly distributed, such that their reactive transformation would depend on their mixing with other reactants. This is the case for the denitrification of groundwater-borne nitrate (G-NO_3) being dependent on a source of DOC, such as from infiltrating stream water. In contrast, hyporheic reactions between commonly sourced solutes (e.g. two solutes both derived from the stream) are mainly controlled by the size of the hyporheic flow cell and hyporheic residence times. Hence, dispersion has a role in hyporheic reactions, but mainly for mixing dependent reactions [Hester et al., 2014].

In addition to the advective-dispersive influx of O_2 along hyporheic flow paths, O_2 can be introduced to the shallow groundwater by diffusion through the unsaturated zone following concentration gradients between air and water according to Fick's law. In order to evaluate the

importance of this diffusive transport, we modeled 10 low stream discharge scenarios with disabled gas diffusion. These scenarios contained the largest unsaturated zones, where the possible effects of O_2 diffusion should be most pronounced. These scenarios showed that O_2 consumption was, at most, 1 % lower when O_2 diffusion was disabled compared to the base case scenarios with enabled diffusion. Denitrification was enhanced by 0.8–1.5 % relative to the base case scenarios when diffusion was disabled. Hence, we conclude that O_2 diffusion has a negligible effect on both solute distribution and reactions in the subsurface for our scenarios, most likely due to the low O_2 concentration gradients between air and water in the ISGB. These low gradients are likely the result of abundant O_2 in the saturated zone due to the dominantly advective transport of O_2 by infiltrating stream water. However, for larger fluvial islands the effect of additional diffusive influx of O_2 through a possibly thicker unsaturated zone should still be considered.

4.5 Summary and Conclusions

In this study, we couple three-dimensional CFD simulations to a reactive transport groundwater model in order to simulate the effect of hydraulic conditions on the biogeochemical functioning of an in-stream gravel bar. In particular, we evaluate the effects of stream discharge, stream stage and ambient groundwater conditions (neutral, losing, and gaining) on hyporheic exchange, solute fluxes and reactions. This work advances our understanding of the functioning and spatial distribution of complex hyporheic exchange resulting from intermediate scale streambed structures. Furthermore, this study highlights the relevance of the contribution of such structures to the efficiency of denitrification in fluvial systems.

Hydraulic head gradients across a partially submerged ISGB induce infiltration of stream water in the secondary stream channel and exfiltration in the primary stream channel, forming a hyporheic flow cell underneath the ISGB. Hydraulic head gradients and hyporheic exchange flows (HEF) decrease with increasing stream discharge, contrary to what has been reported for fully submerged streambed structures. Losing and gaining conditions induced by ambient groundwater heads significantly reduce HEF and hyporheic flow cell extent. The fraction of HEF of total stream discharge is on the order of 0.1 - 2 %, with its maximum under low stream discharge and neutral conditions (no net gradient between groundwater and stream).

Residence times for the hyporheic flow paths are up to 8.3 hours and show a log-normal distribution. Residence time distributions show a negative skewness that decreases with increasing stream discharge, demonstrating that under low flow conditions short flow paths with short residence times do not exist. This skewed distribution leads to slightly lower aerobic respiration efficiency compared to fully submerged structures, where the residence time distributions tend to be more symmetric. In contrast, the efficiency of denitrification is higher for partially submerged bedforms, like the ISGB, because larger hyporheic flow cells and reactive zones can develop than in submerged pool-riffle structures.

Solute transformation in the hyporheic zone strongly decreases with increasing magnitude of losing or gaining conditions. This effect is mainly the result of a diminished hyporheic flow cell size and the associated shorter RTs. The highest reactive potential of the hyporheic zone can be realized under neutral conditions, where aerobic respiration rates of up to 133 $mmol/m^2/d$ and denitrification rates of up to 40 $mmol/m^2/d$ are observed. In the gaining and the losing cases,

aerobic respiration and denitrification occur at markedly different locations in the subsurface. Under gaining conditions, solutes infiltrating from the stream are constrained to the hyporheic flow cell where aerobic respiration is the dominant reactive process. At the margin of the hyporheic flow cell a reactive zone develops where stream-borne nitrate (S-NO_3) can be denitrified. With increasing magnitudes of upwelling groundwater, the spatial extent of this reactive zone shrinks with the size of the hyporheic flow cell. At the lower rim of this zone groundwater borne nitrate G-NO_3 can be denitrified in small quantities as it mixes with DOC from the stream. Under losing conditions, the presence of stream-borne solutes is not restricted to the extent of the hyporheic flow cell and aerobic respiration and denitrification may occur outside of the hyporheic flow cell. These reactions do not affect local stream water concentrations as they take place along flow paths that do not immediately return to the stream, however, they may still impact stream water concentrations further downstream, if they are part of a longer hyporheic flow path.
Our modeling results suggest that morphological structures, like ISGBs, have a higher capacity to denitrify stream- and groundwater-borne nitrate than fully submerged pool-riffle structures of similar dimension due to larger reactive zones and hyporheic exchange volumes. Over a 1 km stream reach 5 - 8 % of the NO_3 load in the stream water may be denitrified under slightly gaining conditions ($\Delta h < 0.1$ m) by hyporheic flow through morphological structures like the ISGB. This fraction declines significantly with increasing stream discharge or with even slight magnitudes of losing and gaining conditions. We conclude that in-stream structures similar to our modeled ISGB can be a significant sink for nitrate in fluvial systems, although one which is strongly controlled by both stream and groundwater hydraulics.

5 | General Summary and Conclusions

5.1 Summary

5.1.1 Hyporheic Flow and Residence Times

In this thesis, hyporheic exchange flow is investigated at fully and partially submerged streambed structures by a numerical modeling approach that is able to simulate different water stages and turbulent effects that generate complex hydraulic head distributions across the streambed. This hydraulic head distribution is used as the top boundary condition in a groundwater model and induces significant hyporheic exchange fluxes at both the partially and fully submerged morphologies.

In pool-riffle structures, the hydraulic head distribution is generated by variations in near-bed velocity and is strongly related to the extent of eddies in the pool region. The observed hydraulic head variation of high and low heads at the upstream and downstream side of the structures respectively, induces a hyporheic exchange flux through the riffle forming a hyporheic flow cell. Hydraulic head gradients increase with stream discharge and hence hyporheic exchange flux increase as well. The faster water flow leads to a decrease of residence times with increasing stream discharge. These findings are generally in line with studies of previous 2D morphologies [e.g Cardenas and Wilson, 2007b]. However, the novel three-dimensional modeling approach used in this study is able to capture eddies in the pool region that are responsible for a complex hydraulic head distribution at the streambed, varying also in lateral direction (perpendicular to the stream flow). As highest hydraulic heads occur next to the stream center and lowest heads at the downstream side with a greater distance to the center, the hyporheic flow paths deviate from a pure longitudinal flow with an average fraction of 20 % of the longitudinal flow distance. With increasing bedform amplitude of the pool-riffle morphologies, the hyporheic exchange flux increases up to a threshold where hyporheic exchange flux is insensitive to further increase of bedform amplitude. Also, hyporheic residence times decrease with increasing bedform height, because hydraulic head gradients are significantly smaller at shallow pool-riffle amplitudes leading to slower flow velocities. Furthermore, at pool-riffle morphologies surface water waves influence hyporheic exchange which is a novel aspect in investigations on hyporheic exchange. At the riffle structures Froude Numbers slightly higher than one occur, that evoke stationary surface water waves downstream of the initial water level rise of a hydraulic jump (undular hydraulic jumps) [Chanson, 2009]. In case of an interference of a wave trough of low hydrostatic pressure with the upstream side of a riffle, where commonly high hydraulic heads occur, the resulting hydraulic head will be reduced. Consequently, hydraulic head gradients at the streambed and thus water and solute flux will be decreased by this effect. Due to the three-dimensionality of the surface water waves, interferences can occur at particular spots at the streambed and do not necessarily extend over the entire channel width.

Under low stream discharge conditions streambed structures like gravel bars and fluvial islands

with partially emerged streambed occur. In comparison to fully submerged structures, the hydraulic head gradients are induced primarily by water level differences around the in-stream structure. At the in-stream gravel bar investigated here, the hydraulic head gradients are a result of opposed riffles in the channels that induce water level differences. In contrast to submerged structures, the hydraulic head gradients decrease with increasing stream discharge, leading to lower hyporheic exchange flux. In comparison to the symmetric log-normal residence time distribution of fully submerged structures, at partially submerged structures the short hyporheic flow paths are less present. This effect is pronounced under low discharge conditions, when the emerged parts of the in-stream gravel bar are large. Here, long flow paths related to the flow between the two stream channels are more frequent than the short ones. Consequently, median hyporheic residence times generally decrease with increasing discharge.
Gradients between the stream water level and the ambient groundwater level induce water exchange flows from the groundwater to the stream (gaining condition) or vice versa (losing condition). These flow paths significantly diminish hyporheic exchange flux, the extent of the hyporheic zone and also shorten hyporheic residence times for both the fully and partially submerged structures. With increasing magnitude of gaining or losing conditions, these metrics rigorously decrease which can be described by exponential functions. Therefore, gaining and losing conditions can be regarded as the counterparts to the primary driver of hyporheic exchange given by stream stage and discharge. Consequently, depending on the magnitudes of these two forces, hyporheic water flow and solute transport develop in the hyporheic zone.

5.1.2 Solute Transport and Reactions in the Hyporheic Zone

Generally, solute influx into the hyporheic zone increases with hyporheic exchange flux, transported mainly advectively. In the pool-riffle morphologies, solute consumption of the considered species (oxygen, nitrate, dissolved organic carbon) increases with increasing stream discharge and bedform amplitude, which is mainly related to larger hyporheic flow cells and thus also larger available reactive areas. In turn, reactive efficiency, represented by the consumed solutes as a fraction of solute influx is higher for low stream discharge conditions and shallow morphology, because under these conditions solute influx is significantly lower accompanied with longer residence times.
The efficiency of aerobic respiration of the partially submerged in-stream gravel bar is 20 to 30 % lower than efficiency of the submerged structures. This effect is based on the less frequent short hyporheic flow paths under partially submerged conditions that would contribute to aerobic reactions. In contrast, denitrification efficiency of partially submerged structures is about 35 to 50 % higher than below fully submerged pool-riffle structures, because reactive areas surrounding the mainly aerobic hyporheic flow cells are larger. Due to the shorter residence times in the fully submerged in-stream gravel bar, aerobic respiration is lower than under partially submerged conditions. In contrast, denitrification rates increase with increasing discharge, which is related to the increasing size of the reactive areas suitable for denitrification.
Losing and gaining conditions between stream and groundwater strongly affect solute transport and reactions in the hyporheic zone, similar to their impact on hyporheic exchange flux. Solute influx decreases with increasing magnitude of losing or gaining conditions and available area for reactions decreases accompanied with shorter residence times. These simultaneous effects lead

to a significant reduced aerobic and anaerobic solute consumption in both fully and partially submerged structures. Hence, the highest solute turn-over rates can be expected under neutral conditions, where solute flux, residence times and hyporheic flow cell size are at a maximum.
Hyporheic residence times and reactions show in general a good positive correlation when reactants are introduced along the same flow paths (stream water solutes). However, when solutes of different water sources have to get mixed before they react, the usage of residence times as a proxy for reactivity is not appropriate. This is the case when upwelling groundwater, under gaining conditions, transports solutes of nitrate or dissolved oxygen towards the streambed that possibly mix with stream water borne solutes resulting in additional reactions. For these scenarios the concentration of the upwelling solutes also influences reactions in the hyporheic zone. With increasing oxygen concentration, the consumption of the carbon source by aerobic respiration increases, but denitrification of nitrate decreases due to enlarged aerobic conditions. An increase in nitrate concentration also leads to an increase of the absolute denitrification rates. However, the denitrification efficiency (consumed nitrate of nitrate influx) decreases, because maximum denitrification rate is limited by the used Monod-Kinetics.

5.2 Conclusions

In this thesis, a modeling approach is used that enables the simulation of stream water flow and the influence on hyporheic exchange processes of water and solute flux as well as biogeochemical reactions. The results help to further understand hyporheic exchange processes and reactions on the intermediate scale and emphasize the strong influence of hydrological conditions as controlling factors.
The fraction of stream water that is exchanged through the considered individual structures is in the order of 2×10^{-2} to 1×10^{-5}, and decrease with stream discharge and degree of submergence. This seems at first to be a small fraction only, but is better appreciated when assuming that the investigated structures are common and repeating in gravelly streams. Thus, along a stream section of several kilometers a substantial amount of stream water potentially takes part at hyporheic exchange.
The modelled aerobic and anaerobic reactions show, that predominantly aerobic reactions occur in the pool-riffle and in-stream gravel bar structures. In contrast, anaerobic reactions like denitrification play a secondary role because they require conditions of low oxygen concentrations and a carbon source. These conditions are achieved when water remains relatively long in the sediments, which is not necessarily the case on the intermediate scale of gravelly streambed structures. Here, residence times are relatively short, due to strong hydraulic gradients and high hydraulic conductivities. However, bars and riffles are frequent structures in gravelly streams and thus effects on stream water quality are the result of the sum of the nitrate removal at each single structure. Hence, upscaling the results of the denitrification efficiency suggests that up to 8 % of the nitrate load in stream water with a nitrate concentration of 10 mg/L can be consumed by gravelly structures along a 1 km stream reach. Hence, streambed structures on the intermediate scale as considered in this study are an important contributor for removing nitrate from the aqueous system.
The results of this thesis show, that the interface between groundwater and streams is an

important zone that has a direct impact on nitrate removal efficiency. It is highlighted that strong gradients from the stream towards the groundwater and vice versa, can significantly reduce hyporheic exchange flux and the potential to degrade nitrate. Hence, it can be concluded that hyporheic exchange on the intermediate scale is an important and necessary process for solute turnover, but is very sensitive to hydraulic gradients between stream water and groundwater.

5.3 Limitations of the Modeling Approach and Recommendations for Future Work

The presented numerical modeling approach considers multiple steady state scenarios, although stream hydraulics can be very dynamic over time and events can lead to strong stream discharge and stage variations. Those events probably have an effect on hyporheic exchange, solute transport and reactions. Hence, investigating the effects of transient discharge conditions could be part of further studies that should also include the change of solute concentration in stream water by dilution or enhanced solute mobilization.

Hydraulic conductivity is set as homogeneous in the scenarios of pool-riffle morphologies and homogeneous with a high anisotropy ratio of 13 between the horizontal and vertical hydraulic conductivity in the model of the in-stream gravel bar. This clearly is a strong simplification in the groundwater model, because streambed sediments are commonly built up of heterogeneous sediments. However, studies with focus on the impact of heterogeneity of fluvial sediments on hyporheic exchange processes found contradictory results, ranging from strong to negligible effects [Salehin et al., 2004; Sawyer and Cardenas, 2009; Bardini et al., 2013]. To approach this discrepancy, further studies could systematically analyze the effect of heterogeneities by simulating scenarios consisting of a realistic range of variants of correlation lengths, dipping angles and standard deviations of hydraulic conductivities.

In this study, the modeled solute consumption rates are in line with rates observed in field and laboratory studies for both the consumption of oxygen [Pusch, 1996; Mermillod-Blondin et al., 2005; Edmonds and Grimm, 2011] and nitrate [Opdyke et al., 2006; Arango et al., 2007; Pinay et al., 2009]. However, it would be of great interest to delineate the spatial distribution of solutes and reactions in real fluvial systems. For this purpose, spatial highly resolved field measurements of reactive solutes and reaction products (e.g. labeled nitrogen, nitrous oxide) could be used that enable a detailed insight into reactions in the hyporheic zone.

In the reactive transport simulations, several input conditions are simplified because the focus of this thesis was primary on evaluating the effects of hydrological conditions and morphology on hyporheic exchange processes and reactions.

Firstly, the carbon source for aerobic and anaerobic reactions is considered as unlimited, easy bioavailable (labile) and transported exclusively from the streambed boundary into the hyporheic zone. Although this assumption is used in many previous studies, it does not fully reflect the real availability of carbon sources. In fact, carbon sources spatially and temporally vary which is a result of changing stream discharge, vegetation and climate [Vervier et al., 1993; Kaplan and Newbold, 2000]. Additional labile carbon sources are supposed to be generated at the streambed or within the shallow hyporheic zones, denoted as autochthonous DOC source [e.g. Brunke and Gonser, 1997; Brugger et al., 2001]. Due to the fact, that DOC supply controls metabolism in

the hyporheic zone [Kaplan and Newbold, 2000; Zarnetske et al., 2011b], DOC availability and lability for microorganisms could be addressed in further modeling studies.

Secondly, processes that play an important role in the nitrogen cycle like e.g. nitrogen assimilation by biofilms and nitrification are not considered in the reactive transport model. The effects of biofilms and biological assimilation were not included, because these complex processes are not readily implemented in the MIN3P code, which could be a task in future studies. Also, nitrification, the microbial reaction that produces nitrate by consumption of ammonia and oxygen, is not included in the modeling approach, because ammonia concentrations at the Selke site are very low compared to the nitrate concentrations (1:30). Hence, the additional production of nitrate by nitrification is of minor importance which is supported by preliminary model test runs described in section 3.2.4 and the studies of Peyrard et al. [2011], Kessler et al. [2012], and Marzadri et al. [2012]. However, in systems where ammonia concentrations are high compared to nitrate concentrations, nitrification should be considered as it can produce a significant additional amount of nitrate, which in turn possibly undergoes reactions [Jones and Holmes, 1996; Duff and Triska, 2000; Bardini et al., 2012].

Thirdly, the reaction rates for aerobic respiration and denitrification used in this study are valid for a constant temperature of 15 °C, representing the mean stream water temperature during the summer months at the Selke site. However, due to daily and seasonal variations of the temperature, reaction rates decrease with decreasing temperature according to the Arrhenius equation [Arrhenius, 1889]. Hence, temperature is an additional parameter that obviously influences reactions in the hyporheic zone and hence, heat transport with feedback to the reactions should be considered in further modeling studies.

6 | Appendix

6.1 Numerical Modeling of the Stream Water Flow by Computational Fluid Dynamics

In this thesis, the open-source Computational Fluid Dynamics (CFD) software OpenFOAM version 1.7.1 (`www.openfoam.org`) is used to simulate stream water flow over the streambed morphologies. The software solves the three-dimensional Navier-Stokes-Equations using the finite-volume approach (FVM). For the turbulence closure model Large Eddy Simulation (LES) is applied. In the used LES small scales are separated from large scales by a spatial filter determined by the cubic root of the local mesh cell volume V:

$$\Delta = (V)^{1/3} \tag{6.1}$$

where Δ is the resulting filter width that is used to decompose the velocity vector u_i and the pressure field p by

$$u_i = \overline{u}_i + u_i' \tag{6.2}$$

$$p = \overline{p} + p' \tag{6.3}$$

into the resolvable components $\overline{u}_i$ and $\overline{p}$ and the residual, subgrid scale components u_i' and p'. By substituting u_i and p by Eq. 6.2 and Eq. 6.3 the governing continuity and momentum equations for three-dimensional incompressible flow are the filtered Navier-Stokes equations:

$$\frac{\partial \overline{u}_i}{\partial x_i} = 0 \tag{6.4}$$

$$\frac{\partial \rho \overline{u}_i}{\partial t} + \frac{\partial \rho(\overline{u}_i \overline{u}_j)}{\partial x_j} = -\frac{\partial \overline{p}}{\partial x_i} + \mu \frac{\partial^2 \overline{u}_j}{\partial x_i^2} + \rho g + \frac{\partial \tau_{ij}}{\partial x_i} \tag{6.5}$$

where x_i with $i = 1, 2, 3$ represents the coordinates in three spatial directions, ρ is the density of the fluid, g is the gravitational constant, μ is the molecular viscosity and τ_{ij} is the subgrid scale (SGS) stress tensor that contains two unfiltered variables $\overline{u_i u_j}$ in the form of

$$\tau_{ij} = \overline{u}_i \overline{u}_j - \overline{u_i u_j} \tag{6.6}$$

This term cannot be resolved numerically and has to be modeled by a SGS-model. In this study, the original SGS-Model of Smagorinsky [1963] is used:

$$\tau_{ij} = -2\nu_t \overline{S}_{ij} + \frac{1}{3}\tau_{kk}\delta_{ij} \tag{6.7}$$

where δ_{ij} is the Kronecker delta and $\overline{S}_{ij}$ is the strain rate tensor defined by

$$\overline{S}_{ij} = \frac{1}{2}\left(\frac{\partial \overline{u}_i}{\partial x_j} + \frac{\partial \overline{u}_j}{\partial x_i}\right) \tag{6.8}$$

and ν_t is the subgrid eddy viscosity calculated from

$$\nu_t = (C_s \Delta)^2 \sqrt{2\overline{S}_{ij}\overline{S}_{ij}} \tag{6.9}$$

where Δ is the filter width, defined in Eq. 6.1 and C_s is the Smagorinsky coefficient with a constant value of 0.17 in all simulations.

To simulate both the water and the air fraction of the surface water model domain, a two-phase model approach, the Volume of Fluid Method (VoF) [Hirt and Nichols, 1981] is used. In the VoF-approach, the distribution of water and air in the domain is represented by a phase fraction value, denoted by α. In cells completely filled with water, α has a value of 1. A lower value indicates a specific fraction of air in the cell. Hence, the water surface is represented by $\alpha = 0.5$, where water and air fractions are equal [Shen and Diplas, 2008].
The phase fraction α is transported by:

$$\frac{\partial \alpha}{\partial t} + \frac{\partial \alpha \overline{u}_i}{\partial x_i} = 0 \tag{6.10}$$

Furthermore, a term F_i considering the surface tension force is added to the momentum equation of Eq. 6.5:

$$\frac{\partial \rho \overline{u}_i}{\partial t} + \frac{\partial \rho(\overline{u}_i \overline{u_j})}{\partial x_j} = -\frac{\partial \overline{p}}{\partial x_i} + \mu \frac{\partial^2 \overline{u}_j}{\partial x_i^2} + \rho g + \frac{\partial \tau_{ij}}{\partial x_i} + F_i \tag{6.11}$$

with

$$F_i = \sigma \kappa \frac{\partial \alpha}{\partial x_i} \tag{6.12}$$

where σ is the surface tension coefficient and κ is the curvature of the water surface.
The density and viscosity values for the numerical calculations are adjusted according to the phase fraction α for each volume cell by:

$$\rho = \alpha \rho_{water} + (1 - \alpha)\rho_{air} \tag{6.13}$$

$$\mu = \alpha \mu_{water} + (1 - \alpha)\mu_{air} \tag{6.14}$$

In the VoF-approach an adjustment of the convection equation for the phase fraction α is necessary to obtain a sharp interface between water and air without smearing. Therefore, in OpenFOAM an extra term with an artificial compression, represented by a velocity field u_r is added to the transport equation (Eq. 6.10) which is only active for the air-water interface [Rusche, 2003]:

$$\frac{\partial \alpha}{\partial t} + \frac{\partial \alpha \overline{u}_i}{\partial x_i} + \frac{\partial \alpha(1 - \alpha) u_r}{\partial x_i} = 0 \tag{6.15}$$

Bibliography

Alexander, R. B., Böhlke, J. K., Boyer, E. W., David, M. B., Harvey, J. W., Mulholland, P. J., Seitzinger, S. P., Tobias, C. R., Tonitto, C., and Wollheim, W. M. (2009). Dynamic modeling of nitrogen losses in river networks unravels the coupled effects of hydrological and biogeochemical processes. *Biogeochemistry*, 93(1-2):91–116.

Angermann, L., Lewandowski, J., Fleckenstein, J. H., and Nützmann, G. (2012). A 3D analysis algorithm to improve interpretation of heat pulse sensor results for the determination of small-scale flow directions and velocities in the hyporheic zone. *Journal of Hydrology*, 475:1–11.

Appelo, C. A. J. and Postma, D. (2005). *Geochemistry, Groundwater and Pollution*. Balkema Publishers, Amsterdam.

Arango, C. P., Tank, J. L., Schaller, J. L., Royer, T. V., Bernot, M. J., and David, M. B. (2007). Benthic organic carbon influences denitrification in streams with high nitrate concentration. *Freshwater Biology*, 52(7):1210–1222.

Arnon, S., Gray, K. A., and Packman, A. I. (2007). Biophysicochemical process coupling controls nitrate use by benthic biofilms. *Limnology and Oceanography*, 52(4):1665–1671.

Arrhenius, S. (1889). Über die Reaktionsgeschwindigkeit bei der Inversion von Rohrzucker durch Säuren. *Zeitschrift für physikalische Chemie*, 4:226–248.

Baker, M., Dahm, C., and Valett, H. (2000). 11 - Anoxia, Anaerobic Metabolism, and Biogeochemistry of the Stream-water – Groundwater Interface. In Jones, J. B. and Mullholland, P. J., editors, *Streams and Ground Waters*, pages 259–284. Academic Press, San Diego.

Bardini, L., Boano, F., Cardenas, M., Sawyer, A., Revelli, R., and Ridolfi, L. (2013). Small-scale permeability heterogeneity has negligible effects on nutrient cycling in streambeds. *Geophysical Research Letters*, 40(6):1118–1122.

Bardini, L., Boano, F. and, M., Revelli, R., and Ridolfi, L. (2012). Nutrient cycling in bedform induced hyporheic zones. *Geochimica et Cosmochimica Acta*, 84:47–61.

Bartsch, S., Shope, C. L., Arnhold, S., Jeong, J.-J., Park, J.-H., Eum, J., Kim, B., Peiffer, S., and Fleckenstein, J. H. (2013). Monsoonal-type climate or land-use management: Understanding their role in the mobilization of nitrate and DOC in a mountainous catchment. *Journal of Hydrology*, 507:149–162.

Battin, T. J., Kaplan, L. A., Newbold, J. D., and Hendricks, S. P. (2003). A mixing model analysis of stream solute dynamics and the contribution of a hyporheic zone to ecosystem function. *Freshwater Biology*, 48(6):995–1014.

Bencala, K. E. (2000). Hyporheic zone hydrological processes. *Hydrological Processes*, 14(15):2797–2798.

Benner, R. (2003). 5 - Molecular Indicators of the Bioavailability of Dissolved Organic Matter. In Sinsabaugh, S. E. G. and Findlay, R. L., editors, *Aquatic Ecosystems*, Aquatic Ecology, pages 121–137. Academic Press, Burlington.

Birgand, F., Skaggs, R. W., Chescheir, G. M., and Gilliam, J. W. (2007). Nitrogen removal in streams of agricultural catchments - A Literature Review. *Critical Reviews in Environmental Science and Technology*, 37(5):381–487.

Boano, F., Camporeale, C., Revelli, R., and Ridolfi, L. (2006). Sinuosity-driven hyporheic exchange in meandering rivers. *Geophysical Research Letters*, 33(18).

Boano, F., Demaria, A., Revelli, R., and Ridolfi, L. (2010). Biogeochemical zonation due to intrameander hyporheic flow. *Water Resources Research*, 46(2).

Boano, F., Harvey, J. W., Marion, A., Packman, A. I., Revelli, R., Ridolfi, L., and Wörman, A. (2014). Hyporheic flow and transport processes: Mechanisms, models, and biogeochemical implications. *Reviews of Geophysics*, pages 603–679.

Boano, F., Revelli, R., and Ridolfi, L. (2007). Bedform-induced hyporheic exchange with unsteady flows. *Advances in Water Resources*, 30(1):148–156.

Boano, F., Revelli, R., and Ridolfi, L. (2008). Reduction of the hyporheic zone volume due to the stream-aquifer interaction. *Geophysical Research Letters*, 35(9).

Boano, F., Revelli, R., and Ridolfi, L. (2009). Quantifying the impact of groundwater discharge on the surface-subsurface exchange. *Hydrological Processes*, 23(15):2108–2116.

Boulton, A. J., Findlay, S., Marmonier, P., Stanley, E. H., and Valett, H. M. (1998). The functional significance of the hyporheic zone in streams and rivers. *Annual Review of Ecology and Systematics*, 29:59–81.

Brugger, A., Wett, B., Kolar, I., Reitner, B., and Herndl, G. J. (2001). Immobilization and bacterial utilization of dissolved organic carbon entering the riparian zone of the alpine Enns River, Austria. *Aquatic Microbial Ecology*, 24(2):129–142.

Brunke, M. and Gonser, T. O. M. (1997). The ecological significance of exchange processes between rivers and groundwater. *Freshwater Biology*, 37(1):1–33.

Buffington, J. M. and Tonina, D. (2009). Hyporheic exchange in mountain rivers II: Effects of channel morphology on mechanics, scales, and rates of exchange. *Geography Compass*, 3(3):1038–1062.

Cardenas, M. B. (2008). Surface water-groundwater interface geomorphology leads to scaling of residence times. *Geophysical Research Letters*, 35(8).

Cardenas, M. B. (2009). Stream-aquifer interactions and hyporheic exchange in gaining and losing sinuous streams. *Water Resources Research*, 45(6).

Cardenas, M. B. (2010). Lessons from and assessment of boussinesq aquifer modeling of a large fluvial island in a dam-regulated river. *Advances in Water Resources*, 33(11):1359–1366.

Cardenas, M. B., Cook, P. L., Jiang, H., and Traykovski, P. (2008). Constraining denitrification in permeable wave-influenced marine sediment using linked hydrodynamic and biogeochemical modeling. *Earth and Planetary Science Letters*, 275(1-2):127–137.

Cardenas, M. B. and Wilson, J. (2007a). Hydrodynamics of coupled flow above and below a sediment-water interface with triangular bedforms. *Advances in Water Resources*, 30(3):301–313.

Cardenas, M. B. and Wilson, J. L. (2007b). Dunes, turbulent eddies, and interfacial exchange with permeable sediments. *Water Resources Research*, 43(8).

Cardenas, M. B. and Wilson, J. L. (2007c). Exchange across a sediment-water interface with ambient groundwater discharge. *Journal of Hydrology*, 346(3-4):69–80.

Cardenas, M. B., Wilson, J. L., and Zlotnik, V. A. (2004). Impact of heterogeneity, bed forms, and stream curvature on subchannel hyporheic exchange. *Water Resources Research*, 40(8).

Chanson, H. (2009). Current knowledge in hydraulic jumps and related phenomena. A survey of experimental results. *European Journal of Mechanics - B/Fluids*, 28(2):191–210.

Chanson, H. and Montes, J. (1995). Characteristics of undular hydraulic jumps: Experimental apparatus and flow patterns. *Journal of Hydraulic Engineering*, 121(2):129–144.

Chen, X. and Chen, X. (2003). Effects of aquifer anisotropy on the migration of infiltrated stream water to a pumping well. *Journal of Hydrologic Engineering*, 8(5):287–293.

Cheng, C. and Chen, X. (2007). Evaluation of methods for determination of hydraulic properties in an aquifer–aquitard system hydrologically connected to a river. *Hydrogeology Journal*, 15(4):669–678.

Cheng, N.-S. and Chiew, Y.-M. (1998). Modified logarithmic law for velocity distribution subjected to upward seepage. *Journal of Hydraulic Engineering*, 124(12):1235–1241.

Dahm, C. N., Grimm, N. B., Marmonier, P., Valett, H. M., and Vervier, P. (1998). Nutrient dynamics at the interface between surface waters and groundwaters. *Freshwater Biology*, 40(3):427–451.

Dent, C. L., Grimm, N. B., Martí, E., Edmonds, J. W., Henry, J. C., and Welter, J. R. (2007). Variability in surface-subsurface hydrologic interactions and implications for nutrient retention in an arid-land stream. *Journal of Geophysical Research*, 112(G4).

Diem, S., Cirpka, O. A., and Schirmer, M. (2013). Modeling the dynamics of oxygen consumption upon riverbank filtration by a stochastic–convective approach. *Journal of Hydrology*, 505:352–363.

Doussan, C., Poitevin, G., Ledoux, E., and Detay, M. (1997). River bank filtration: modelling of the changes in water chemistry with emphasis on nitrogen species. *Journal of Contaminant Hydrology*, 25(1):129–156.

Duff, J. H. and Triska, F. J. (2000). 8 - Nitrogen Biogeochemistry and Surface-Subsurface Exchange in Streams. In Jones, J. B. and Mulholland, P. J., editors, *Streams and Ground Waters*, pages 197–220. Academic Press, San Diego.

Edmonds, J. W. and Grimm, N. B. (2011). Abiotic and biotic controls of organic matter cycling in a managed stream. *Journal of Geophysical Research*, 116(G2).

Edwards, R. T. (1998). 16 – the hyporheic zone. In Naiman, R. and Bilby, R. E., editors, *River ecology and management: Lessons from the Pacific coastal ecoregion*, pages 399–429. Springer Science & Business Media, New York.

Elliott, A. H. and Brooks, N. H. (1997a). Transfer of nonsorbing solutes to a streambed with bed forms: Laboratory experiments. *Water Resources Research*, 33(1):137–151.

Elliott, A. H. and Brooks, N. H. (1997b). Transfer of nonsorbing solutes to a streambed with bed forms: Theory. *Water Resources Research*, 33(1):123–136.

Endreny, T., Lautz, L., and Siegel, D. I. (2011). Hyporheic flow path response to hydraulic jumps at river steps: Flume and hydrodynamic models. *Water Resources Research*, 47(2).

Engelhardt, I., Barth, J., Bol, R., Schulz, M., Ternes, T., Schüth, C., and van Geldern, R. (2014). Quantification of long-term wastewater fluxes at the surface water/groundwater-interface: An integrative model perspective using stable isotopes and acesulfame. *Science of the Total Environment*, 466-467:16–25.

Engelhardt, I., Piepenbrink, M., Trauth, N., Stadler, S., Kludt, C., Schulz, M., Schüth, C., and Ternes, T. (2011). Comparison of tracer methods to quantify hydrodynamic exchange within the hyporheic zone. *Journal of Hydrology*, 400(1-2):255–266.

Erisman, J. W., Sutton, M. A., Galloway, J., Klimont, Z., and Winiwarter, W. (2008). How a century of ammonia synthesis changed the world. *Nature Geoscience*, 1(10):636–639.

Fehlman, H. M. (1985). Resistance components and velocity distributions of open channel flows over bedforms. Master's thesis, Colorado State University.

Findlay, S. (1995). Importance of surface-subsurface exchange in stream ecosystems: The hyporheic zone. *Limnology and oceanography*, 40(1):159–164.

Fleckenstein, J. H., Krause, S., Hannah, D. M., and Boano, F. (2010). Groundwater-surface water interactions: New methods and models to improve understanding of processes and dynamics. *Advances in Water Resources*, 33(11):1291–1295.

Fleckenstein, J. H., Niswonger, R. G., and Fogg, G. E. (2006). River-aquifer interactions, geologic heterogeneity, and low-flow management. *Groundwater*, 44(6):837–852.

Fox, A., Boano, F., and Arnon, S. (2014). Impact of losing and gaining streamflow conditions on hyporheic exchange fluxes induced by dune-shaped bed forms. *Water Resources Research*, 50(3):1895–1907.

Francis, B. A., Francis, L. K., and Cardenas, M. B. (2010). Water table dynamics and groundwater-surface water interaction during filling and draining of a large fluvial island due to dam-induced river stage fluctuations. *Water Resources Research*, 46(7).

Frei, S., Knorr, K. H., Peiffer, S., and Fleckenstein, J. H. (2012). Surface micro-topography causes hot spots of biogeochemical activity in wetland systems: A virtual modeling experiment. *Journal of Geophysical Research*, 117.

Fuss, C. and Smock, L. (1996). Spatial and temporal variation of microbial respiration rates in a blackwater stream. *Freshwater Biology*, 36(2):339–349.

Galloway, J. N., Dentener, F. J., Capone, D. G., Boyer, E. W., Howarth, R. W., Seitzinger, S. P., Asner, G. P., Cleveland, C. C., Green, P. A., Holland, E. A., Karl, D. M., Michaels, A. F., Porter, J. H., Townsend, A. R., and Vöosmarty, C. J. (2004). Nitrogen cycles: Past, present, and future. *Biogeochemistry*, 70(2):153–226.

García-Ruiz, R., Pattinson, S. N., and Whitton, B. A. (1998). Kinetic parameters of denitrification in a river continuum. *Applied and Environmental Microbiology*, 64(7):2533–2538.

Giordano, M. (2009). Global groundwater? Issues and Solutions. *Annual Review of Environment and Resources*, 34(1):153–178.

Gomez-Velez, J. D. and Harvey, J. W. (2014). A hydrogeomorphic river network model predicts where and why hyporheic exchange is important in large basins. *Geophysical Research Letters*, 41(18):2014GL061099.

Gomez-Velez, J. D., Krause, S., and Wilson, J. L. (2014). Effect of low-permeability layers on spatial patterns of hyporheic exchange and groundwater upwelling. *Water Resources Research*, 50(6):5196–5215.

González-Pinzón, R., Ward, A. S., Hatch, C. E., Wlostowski, A. N., Singha, K., Gooseff, M. N., Haggerty, R., Harvey, J. W., Cirpka, O. A., and Brock, J. T. (2015). A field comparison of multiple techniques to quantify groundwater–surface-water interactions. *Freshwater Science*, 34(1).

Grant, G. E., Swanson, F. J., and Wolman, M. G. (1990). Pattern and origin of stepped-bed morphology in high-gradient streams, Western Cascades, Oregon. *Geological Society of America Bulletin*, 102(3):340–352.

Greig, S. M., Sear, D. A., and Carling, P. A. (2007). A review of factors influencing the availability of dissolved oxygen to incubating salmonid embryos. *Hydrological Processes*, 21(3):323–334.

Grigoriadis, D. G. E., Balaras, E., and Dimas, A. A. (2009). Large-eddy simulations of unidirectional water flow over dunes. *Journal of Geophysical Research*, 114(F2).

Gu, C., Anderson, W., and Maggi, F. (2012). Riparian biogeochemical hot moments induced by stream fluctuations. *Water Resources Research*, 48(9).

Gu, C., Hornberger, G. M., Mills, A. L., Herman, J. S., and Flewelling, S. A. (2007). Nitrate reduction in streambed sediments: Effects of flow and biogeochemical kinetics. *Water Resources Research*, 43(12).

Hall, R. O. and Tank, J. L. (2005). Correcting whole-stream estimates of metabolism for groundwater input. *Limnology and Oceanography: Methods*, 3:222–229.

Hartwig, M. and Borchardt, D. (2014). Alteration of key hyporheic functions through biological and physical clogging along a nutrient and fine-sediment gradient. *Ecohydrology*.

Harvey, J. W. and Bencala, K. E. (1993). The effect of streambed topography on surface-subsurface water exchange in mountain catchments. *Water Resources Research*, 29(1):89–98.

Hedin, L. O., Fischer, J. C. v., Ostrom, N. E., Kennedy, B. P., Brown, M. G., and Robertson, G. P. (1998). Thermodynamic constraints on nitrogen transformations and other biogeochemical processes at soil-stream interfaces. *Ecology*, 79(2):684–703.

Henderson, A., Ahrens, J., and Law, C. (2004). *The ParaView Guide*. Kitware Inc., Clifton Park, New York.

Hester, E. T., Young, K. I., and Widdowson, M. A. (2013). Mixing of surface and groundwater induced by riverbed dunes: Implications for hyporheic zone definitions and pollutant reactions. *Water Resources Research*, 49(9):5221–5237.

Hester, E. T., Young, K. I., and Widdowson, M. A. (2014). Controls on mixing-dependent denitrification in hyporheic zones induced by riverbed dunes: A steady state modeling study. *Water Resources Research*, 50(11):9048–9066.

Hill, A. R., Labadia, C. F., and Sanmugadas, K. (1998). Hyporheic zone hydrology and nitrogen dynamics in relation to the streambed topography of a N-rich stream. *Biogeochemistry*, 42(3):285–310.

Hirt, C. W. and Nichols, B. D. (1981). Volume of fluid (VOF) method for the dynamics of free boundaries. *Journal of computational physics*, 39(1):201–225.

Janssen, F., Cardenas, M. B., Sawyer, A. H., Dammrich, T., Krietsch, J., and de Beer, D. (2012). A comparative experimental and multiphysics computational fluid dynamics study of coupled surface-subsurface flow in bed forms. *Water Resources Research*, 48(8).

Jin, G., Tang, H., Gibbes, B., Li, L., and Barry, D. (2010). Transport of nonsorbing solutes in a streambed with periodic bedforms. *Advances in Water Resources*, 33(11):1402–1416.

Jones, J. B. and Holmes, R. M. (1996). Surface-subsurface interactions in stream ecosystems. *Trends in Ecology & Evolution*, 11(6):239–242.

Jones, Jr., J. B., Fisher, S. G., and Grimm, N. B. (1995). Nitrification in the hyporheic zone of a desert stream ecosystem. *Journal of the North American Benthological Society*, 14(2):249–258.

Kalbus, E., Reinstorf, F., and Schirmer, M. (2006). Measuring methods for groundwater–surface water interactions: A review. *Hydrology and Earth System Sciences*, 10(6):873–887.

Kaplan, L. and Bott, T. (1982). Diel fluctuations of DOC generated by algae in a piedmont stream. *Limnology and Oceanography*, 27(6):1091–1100.

Kaplan, L. A. and Newbold, J. D. (2000). 10 - Surface and Subsurface Dissolved Organic Carbon. In Jones, J. B. and Mulholland, P. J., editors, *Streams and Ground Waters*, pages 237–258. Academic Press, San Diego.

Kasahara, T. and Hill, A. R. (2006). Effects of riffle-step restoration on hyporheic zone chemistry in N-rich lowland streams. *Canadian Journal of Fisheries and Aquatic Sciences*, 63(1):120–133.

Kasahara, T. and Wondzell, S. M. (2003). Geomorphic controls on hyporheic exchange flow in mountain streams. *Water Resources Research*, 39(1):SBH 3–1–SBH 3–14.

Keller, E. A. (1972). Development of alluvial stream channels: A five-stage model. *Geological Society of America Bulletin*, 83(5):1531–1536.

Kennedy, C. D., Genereux, D. P., Corbett, D. R., and Mitasova, H. (2009). Spatial and temporal dynamics of coupled groundwater and nitrogen fluxes through a streambed in an agricultural watershed. *Water Resources Research*, 45(9).

Kessler, A. J., Glud, R. N., Bayani Cardenas, M., Larsen, M., Bourke, M. F., and Cook, P. L. M. (2012). Quantifying denitrification in rippled permeable sands through combined flume experiments and modeling. *Limnology and Oceanography*, 57(4):1217–1232.

Krause, S., Tecklenburg, C., Munz, M., and Naden, E. (2013). Streambed nitrogen cycling beyond the hyporheic zone: Flow controls on horizontal patterns and depth distribution of nitrate and dissolved oxygen in the upwelling groundwater of a lowland river. *Journal of Geophysical Research: Biogeosciences*, 118(1):54–67.

Lane, S. N., Hardy, R. J., Elliott, L., and Ingham, D. B. (2004). Numerical modeling of flow processes over gravelly surfaces using structured grids and a numerical porosity treatment. *Water Resources Research*, 40(1).

Lansdown, K., Trimmer, M., Heppell, C. M., Sgouridis, F., Ullah, S., Heathwaite, A. L., Binley, A., and Zhang, H. (2012). Characterization of the key pathways of dissimilatory nitrate reduction and their response to complex organic substrates in hyporheic sediments. *Limnology and Oceanography*, 57(2):387–400.

Laursen, A. E. and Seitzinger, S. P. (2002). Measurement of denitrification in rivers: An integrated, whole reach approach. *Hydrobiologia*, 485(1-3):67–81.

Lautz, L. K. and Fanelli, R. M. (2008). Seasonal biogeochemical hotspots in the streambed around restoration structures. *Biogeochemistry*, 91(1):85–104.

Lautz, L. K. and Siegel, D. I. (2006). Modeling surface and ground water mixing in the hyporheic zone using MODFLOW and MT3D. *Advances in Water Resources*, 29(11):1618–1633.

Leopold, L. B. and Wolman, M. G. (1957). River channel patterns: Braided, meandering, and straight. USGS Numbered Series 282-B, U.S. Geological Survey.

Lewandowski, J., Putschew, A., Schwesig, D., Neumann, C., and Radke, M. (2011). Fate of organic micropollutants in the hyporheic zone of a eutrophic lowland stream: Results of a preliminary field study. *Science of the Total Environment*, 409(10):1824–1835.

Lowell, J. L., Gordon, N., Engstrom, D., Stanford, J. A., Holben, W. E., and Gannon, J. E. (2009). Habitat heterogeneity and associated microbial community structure in a small-scale floodplain hyporheic flow path. *Microbial Ecology*, 58(3):611–620.

Maazouzi, C., Claret, C., Dole-Olivier, M.-J., and Marmonier, P. (2013). Nutrient dynamics in river bed sediments: effects of hydrological disturbances using experimental flow manipulations. *Journal of Soils and Sediments*, 13(1):207–219.

Malcolm, I. A., Soulsby, C., and Youngson, A. F. (2006). High-frequency logging technologies reveal state-dependent hyporheic process dynamics: Implications for hydroecological studies. *Hydrological Processes*, 20(3):615–622.

Marzadri, A., Tonina, D., and Bellin, A. (2011). A semianalytical three-dimensional process-based model for hyporheic nitrogen dynamics in gravel bed rivers. *Water Resources Research*, 47(11).

Marzadri, A., Tonina, D., and Bellin, A. (2012). Morphodynamic controls on redox conditions and on nitrogen dynamics within the hyporheic zone: Application to gravel bed rivers with alternate-bar morphology. *Journal of Geophysical Research*, 117.

Marzadri, A., Tonina, D., and Bellin, A. (2013). Effects of stream morphodynamics on hyporheic zone thermal regime. *Water Resources Research*, 49(4):2287–2302.

Marzadri, A., Tonina, D., Bellin, A., Vignoli, G., and Tubino, M. (2010). Semianalytical analysis of hyporheic flow induced by alternate bars. *Water Resources Research*, 46(7).

Mayer, K. U., Frind, E. O., and Blowes, D. W. (2002). Multicomponent reactive transport modeling in variably saturated porous media using a generalized formulation for kinetically controlled reactions. *Water Resources Research*, 38(9):13–1–13–21.

McCutchan, J., Saunders, I. I. I., Lewis, W. M., and Hayden, M. G. (2002). Effects of groundwater flux on open-channel estimates of stream metabolism. *Limnology and Oceanography*, 47:321–324.

Mermillod-Blondin, F., Mauclaire, L., and Montuelle, B. (2005). Use of slow filtration columns to assess oxygen respiration, consumption of dissolved organic carbon, nitrogen transformations, and microbial parameters in hyporheic sediments. *Water Research*, 39(9):1687–1698.

Montgomery, D. R., Buffington, J. M., Smith, R. D., Schmidt, K. M., and Pess, G. (1995). Pool spacing in forest channels. *Water Resources Research*, 31(4):1097–1105.

Mulholland, P. J., Helton, A. M., Poole, G. C., Hall, R. O., Hamilton, S. K., Peterson, B. J., Tank, J. L., Ashkenas, L. R., Cooper, L. W., Dahm, C. N., Dodds, W. K., Findlay, S. E. G., Gregory, S. V., Grimm, N. B., Johnson, S. L., McDowell, W. H., Meyer, J. L., Valett, H. M., Webster, J. R., Arango, C. P., Beaulieu, J. J., Bernot, M. J., Burgin, A. J., Crenshaw, C. L., Johnson, L. T., Niederlehner, B. R., O'Brien, J. M., Potter, J. D., Sheibley, R. W., Sobota, D. J., and Thomas, S. M. (2008). Stream denitrification across biomes and its response to anthropogenic nitrate loading. *Nature*, 452:202–205.

Munz, M., Krause, S., Tecklenburg, C., and Binley, A. (2011). Reducing monitoring gaps at the aquifer-river interface by modelling groundwater-surface water exchange flow patterns. *Hydrological Processes*, 25(23):3547–3562.

Mutz, M., Kalbus, E., and Meinecke, S. (2007). Effect of instream wood on vertical water flux in low-energy sand bed flume experiments. *Water Resources Research*, 43(10).

Naegeli, M. W. and Uehlinger, U. (1997). Contribution of the hyporheic zone to ecosystem metabolism in a prealpine gravel-bed-river. *Journal of the North American Benthological Society*, 16(4):794.

Nicholas, A. (2001). Computational fluid dynamics modelling of boundary roughness in gravel-bed rivers: An investigation of the effects of random variability in bed elevation. *Earth Surface Processes and Landforms*, 26(4):345–362.

O'Connor, B. L. and Hondzo, M. (2007). Enhancement and inhibition of denitrification by fluid-flow and dissolved oxygen flux to stream sediments. *Environmental science & technology*, 42(1):119–125.

Odum, H. T. (1956). Primary production in flowing waters. *Limnology and Oceanography*, 1(2):102–117.

Oki, T. and Kanae, S. (2006). Global hydrological cycles and world water resources. *Science*, 313(5790):1068–1072.

Opdyke, M. R., David, M. B., and Rhoads, B. L. (2006). Influence of geomorphological variability in channel characteristics on sediment denitrification in agricultural streams. *Journal of Environmental Quality*, 35(6):2103–2112.

Orghidan, T. (1959). Ein neuer Lebensraum des unterirdischen Wassers: Der hyporheische Biotop. *Archiv fur Hydrobiologie*, 55:392–414.

Osterkamp, W. R. (1998). Processes of fluvial island formation, with examples from Plum Creek, Colorado and Snake River, Idaho. *Wetlands*, 18(4):530–545.

Packman, A. I., Brooks, N. H., and Morgan, J. J. (2000). A physicochemical model for colloid exchange between a stream and a sand streambed with bed forms. *Water Resources Research*, 36(8):2351–2361.

Packman, A. I., Salehin, M., and Zaramella, M. (2004). Hyporheic exchange with gravel beds: Basic hydrodynamic interactions and bedform-induced advective flows. *Journal of Hydraulic Engineering*, 130(7):647–656.

Peyrard, D., Delmotte, S., Sauvage, S., Namour, P., Gerino, M., Vervier, P., and Sanchez-Perez, J. (2011). Longitudinal transformation of nitrogen and carbon in the hyporheic zone of an N-rich stream: A combined modelling and field study. *Physics and Chemistry of the Earth, Parts A/B/C*, 36(12):599–611.

Pinay, G., O'Keefe, T. C., Edwards, R. T., and Naiman, R. J. (2009). Nitrate removal in the hyporheic zone of a salmon river in Alaska. *River Research and Applications*, 25(4):367–375.

Polatel, C. (2006). *Large-scale roughness effect on free-surface and bulk flow characteristics in open-channel flows*. PhD thesis, The University of Iowa, Iowa.

Precht, E., Franke, U., Polerecky, L., and Huettel, M. (2004). Oxygen dynamics in permeable sediments with wave-driven pore water exchange. *Limnology and Oceanography*, 49(3):693–705.

Prinos, P. (1995). Bed-suction effects on structure of turbulent open-channel flow. *Journal of Hydraulic Engineering*, 121(5):404–412.

Pusch, M. (1996). The metabolism of organic matter in the hyporheic zone of a mountain stream, and its spatial distribution. *Hydrobiologia*, 323(2):107–118.

Rusche, H. (2003). *Computational fluid dynamics of dispersed two-phase flows at high phase fractions*. PhD thesis, Imperial College, University of London.

Saenger, N., Kitanidis, P. K., and Street, R. L. (2005). A numerical study of surface-subsurface exchange processes at a riffle-pool pair in the Lahn River, Germany. *Water Resources Research*, 41(12).

Salehin, M., Packman, A. I., and Paradis, M. (2004). Hyporheic exchange with heterogeneous streambeds: Laboratory experiments and modeling. *Water Resources Research*, 40(11).

Sampat, P. and Peterson, J. A. (2000). *Deep Trouble: The Hidden Threat of Groundwater Pollution*. Worldwatch Institute, Washington, DC.

Sawyer, A. H. and Cardenas, M. B. (2009). Hyporheic flow and residence time distributions in heterogeneous cross-bedded sediment. *Water Resources Research*, 45(8).

Schmidt, C., Bayer-Raich, M., and Schirmer, M. (2006). Characterization of spatial heterogeneity of groundwater-stream water interactions using multiple depth streambed temperature measurements at the reach scale. *Hydrology and Earth System Sciences*, 10(6):849–859.

Schmidt, C., Musolff, A., Trauth, N., Vieweg, M., and Fleckenstein, J. H. (2012). Transient analysis of fluctuations of electrical conductivity as tracer in the stream bed. *Hydrology and Earth System Sciences*, 16(10):3689–3697.

Seitzinger, S. P., Styles, R. V., Boyer, E. W., Alexander, R. B., Billen, G., Howarth, R. W., Mayer, B., and Breemen, N. v. (2002). Nitrogen retention in rivers: Model development and application to watersheds in the northeastern U.S.A. *Biogeochemistry*, 57-58(1):199–237.

Shanafield, M., Pohll, G., and Susfalk, R. (2010). Use of heat-based vertical fluxes to approximate total flux in simple channels. *Water Resources Research*, 46(3).

Shen, Y. and Diplas, P. (2008). Application of two- and three-dimensional computational fluid dynamics models to complex ecological stream flows. *Journal of Hydrology*, 348(1):195–214.

Shiklomanov, I. A. (1997). *Comprehensive assessment of the freshwater resources of the world: Assessment of water resources and water availability in the world*. World Meteorological Organization.

Shope, C. L. (2009). *Water and heat fluxes in a channel bar compared with adjacent streambed and streambank*. PhD thesis, University of Nevada, Reno.

Shope, C. L., Constantz, J. E., Cooper, C. A., Reeves, D. M., Pohll, G., and McKay, W. A. (2012). Influence of a large fluvial island, streambed, and stream bank on surface water-groundwater fluxes and water table dynamics. *Water Resources Research*, 48(6).

Smagorinsky, J. (1963). General circulation experiments with the primitive equations. *Monthly Weather Review*, 91(3):99–164.

Stanford, J. A. and Ward, J. V. (1988). The hyporheic habitat of river ecosystems. *Nature*, 335(6185):64–66.

Stonedahl, S. H., Harvey, J. W., Wörman, A., Salehin, M., and Packman, A. I. (2010). A multiscale model for integrating hyporheic exchange from ripples to meanders. *Water Resources Research*, 46(12).

Storey, R. G., Howard, K. W. F., and Williams, D. D. (2003). Factors controlling riffle-scale hyporheic exchange flows and their seasonal changes in a gaining stream: A three-dimensional groundwater flow model. *Water Resources Research*, 39(2).

Stuart, T. A. (1953). Water currents through permeable gravels and their significance to spawning salmonids, etc. *Nature*, 172(4374):407–408.

Stuart, T. A. (1954). Spawning sites of trout. *Nature*, 173(4399):354–354.

Stumm, W. and Morgan, J. J. (2012). *Aquatic Chemistry: Chemical Equilibria and Rates in Natural Waters*. John Wiley & Sons.

Thibodeaux, L. J. and Boyle, J. D. (1987). Bedform-generated convective transport in bottom sediment. *Nature*, 325:341–343.

Tonina, D. and Buffington, J. M. (2007). Hyporheic exchange in gravel bed rivers with pool-riffle morphology: Laboratory experiments and three-dimensional modeling. *Water Resources Research*, 43(1).

Tonina, D. and Buffington, J. M. (2009a). Hyporheic Exchange in Mountain Rivers I: Mechanics and Environmental Effects. *Geography Compass*, 3(3):1063–1086.

Tonina, D. and Buffington, J. M. (2009b). A three-dimensional model for analyzing the effects of salmon redds on hyporheic exchange and egg pocket habitat. *Canadian Journal of Fisheries and Aquatic Sciences*, 66(12):2157–2173.

Tonina, D. and Buffington, J. M. (2011). Effects of stream discharge, alluvial depth and bar amplitude on hyporheic flow in pool-riffle channels. *Water Resources Research*, 47(8).

Trauth, N., Schmidt, C., Maier, U., Vieweg, M., and Fleckenstein, J. H. (2013). Coupled 3-D stream flow and hyporheic flow model under varying stream and ambient groundwater flow conditions in a pool-riffle system. *Water Resources Research*, 49(9):5834–5850.

Trauth, N., Schmidt, C., Vieweg, M., Maier, U., and Fleckenstein, J. H. (2014). Hyporheic transport and biogeochemical reactions in pool-riffle systems under varying ambient groundwater flow conditions. *Journal of Geophysical Research: Biogeosciences*, 119(5):910–928.

Triska, F. J., Duff, J. H., and Avanzino, R. J. (1993). The role of water exchange between a stream channel and its hyporheic zone in nitrogen cycling at the terrestrial–aquatic interface. In *Nutrient Dynamics and Retention in Land/Water Ecotones of Lowland, Temperate Lakes and Rivers*, pages 167–184. Springer.

Uehlinger, U. (2006). Annual cycle and inter-annual variability of gross primary production and ecosystem respiration in a floodprone river during a 15-year period. *Freshwater Biology*, 51(5):938–950.

Van der Molen, D. T., Breeuwsma, A., and Boers, P. C. M. (1998). Agricultural Nutrient Losses to Surface Water in the Netherlands: Impact, Strategies, and Perspectives. *Journal of Environmental Quality*, 27(1):4.

Vervier, P., Dobson, M., and Pinay, G. (1993). Role of interaction zones between surface and ground waters in DOC transport and processing: Considerations for river restoration. *Freshwater Biology*, 29(2):275–284.

Vieweg, M., Trauth, N., Fleckenstein, J. H., and Schmidt, C. (2013). Robust optode-based method for measuring in situ oxygen profiles in gravelly streambeds. *Environmental Science & Technology*, 47(17):9858–9865.

Wagenschein, D. and Rode, M. (2008). Modelling the impact of river morphology on nitrogen retention – A case study of the Weisse Elster River (Germany). *Ecological Modelling*, 211(1-2):224–232.

Winter, T. C. (1998). *Ground water and surface water: A single resource*. U.S. Geological Survey, Denver, Colorado.

Woessner, W. W. (2000). Stream and fluvial plain ground water interactions: Rescaling hydrogeologic thought. *Ground Water*, 38(3):423–429.

Wondzell, S. M. and Gooseff, M. N. (2013). Geomorphic controls on hyporheic exchange across scales: Watersheds to particles. In Shroder, J. F., editor, *Treatise on Geomorphology*, pages 203–218. Academic Press, San Diego.

Wondzell, S. M., LaNier, J., and Haggerty, R. (2009). Evaluation of alternative groundwater flow models for simulating hyporheic exchange in a small mountain stream. *Journal of Hydrology*, 364(1-2):142–151.

Wondzell, S. M. and Swanson, F. J. (1996). Seasonal and Storm Dynamics of the Hyporheic Zone of a 4th-Order Mountain Stream. I: Hydrologic Processes. *Journal of the North American Benthological Society*, 15(1):3–19.

Wörman, A., Packman, A. I., Johansson, H., and Jonsson, K. (2002). Effect of flow-induced exchange in hyporheic zones on longitudinal transport of solutes in streams and rivers. *Water Resources Research*, 38(1):2–1.

Wörman, A., Packman, A. I., Marklund, L., Harvey, J. W., and Stone, S. H. (2006). Exact three-dimensional spectral solution to surface-groundwater interactions with arbitrary surface topography. *Geophysical Research Letters*, 33(7).

Wroblicky, G. J., Campana, M. E., Valett, H. M., and Dahm, C. N. (1998). Seasonal variation in surface-subsurface water exchange and lateral hyporheic area of two stream-aquifer systems. *Water Resources Research*, 34(3):317–328.

Wyrick, J. R. (2005). *On the formation of fluvial islands*. PhD thesis, Oregon State University, Corvallis, Oregon.

Yager, R. M. (1993). Estimation of hydraulic conductivity of a riverbed and aquifer system on the Susquehanna River in Broome County, New York. Technical Report WSP - 2387, U.S. Geological Survey.

Yue, W., Lin, C.-L., and Patel, V. C. (2005). Large eddy simulation of turbulent open-channel flow with free surface simulated by level set method. *Physics of Fluids*, 17(2):025108.

Zarnetske, J. P., Haggerty, R., Wondzell, S. M., and Baker, M. A. (2011a). Dynamics of nitrate production and removal as a function of residence time in the hyporheic zone. *Journal of Geophysical Research*, 116(G1).

Zarnetske, J. P., Haggerty, R., Wondzell, S. M., and Baker, M. A. (2011b). Labile dissolved organic carbon supply limits hyporheic denitrification. *Journal of Geophysical Research*, 116(G4).

Zarnetske, J. P., Haggerty, R., Wondzell, S. M., Bokil, V. A., and González-Pinzón, R. (2012). Coupled transport and reaction kinetics control the nitrate source-sink function of hyporheic zones. *Water Resources Research*, 48(11).

Danksagung

Ich danke

- *Christian Schmidt für die exzellente Betreuung mit hilfreichen Ideen und Diskussionen.*
- *Jan Fleckenstein für Betreuung, Ideen und den anschließenden PostDoc Vertrag.*
- *Uli Maier für Tipps und Tricks mit MIN3P.*
- *Michael Vieweg für eine schöne gemeinsame Doktorandenzeit mit unterhaltsamen Feldaktionen und Tagungen.*
- *Sascha Oswald für die Betreuung und Tipps zu den numerischen Modellen.*
- *den Kollegen im Department Hydrogeologie am UFZ-Leipzig für die angenehme Arbeitsatmosphäre.*
- *Marie für das Korrekturlesen des zweiten und dritten Papers.*
- *Con für das Korrekturlesen des "Rahmens".*
- *Armin, Michael und Thomas für fachliche und private Diskussionen.*
- *meinen Eltern für ihre beständige und andauernde Untersützung jeglicher Art während meines bisherigen Lebens.*
- *meinen Schwiegereltern für ihre Unterstützung und ihre Tochter.*
- *meinen Buben für die Ablenkung nach Feierabend und somit der Fokussierung auf das Wesentliche.*
- *Eva für Alles.*